Nano Today (2015) 10, 355—396

Available online at www.sciencedirect.com

ScienceDirect

journal homepage: www.elsevier.com/locate/nanotoday

REVIEW

Under the spotlight: The organic—inorganic hybrid halide perovskite for optoelectronic applications

Qi Chen[a,b], Nicholas De Marco[a,b], Yang (Michael) Yang[a], Tze-Bin Song[a,b], Chun-Chao Chen[a], Hongxiang Zhao[a,b], Ziruo Hong[a], Huanping Zhou[a,b], Yang Yang[a,b,*]

[a] *Department of Materials Science and Engineering, University of California, Los Angeles, CA 90095, USA*
[b] *California NanoSystems Institute, University of California, Los Angeles, CA 90095, USA*

Received 23 February 2015; received in revised form 17 April 2015; accepted 27 April 2015
Available online 9 June 2015

KEYWORDS
Perovskite;
Solar cells;
Hybrids;
Thin films;
Photovoltaics

Summary The dawn of a new era in optoelectronic technologies has emerged with the recent development of the organic—inorganic hybrid halide perovskite. Its exceptional attributes, including high carrier mobility, an adjustable spectral absorption range, long diffusion lengths, and the simplicity and affordability of fabrication render it one of the most exceptional and market-competitive optoelectronic materials for applications in photovoltaics, light emitting diodes (LED), photodetectors, lasers, and more. Moreover, its versatility in device architecture and ability to achieve relatively high performance devices via various processing techniques makes perovskites a highly promising material for various practical applications. Here, we review the organic—inorganic hybrid halide perovskite and delve into its recent progress and relevant applications.

Introduction

The rise of the organic—inorganic hybrid halide perovskite (hybrid perovskite) has stunned the photovoltaic community with its remarkable performance and rapid progress in the past 5 years [1—4]. This extraordinary material has exhibited unprecedented development, soaring to reach 20% power conversion efficiency (PCE) in photovoltaic (PV) devices [5—9].

Perovskites derive their name from the mineral structure of calcium titanium oxide ($CaTiO_3$), discovered by German mineralogist Gustav Rose in the year 1839. This structure was later characterized by Russian mineralogist Lev A. Perovski, from which it derives its name. The family of perovskite

* Corresponding author at: Department of Materials Science and Engineering, University of California, Los Angeles, CA 90095, USA. Tel.: +1 3108254052.
E-mail address: yangy@ucla.edu (Y. Yang).

http://dx.doi.org/10.1016/j.nantod.2015.04.009

materials adopt the chemical formula ABX_3, where A and B are cations of dissimilar sizes, and X are anions, typically oxygen, halogens, or alkali metals. Historically, oxide-based perovskites (X=O) have been the most actively studied of the perovskite family as a result of their superior ferroelectric, magnetic, and superconductive properties [10]. The first halide-based perovskite structure was observed in cesium lead halides ($CsPbX_3$) by Moller in 1958 [11]. It was observed that photoconductive properties could be tuned through varying halide components to achieve different spectral responses. The first appearance of the organic cation, methylammonium (MA), in halide perovskites was seen by Weber and Naturforsch in 1978 for I, Cl, and Br [12]. In the 1990s, Mitzi and co-workers focused on layered organic—inorganic halide perovskites that featured strong excitonic characteristics and demonstrated applications in thin film transistors (TFT) and light-emitting diodes (LED) [13].

The hybrid perovskite made its debut in photovoltaics in 2006 when Miyasaka and colleagues employed $CH_3NH_3PbBr_3$ as a sensitizer on nanoporous TiO_2 in a liquid electrolyte-based dye-sensitized solar cell (DSSC), realizing an efficiency of 2.2% [14]. In 2009, a power conversion efficiency (PCE) of 3.8% was achieved by replacing Br with I [15]. In 2011, Park and co-workers achieved an efficiency of 6.5% by employing perovskite nanoparticles (~2.5 nm in diameter) on TiO_2 to serve as sensitizers for improved absorption over conventional dyes [16]. However, these devices were highly susceptible to dissolution within the polar electrolyte solution. Consequentially, in 2012 a solid electrolyte 2,2′,7,7′-tetrakis(N,N-di-p-methoxyphenylamine)-9,9′-spirobifluorene (Spiro-MeOTAD) was employed as a hole transport material (HTM), achieving an initial efficiency of 9.7% and improved stability compared to the liquid-based design [17]. In the same year, a HTM-free device was demonstrated with a PCE of 7.3% [18]. Later, Snaith et al. reported replacement of the n-type TiO_2 electron transport material (ETM) with an inert Al_2O_3 scaffold, demonstrating an efficiency of 10.9% [19]. These reports revealed the ambipolar nature of perovskites, which enlightened and encouraged the intensive employment of the planar heterojunction architecture in these devices [7,20,21]. Meanwhile, Snaith and co-workers reported a mixed-halide perovskite by using chlorine-containing precursors, demonstrating improved carrier transport, diffusion lengths and stability over its triiodide counterpart [17]. Later, bromine inclusion was reported to feature an adjustable band gap for perovskites [22]. This sparked an enormous development in the hybrid lead halide perovskite $CH_3NH_3PbX_3$ (X = I, Cl, Br), obtaining a record PCE reaching up to 20.1% in just five years using low cost production methods. This family of materials exhibits a myriad of properties ideal for PV such as high dual electron and hole mobility, large absorption coefficients resulting from s—p antibonding coupling, a favorable band gap, a strong defect tolerance and shallow point defects, benign grain boundary recombination effects and reduced surface recombination. Consequently, hybrid perovskites have been implemented into various photonic devices and found great promise for applications beyond photovolatics. The versatility of hybrid perovskites also presents a facile and affordable route, as 15% efficiencies can be obtained with relative ease through diverse architectures and processing techniques. In this article, we present a thorough review of the recent developments in fundamental material properties ('Material properties' section), notable achievements of perovskites for photovoltaics ('PV applications' section), and other promising applications ('Applications beyond PV' section).

Material properties

In general, optoelectronic materials can be categorized as either organic or inorganic according to their chemical compositions that lead to strikingly different property trends in materials. The family of hybrid organic—inorganic perovskite materials introduces a molecular assembly of a well-defined nanoscale structure serving as an exemplary species to closely bridge these organic and inorganic worlds. In this section, we will review the recent efforts in understanding the unique structure—property relationships seen in hybrid perovskite materials.

Perovskites are a large family of compounds that share the same chemical formula ABX_3. 'A' and 'B' denote cations, where A is much larger than B, and 'X' an anion. The versatility of perovskites makes them highly attractive as they can form multidimensional structures pertaining to the same chemical formula through use of different combinations of various components. A wide variety of elements may be incorporated each with different valency, so long as charge neutrality is satisfied, making perovskites one of the most highly studied materials. As we shall see in the following sections, there is a stringent structure—property relationship for perovskites pertaining to both crystal composition and ion arrangement that govern its structural, optical and electronic properties. Here we will discuss the formability of perovskites and its corresponding impacts on relevant properties.

Historically, oxide perovskites (X=O) have been most actively studied as they possess a unique multifunctional nature. Studies of the perovskite crystal chemistry date back to 1920, conducted by Goldschmidt [23], that revealed the significance of relative radii sizes to polyhedral packing that ultimately led to the ever-important tolerance factor (further discussed in the coming sections). Eventually, it was revealed that with proper tuning of composition a wide variety of electronic properties including capacitive, ferroelectric, piezoelectric, superconductive, metallic, catalytic, and magnetic could be achieved [24]. While ferroelectric properties have recently shown beneficial effects in photovoltaics, the wide band gaps of oxide perovskites limit their use in solar applications as they utilize a mere 8—20% of the solar spectrum.

Halide perovskites, as the name implies, employ an inorganic halide (I^-, Cl^-, Br^-) to replace the oxygen anion of oxide perovskites. An organic or inorganic monovalent A^+ cation and a divalent B^{2+} metal cation are generally seen corresponding to the 1^- charge of the halide anion.

The hybrid organic—inorganic halide perovskite (hybrid perovskite), most commonly denoted as $CH_3NH_3PbI_3$ ($MAPbI_3$), often has the A site occupied by an organic component. Similarly to its parent oxide perovskite, halide perovskites must obey allowable tolerance factors to achieve desired crystal symmetry. The structural

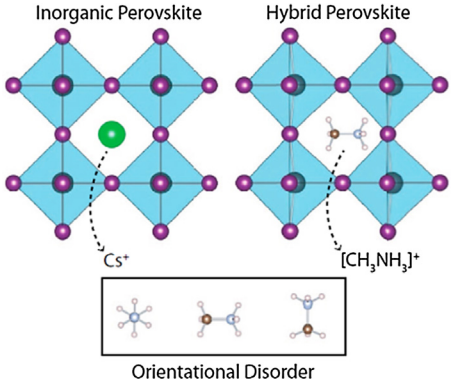

Figure 2.1 Orientational disorder associated with the non-spherically symmetric organic methylammonium ($CH_3NH_3^+$) cation versus the spherically symmetric inorganic cesium (Cs^+) cation.
Source: Adapted with permission from Ref. [27].

dimensionality of halide perovskites can be easily tuned through varying components to obtain zero-dimensional (0D) ($(CH_3NH_3)_4PbX_62H_2O$), one-dimensional (1D) ($C_5H_{10}NH_2PbX_3$), two dimensional (2D) ($C_nH_{2n+1}NH_3PbX_4$), and three dimensional ($CH_3NH_3PbX_3$) structures simply by changing organic—inorganic precursor molar ratios [25]. Here a clear distinction between organic and inorganic perovskites must be noted. Aside from a clear difference in A species, inorganic (e.g. Cs^+) versus organic (e.g. $CH_3NH_3^+$), there is also a change in symmetry of the A site component from spherical (inorganic) to non-spherical (organic) (Fig. 2.1). This is particularly important in terms of orientational disorder and polarization, discussed further in the coming sections [26]. In this section we will focus our discussion on the properties of this family of materials pertaining to the influences of varying each component and the associated structure—property relations.

Crystal structure and composition

Symmetry and phase

The electronic properties of perovskite compounds are governed by the B—X bond of the inorganic framework. While the A cation does not directly contribute toward electronic properties [25,28,29], its size can cause distortion of the B—X bonds thus adversely affecting symmetry. Cubic symmetry is the ideal case for perovskites, corresponding to a P*m*3*m* space group with 12-fold coordination of the A cation, 6-fold coordination of B cations, and corner residing BX_6 octahedra (Fig. 2.2a and b).

Deviations from cubic symmetry can result from several factors, the first being size effects. A tolerance factor, developed by Goldschmidt [23], presents a guideline for tuning of radii sizes relative to cubic symmetry, described by $t = (R_A + R_X)/[\sqrt{2}|(R_B + R_X)]$ where R_A, R_B, R_X are the ionic radii of A, B, X, respectively. In general, cubic structures occur for $0.89 < t < 1$ for oxide perovskites [30] and $0.85 < t < 1.11$ for halide perovskites [31]. Cubic symmetry provides optimum electronic properties due to a high degree of ionic bonding. Mismatch of crystal components outside of the ideal tolerance range result in octahedral tilting that

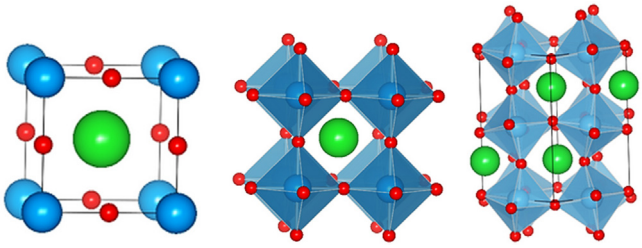

Figure 2.2 The ideal cubic perovskite unit cell. (a) A cations (blue) occupy the lattice corners, B cations (green) occupy the interstitial site, and X anions (red) occupy lattice faces. (b) An alternative view depicting B cations assembled around X anions to form BX_6 octahedra, as B—X bonds are responsible for determining electrical properties. (c) Tilting of BX_6 octahedra occurring from non-ideal size effects and other factors, inducing strain on the B—X bonds.

can affect electronic properties (Fig. 2.2c). For instance, if $t < 1$ the B—X bonds will undergo compression and the A—X bonds tension to compensate for the excess space (void). A rotation of octahedra will result to accommodate these induced stresses that lead to reduced symmetry and tilting of BX_6 octahedra. If $t > 1$, as a result of a large A or small B, a higher degree of symmetry will result, providing a more stable hexagonal structure. Moreover, perovskites can obtain different dimensionalities based on component sizes. Occupation of A sites by monovalent cations, such as Rb^+, Cs^+, $CH_3NH_3^+$, and $HC(NH_2)_2^+$, form a three-dimensional (3D) framework, whereas if a larger cation, such as $CH_3CH_2NH_3^+$, is used, two-dimensional (2D) or one-dimensional (1D) structures can be obtained. Thus we can see that the case of an excessively large A cation results in destruction of the 3D framework, corresponding to $t \ll 1$ and a reduced dimensionality.

To further compliment Goldschmidt's tolerance factor in constructing a structure map for perovskites, an octahedral factor (μ) was developed by Li and company [31]. It provides a ratio of the ionic radii of the B cation to the X anion, given by $\mu = R_B/R_X$, that is directly correlated to the BX_6 octahedron. According to this factor, halide perovskite formation occurs for $\mu > 0.442$, whereas below this value BX_6 octahedron will become unstable and a perovskite structure will not form. Though these two combined factors provide a reasonable guideline for determining halide perovskite formability, they are not entirely sufficient for predicting all structure formations within the perovskite family [31]. A comparison for tolerance and octahedral factors for commonly employed halide perovskites are provided in Fig. 2.3.

Furthermore, external effects, such as heat or oxidative/reductive environments, can cause compositional changes that also contribute toward distortion. For instance, the valency of the transition metal or the relative amount of oxygen present can be altered to create voids within the crystal structure of oxide perovskites that change size effects. In some cases, Jahn—Teller distortion [30], a distortion of spatial degeneracy, can arise for some B cations in perovskites, such as Mn^{3+}, that can distort the non-linear BX_6 octahedra due to the odd number of electrons residing in the E_g energy level [30]. An associated pressure-dependence of perovskites has also been observed [25], producing a

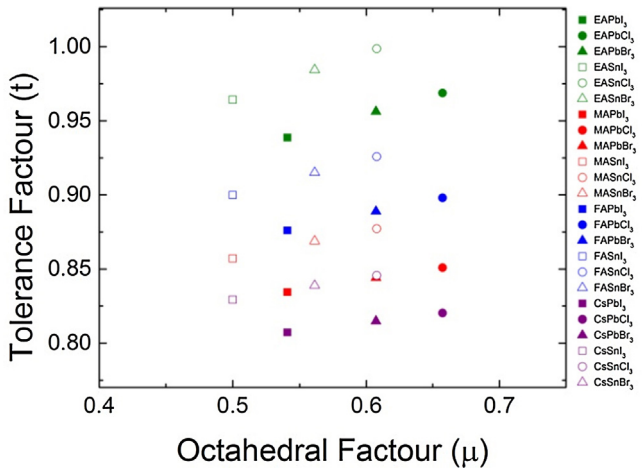

Figure 2.3 Calculated octahedral and tolerance factors for various combinations of commonly employed organic and inorganic hybrid perovskite components.
Source: Ionic Radii adopted from Ref. in Table 2.2.

redshift as further pressure is applied to the B—X bond. This can be further understood by examining the electronic band structure, as will be discussed in the coming sections. Thus it is apparent that crystal component selections, along with external effects, are important considerations in obtaining a desired symmetry for specifically tailored properties.

Analysis of perovskite crystals has revealed cubic (P*m*3*m*), tetragonal (I4/*mcm*), and orthorhombic (P*nam*) phases via X-ray Diffraction (XRD) [27]. In general, perovskites adopt cubic structures and undergo phase transitions from cubic to tetragonal to orthorhombic upon temperature reduction [12]. The symmetry of perovskites increases with temperature, where at room temperature $MAPbI_3$ forms a tetragonal structure, and $MAPbCl_3$ and $MAPbBr_3$ form cubic structures [32]. $MAPbI_{3-x}Cl_x$ has been observed to adopt a tetragonal crystal structure at room temperature similar to that of $MAPbI_3$ [33—35]. Furthermore, transmission electron microscopy (TEM) has revealed a 'pseudocubic' structure resulting from octahedral tilting and cation rotation [27,35]. It has been shown that $MAPbI_3$ undergoes a phase transformation to a lower symmetry from tetragonal to pseudocubic at temperatures in the range of 300 K and 400 K [36]. A detailed study has been conducted by Kanatzidis et al. on MA, FA, Pb, and Sn perovskite combinations to identify three distinct phase transitions that occur classified as such: a high temperature α phase, an intermediate β temperature phase, and a low temperature γ phase, and are summarized in Table 2.1 [36]. These results are in agreement with previous studies by Poglitsch and Weber [34]. It can be noted that FA-based perovskites show no high temperature phase transformation that may be of significance for field use of perovskite solar cells. Phase transitions, occurring via external temperature or pressure effects, are undoubtedly important considerations during processing and solar cell operation.

'A' site

The A cation has shown no direct contribution toward electronic properties [37]. Fig. 2.4 portrays a contour plot of electron density for $CH_3NH_3PbBr_3$, highlighting the weak interaction and negligible overlap of electron orbitals between the organic component and inorganic B—X octahedra [25]. However, simulations have shown that the size of the A cation can alter the degree of distortion with varying size that in turn affects electronic properties [25,38—41]. When the A lattice site is occupied by a small monovalent cation, such as cesium (Cs), rubidium (Rb), methylammonium (MA), formamidinium (FA), 3D symmetry is achieved [36]. By increasing R_A the tolerance factor approaches unity ($t \rightarrow 1$), resulting in a higher packing symmetry that corresponds to a reduction in band gap, so long as the size is not sufficiently large ($t > 1$) [39].

Methylammonium (MA). The most widely used A cation for hybrid perovskites, the methylammonium ion (MA; $CH_3NH_3^+$; $R_{MA} = 0.18$ nm) [43], has achieved efficiencies of 15% and above for $MAPbI_3$ devices. At room temperature a tetragonal symmetry is formed for $MAPbI_3$, rather than cubic, due to the small size of the MA ion. This yields a bandgap of 1.51—1.55 eV that pertains to an absorption edge at 820 nm, exceeding the optimal 1.1—1.4 eV band gap range dictated by the Shockley—Queisser limit for a single junction solar cell [38,39,44]. Thus, one may speculate that substitution of MA with a larger cation should yield higher symmetry and correspondingly a smaller band gap to allow for enhanced light harvesting across the spectrum. In a quest to replace the unfavorably sized MA ion, other cations have been explored that include ethylammonium (EA), formamidinium (FA) and cesium (Cs), where $R_{Cs} < R_{MA} < R_{FA} < R_{EA}$ (Table 2.2). However, replacement of MA with an excessively large cation, such as EA ($CH_3CH_2NH_3^+$) disrupts the 3D symmetry yielding a 2D orthorhombic crystal structure with a relatively large band gap of 2.2 eV for $EAPbI_3$. The $EAPbI_3$ sensitized solar cell has been reported to achieve a PCE of 2.4% under a 1 sun condition [40]. Thus, it is apparent that an organic cation whose ionic radius is between that of MA and EA is desirable.

Formamidinium (FA). In this regard, FA ($HC(NH_2)_2^+$) is expected to yield a higher symmetry than that of MA and thus has been most extensively investigated. Indeed, $FAPbI_3$ crystals yield and a favorable band gap (~1.43—1.48 eV, 840 nm absorption onset) closer to the optimal 1.4 eV band gap [38,39,46,47]. FA adopts a nearly cubic structure, however due to the disordered nature of the FA—I ion interaction, the asymmetrical FA ion sits off-center within the octahedron, resulting in a trigonal structure [38]. However, a yellow 1D hexagonal non-perovskite polymorph of $FAPbI_3$ has been commonly observed and is thought to hamper PV performance due to an unfavorable band alignment with TiO_2 causing poor electron injection [36,46,47]. It is believed that if this phase can be entirely eliminated performances of FA-based devices would surpass those of MA.

Cesium (Cs). Studies of cesium perovskites date back to the early 1970s when they were investigated by Scaife and company [48]. It was observed that $CsSnI_3$ displayed strong PL intensity at room temperature in the near-IR region of the spectrum [49]. Chung and co-workers investigated structural characterizations of $CsSnI_3$ perovskites revealing four different structural phases that exist independently at room temperature [50,51]. Furthermore, a p-type behavior has been observed for which is attributed to Sn vacancies that create highly mobile holes [51]. The smaller size of Cs in comparison to MA induces octahedral tilting and accordingly

Table 2.1 Structural phase transformations for commonly employed hybrid perovskites.

PVSK	Phase	Temperature (K)	Structure	Space group	Lattice parameters (Å)			Volume (Å^3)
$MAPbI_3$	α	400	Tetragonal	P4*mm*	*a* = 6.3115	*b* = 6.3115	*c* = 6.3161	251.6
	β	293	Tetragonal	I4*cm*	*a* = 8.849	*b* = 8.849	*c* = 12.642	990
	γ	162–172	Orthorhombic	P*na*2$_1$	*a* = 5.673	*b* = 5.628	*c* = 11.182	959.6
$MAPbCl_3$	α	>178.8	Cubic	P*m*3*m*	*a* = 5.675			182.2
	β	172.9–178.9	Tetragonal	P4/*mmm*	*a* = 5.655	*c* = 5.630		180.1
	γ	<172.9	Orthorhombic	P222$_1$	*a* = 5.673	*b* = 5.628	*c* = 11.182	375
$MAPbBr_3$	α	>236.9	Cubic	P*m*3*m*	*a* = 5.901			206.3
	β	155.1–236.9	Tetragonal	I4/*mcm*	*a* = 8.322	*c* = 11.833		819.4
	γ	149.5–155.1	Tetragonal	P4/*mmm*	*a* = 5.8942	*c* = 5.8612		
	δ	<144.5	Orthorhombic	P*na*2$_1$	*a* = 7.979	*b* = 8.580	*c* = 11.849	811.1
$MASnI_3$	α	293	Tetragonal	P4*mm*	*a* = 6.2302	*b* = 6.2302	*c* = 6.2316	241.88
	β	200	Tetragonal	I4*cm*	*a* = 8.7577	*b* = 8.7577	*c* = 12.429	953.2
$FAPbI_3$	α	293	Trigonal	P3*m*1	*a* = 8.9817	*b* = 8.9817	*c* = 11.006	768.9
	β	150	Trigonal	P3	*a* = 17.791	*b* = 17.791	*c* = 10.091	2988.4
$FASnI_3$	α	340	Orthorhombic	A*mm*2	*a* = 6.3286	*b* = 8.9554	*c* = 8.9463	507.03
	β	180	Orthorhombic	I*mm*2	*a* = 12.512	*b* = 12.512	*c* = 12.509	1959.2

Source: Adapted with permission from Refs. [34,36].

Table 2.2 Ionic radii of commonly employed hybrid perovskite components.

Ion	A cation				B cation		X anion			
	EA	FA	MA	Cs	Pb	Sn	I	Br	Cl	F
Ionic radius (Å)	2.3	1.9–2.2	1.8	1.67	1.19	1.1	2.2	1.96	1.81	1.33

Source: Adapted with permission from Refs. [15,35,43,45].

a lower symmetry (*t* is reduced). This leads to a higher band gap (1.73 eV) for $CsPbI_3$ over $MAPbI_3$ (1.57 eV), further moving away from the desired band gap value of 1.4 eV [39].

Mixed A cations. Mixed cations allow for combination of the strong individual attributes of various individual components. The first mixed A cation was reported by Pellet and co-workers [47] who were able to tune the band gap of $(MA)_x(FA)_{1-x}PbI_3$ devices by varying the ratio of MA to FA(*x*), ultimately achieving a PCE of 14.9%. The improved performance compared to pure MA was due to greater absorption of the red region of spectrum, resulting in higher photocurrent without large loss of open circuit voltage. Several reports have been documented for $(MA)_x(FA)_{1-x}PbI_3$ based devices with respectful PCEs [38,39,52]. On the other hand, Cs doping of the perovskite absorber has been employed in $Cs_x(MA)_{1-x}PbI_3$ devices achieving a PCE of 7.68% [53].

One unique mixed A cation hybrid perovskite device based on 5-aminovaleric acid (5-AVA), $(5\text{-AVA})_x(MA)_{1-x}PbI_3$, was employed by Mei and company [54] to realize perovskite films with a reduced quantity of defects and a higher degree of conformity with the adjacent titania layer. This resulted in increased exciton lifetime and dissociation yield compared to that of pure $MAPbI_3$. Partial substitution of the MA cations with 5-AVA in the cuboctahedral site yielded an orthorhombic perovskite phase, where significant expansion of lattice parameters *b* and *c* occurred. This was thought to provide a preferential growth template along its axis due to the interaction with the lead and iodide ions resulting in improved surface contact between layers. $(5\text{-AVA})_x(MA)_{1-x}PbI_3$ devices achieved a efficiencies reaching 12.8%, and more notably improved stability in air and under illumination compared to that of MA.

'B' site

The B metal cation sites in hybrid perovskites are occupied by the group IVA metals in a divalent oxidation state (Pb^{2+}, Sn^{2+}, Ge^{2+}). Lead (Pb) has proven the superior constituent compared to tin (Sn), both in terms of performance and stability, and consequentially has been the most widely employed of the group IVA metals [28,55,56]. Germanium (Ge) has been rarely studied in comparison to Pb and Sn, likely due to its highly unstable nature in the 2+ oxidation state [57,58]. Upon proceeding up group IVA on the periodic table (Pb → Ge), a reduction in stability of the divalent oxidation state occurs for each element as a consequence of reduced inert electron pair effects [58]. However, this also corresponds to an increase in electronegativity, or covalent character, that in turn yields a reduction in band gap. Thus, one may speculate the ideal case to be a lower atomic number group IVA element, however, this also goes hand-in-hand with a compromise in divalent metal stability. For instance, $MASnX_3$ in theory possesses a more optimal band gap (1.2–1.4 eV) than $MAPbX_3$ (1.6–1.8 eV), but suffers from rapid degradation as a result of the inherent instability of the Sn^{2+} state as it readily oxidizes to Sn^{4+} upon contact with air producing a volatile SnI_4 compound [36,55,56]. As this

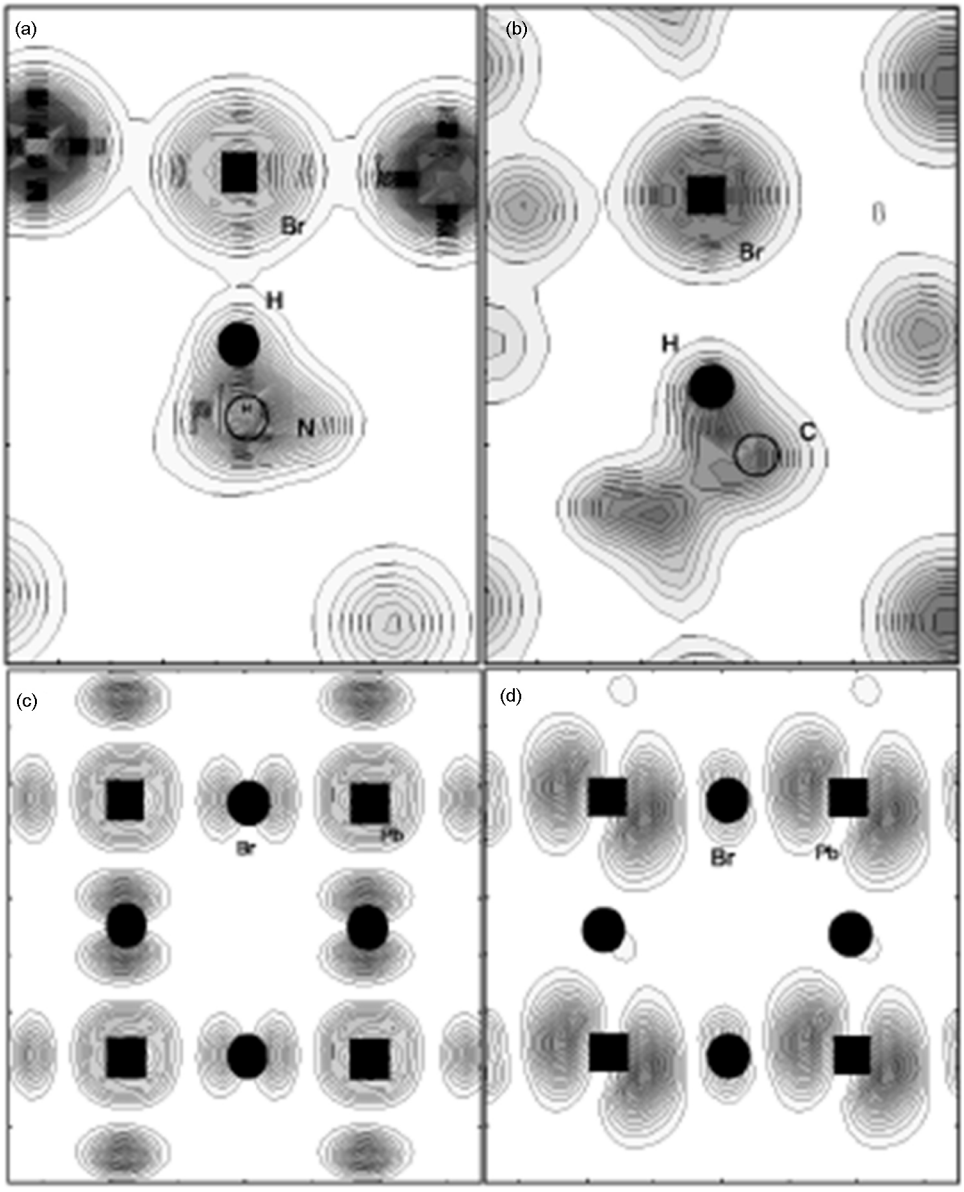

Figure 2.4 Contour plot depicting electron orbital overlap and total electron density of $CH_3NH_3PbBr_3$ for (a) the N—H—Br plane and (b) the C—H—Br plane. Electron density representing the (c) valence band maximum (VBM) and (d) conduction band minimum (CBM) states.
Source: Adapted with permission from Ref. [42].

effect is even more prominent for the case of Ge^{2+}, it is presumptively why no successful Ge-based hybrid perovskites have been developed.

Hao and collaborators reported lead free hybrid perovskites through $MASnI_3$ and $MASnI_{3-x}Br_x$ devices achieving a maximum PCE of 5.73% [55]. Noel et al. later improved this lead-free Sn-based efficiency to over 6% under 1 sun illumination [61]. Stoumpos and company have studied the structure and symmetry of Pb- and Sn-based perovskites [36]. While both $MASnI_3$ and $MAPbI_3$ adopt a tetragonal structure (P4*mm*) at ambient conditions, $MASnI_3$ adopts a higher symmetry α-phase unlike the β-phase seen for $MAPbI_3$ [36,55]. $MASnX_3$ perovskites have the potential to produce a much larger photocurrent density (J_{sc}) than those for $MAPbX_3$, however stability issues present a large obstacle that must first be overcome [28].

Mixed B cations. Mixed $MASn_{1-x}Pb_xI_3$ devices have been studied by Stoumpos et al. and Ogomi et al. [36,59], demonstrating band gap tuning through varying Pb:Sn ratios. For Sn-rich compositions up to $x = 0.5$, a pseudocubic tetragonal P4*mm* structure is obtained, similarly to the pure $MASnI_3$ structure [36]. For a further increase in Sn composition, the structure changes to a tetragonal I4*cm* structure. As expected, an increase in Sn content yields an extension of absorption and a reduction in band gap [36,59]. Furthermore, continuous progress in improving PCE has been achieved in binary metal perovskite based solar cells, detailed elsewhere [55,60,61].

'X' site

The halide anion has been the most effectively varied component in hybrid perovskites. Upon proceeding down group VIIA (Cl → I) atomic size increases, absorption spectra shifts to longer wavelengths, and a reduction in energy (redshift) occurs [59]. This can be attributed to the decrease in electronegativity to better match that of Pb, effectively reducing ionic and increasing covalent character.

Iodide (I). Iodide (I^-) is the basis for hybrid perovskites, achieving the most consistent efficiencies near 15% for hybrid perovskite devices [6,7,28,62]. Iodide lies closest to Pb on the periodic table and thus shares a similar covalent character, resulting in the most stable structure. While iodide has provided the foundation for hybrid perovskite halide components, its ease of oxidation has introduced quite a lot of concerns regarding the stability. Thus, iodide substitutes and mixed halide perovskites are of great interest.

Chloride (Cl). It was not until the addition of chlorine (Cl) that efficiencies were further pushed, especially in planar configurations, as Cl has shown to provide improved diffusion lengths and carrier lifetimes [33,63–67] despite a nearly identical band gap to that of pure iodide-based devices. Cl incorporation yields an apparent low miscibility with iodide in comparison to Br as a result of the larger difference in ionic radii and higher degree of covalent character [66,68,69]. $MAPbCl_3$ adopts a cubic structure at room temperature, however, mixed $MAPbI_{3-x}Cl_x$ have shown to produce highly oriented crystalline structures, exemplified through the strong (1 1 0), (2 2 0), and (3 3 0) peaks attributed to the tetragonal phase [32,68]. In early works, it was thought that chloride inclusion occurred along the (0 0 1) (apical positions) direction as only scattering from the (1 1 0) direction of the highly oriented $MAPbI_{3-x}Cl_x$ was detected via X-ray diffraction (XRD) [33,68]. Furthermore, powder XRD analysis has shown the stoichiometry of $MAPbI_{3-x}Cl_x$ to be very similar to that of $MAPbI_3$, with a maximum 3–4% Cl to I ratio [65,68]. On the other hand, X-ray photoelectron spectroscopy (XPS) revealed minimal chloride content of 1–2% in perovskite films [68,70,71]. It has been proposed that sublimation of Cl content occurs, leaving remains of pure $MAPbI_3$ [66,68]. Other works have claimed the presence of chloride within the physical perovskite structure as $MAPbI_{3-x}Cl_x$ to be incorrect, and believe it remains as unconverted $PbCl_2$ that serves as nucleation sites to improve surface coverage of the perovskite film [42,69].

Currently, chlorine incorporation has been investigated in the context of perovskite film growth in order to reveal

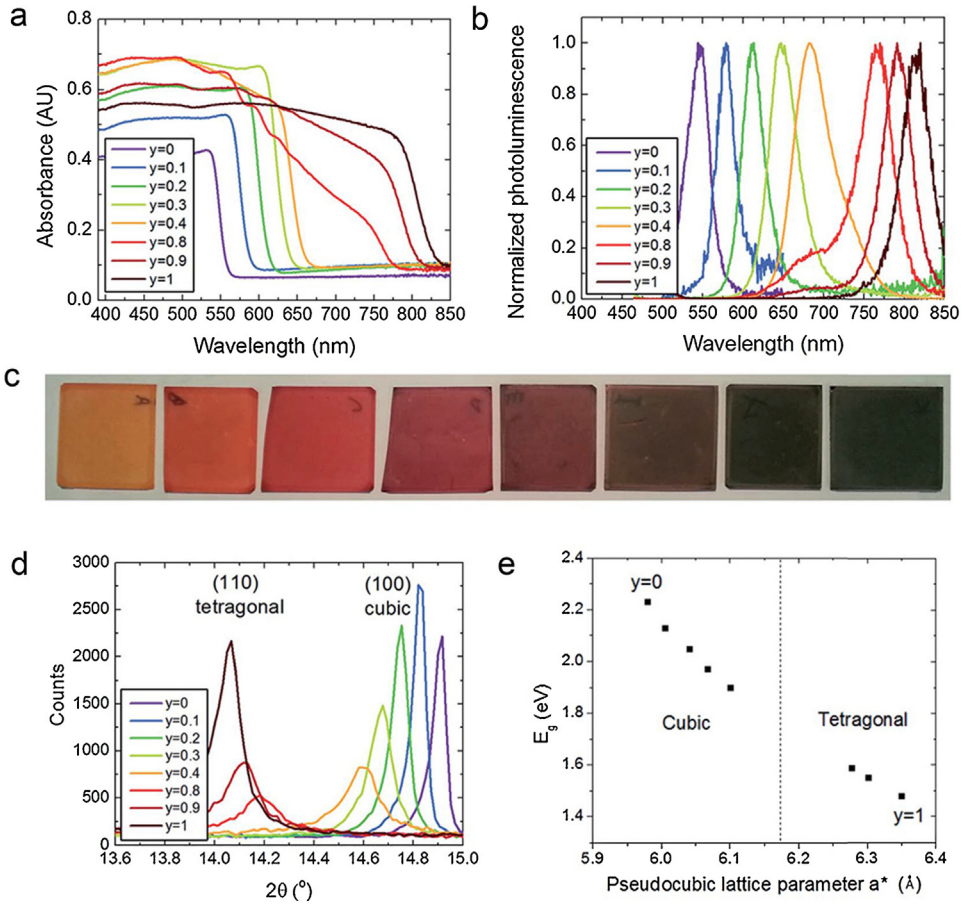

Figure 2.5 $FAPbI_xBr_{3-x}$ devices for varying I:Br ratios (*x*) depicting: (a) absorbance spectra, (b) photoluminescence spectra, (c) color change, (d) XRD spectra of phase transition from a Br-rich cubic phase to a I-rich tetragonal phase, and (e) band gap variation. *Source*: Adapted with permission from Ref. [39].

the mechanisms that govern improved device performances [68—70,72—74]. It has been suggested that crystallization begins from the nucleation of complex ion aggregates due to the limited solubility of the chlorine containing precursors, e.g. $PbCl_2$ in dimethylformamide (DMF). Rearrangement of constituent ions occurs during the subsequent crystal growth, for which chlorine facilitates the release of excess organic components that ultimately determines the crystallographic textures and grain structures of the perovskite film. The accumulative efforts provide direct evidence that chloride inclusion governs the morphological evolution in the absorber and consequently affects material properties and device performance.

Bromide (Br). Bromide has been most effectively used to tune the band gap of hybrid perovskites [39]. It is believed that upon Br inclusion in iodide-based hybrid perovskites, the size effect on lattice parameters will induce a compressive stress on Pb—I bonds, causing structural distortion that leads to the observed band gap increase [33]. $MAPbBr_3$ adopts a cubic structure at room temperature, forming large sized crystals [32]. $MAPbI_xBr_{3-x}$ has reported to enhance power conversion efficiency and stability through the chemical management to tune the band gap [22]. Snaith and co-workers investigated the effects of mixed halide $FAPbI_xBr_{3-x}$ compositions [39], realizing a tunable band gap between 1.48 and 2.23 eV and a wide variety of film color (Fig. 2.5). Increasing the iodide content redshifts the band gap and induces a phase transition from a cubic Br rich phase ($y < 0.5$) to an I-rich tetragonal phase ($y > 0.7$). Their champion device achieved a PCE of 14.2% and J_{sc} in excess of 23 mA/cm^2. It was found that increasing iodide content resulted in increased V_{oc} and decreased J_{sc}.

Mosconi and co-workers conducted computational studies on mixed halide $MAPbI_{3-x}X_x$ perovskites providing insight into variations in structure for Cl and Br inclusions [33]. It was shown that Br preferentially locates at apical and equatorial positions as opposed to Cl, which is located only at the apical position. $MAPbI_{3-x}Br_x$ has an absorption onset around blue shifted compared to that of $MAPbI_3$ and $MAPbI_{3-x}Cl_x$. Variations in structure—property relationships were observed by varying the halide component, for which formations energies decreased from $I \rightarrow Cl$.

Fluoride (F). Fluorine (F^-), while a highly desirable inclusion for optoelectronic applications due to its strong electron-withdrawing nature and ability to form strong hydrogen bonding (N—H—F) over other halides [62,75] yields an undesirable tolerance factor and a high degree of lattice strain that inhibits light harvesting capabilities and conductivity. This is a direct result of its very small radius in comparison to iodide.

Complex ions. Nagane and group members demonstrated a strategy to achieve a mixed halide incorporating F^- using BF_4^-, showing an order of magnitude higher low frequency conductivity than I^- [75]. BF_4^- is similar in size to I^- (0.218 nm, 0.220 nm), thus an identical tetragonal crystal structure for $MAPbI_{3-x}(BF_4)_x$ was observed along with a similar band gap of 1.5 eV corresponding to an absorption onset of 760 nm (compared to MA at 780 nm) due to the electron withdrawing characteristics of the fluorine atom. Furthermore, a strong hydrogen bonding between the BF_4^- halide and MA cation occurs due to the strong electronegativity of the fluorine component that may aid in preventing volatization of the MA ions.

Optoelectronic properties

The phenomenal performances of hybrid perovskites stem from the substantial characteristic properties they possess. Hybrid perovskites demonstrate a strong optical absorption, an adjustable band gap, long diffusion lengths, ambipolar charge transport, high carrier mobility, and a high tolerance of defects [6,7,15,18,26,56,64,76—79]. As discussed in the previous sections, the ability to tune electronic and optical properties of hybrid perovskites with such ease presents a major attraction. Nevertheless, there remain several factors that are not entirely understood, and large barriers still to overcome in terms of stability and toxicity for large-scale implementation.

Absorption

Hybrid perovskites exhibit strong optical absorbance, allowing for a much reduced thickness necessary to efficiently facilitate collection of charge carriers [15,18,76]. Absorption across the entire visible spectrum is achievable with a mere 500 nm thick perovskite film, far less than the 2 μm

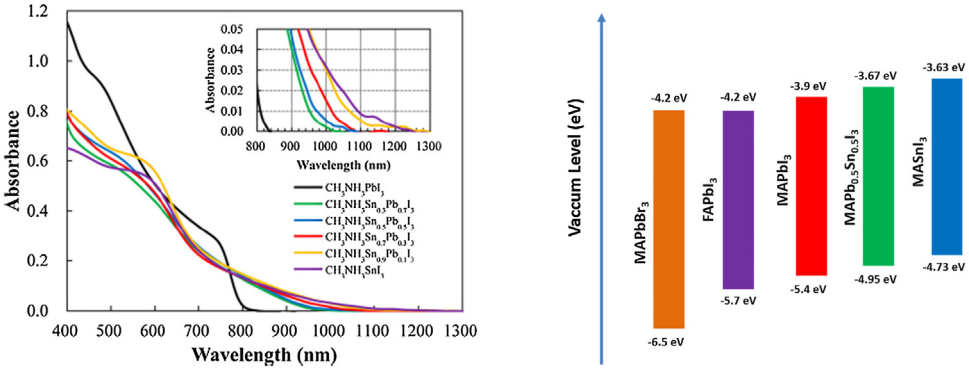

Figure 2.6 Absorption spectra for $MAPb_{1-x}Sn_xI_3$ perovskites (left) and energy band diagram of common hybrid perovskite materials (right). Refs. [39,59].

limitations typically required by solar cell active layers. The absorption peak for both $MAPbI_3$ and $MASnI_3$ are sharp, indicating a direct band gap [6,7,15,18,27,56]. $MAPbI_3$-based devices typically achieve absorption up to the tail end of the red region of the spectrum, approximately 800 nm. It has been demonstrated that Sn-based halide perovskites can extend optical absorbance up to 1000 nm into the near infrared region (NIR) [59]. Moreover, mixed $MASn_xPb_{1-x}I_3$ devices have further extended the absorption edge from 1000 to 1300 nm for a 0.3—1.0 increase in x, corresponding to a valence band shift from −5.12 eV to −4.73 eV and a conduction band shift from −3.18 to −3.63 eV (Fig. 2.6a) [59]. As we can observe, the VB shift is larger than that of the CB shift, effectively reducing the band gap. Absorption spectra for $MAPbI_3$ and $MAPbI_{3-x}Cl_x$ are nearly identical, with onsets located at approximately 800 nm, whereas $MAPbI_{3-x}Br_x$ yields absorption onsets at increased energies close to 700 nm [15,19,33,80]. $FAPbI_3$-based devices have shown reduced band gaps (1.48 eV) with absorption onsets near 850 nm. Incorporation of Br in $FAPbI_{3-x}Br_x$, can be used to tune the band gap, increasing to 2.23 eV for $x = 0$ (100% Br content) corresponding to an absorption onset of approximately 550 nm (Fig. 2.5a). It has been shown that $MAPbI_3$ has a sharp absorption onset, with an Urbach energy of 15 meV [81]. The optical absorption increases exponentially for more than four orders of magnitude (decades) in the below band gap region, with no presence of optically detected deep states. The absence of detectable sub-bandgap absorption below photon energies of 1.5 eV for perovskites makes it a promising candidate for tandem devices, as will be discussed in the coming sections. Energy band alignments of commonly employed hybrid perovskite materials are presented in Fig. 2.6.

Carrier diffusion length

Carrier diffusion lengths (L_D) up to 100 nm for both electrons and holes in $MAPbI_3$ and exceeding 1 μm in the mixed halide $MAPbI_{3-x}Cl_x$ have been reported via transient photoluminescence (PL) measurements [64,82]. However, it has been demonstrated that holes are much more efficiently extracted than electrons in $MAPbI_3$ [83], thus explaining the necessity of a mesoporous ETM for $MAPbI_3$-based devices, whereas in $MAPbI_{3-x}Cl_x$, both electrons and holes have diffusion lengths exceeding 1 μm and do not require a mesoporous ETM. Even more recently, Dong et al. have demonstrated diffusion lengths over 175 μm in single crystals of $MAPbI_3$ under 1 sun illumination, owed to enhanced carrier mobility, lifetime and reduced number of defects in the monocrystalline film [79]. Moreover, FA-based devices have shown diffusion lengths intermediate to those of $MAPbI_3$ and $MAPbI_{3-x}Cl_x$.

Carrier mobility

A near instant charge generation has been observed in $MAPbI_3$, dissociating into essentially balanced free charge carriers within 2 picoseconds (ps) of high mobility (25 cm^2/Vs) that remain so for up to tens of microseconds [78]. Furthermore, electron injection into a mesoporous TiO_2 electron transport layer (ETL) occurs in less than 1 ps, however the sluggish electron mobility of the intrinsic TiO_2 impedes mobility and leads to unbalanced charge transport. Mobilities of 7.5 cm^2/Vs for holes and 12.5 cm^2/Vs for electrons were measured by Ponseca et al. at THz frequencies, and 2 cm^2/Vs and 1 cm^2/Vs in the microsecond range, respectively, yielding an electron-to-hole mobility ratio of approximately 2.0, very much in agreement with computational calculations (discussed in the coming section) [28,78]. In another report, a perovskite-based thin film transistor (TFT) was fabricated to observe the ambipolar semiconductor behavior in the film, where the hole transport mobility was calculated to be 10^{-5} cm^2/Vs in the device [84]. The mobility of electrons compared to holes in pure perovskite films presents significant reasoning as to why performances in Al_2O_3-based devices are comparable to those based on TiO_2.

Electronic structure

Studies on the electronic structures of 2D and 3D perovskite structures have shown that the electronic levels for hybrid perovskites consist of an antibonding hybrid state between the B-s and X-p orbitals that correspond to the valence band maximum (VBM) and a non-bonding hybrid state between the B-p and X-p orbitals that determines the conduction band minimum (CBM) (Fig. 2.7) [25—29]. In 2004, Park and Chang conducted first-principles pseudopotential studies on electronic properties of $MAPbX_3$ and $CsPbX_3$ [25]. It was demonstrated that the electronic levels of MA lie deep within the valence and conduction bands (VB, CB), indicating that the contribution of MA toward electronic properties is miniscule and that the resulting band edges stem primarily from the BX_6 octahedra. Thus, it is apparent that band structures are only slightly affected by change from organic (MA) to inorganic (Cs) A cations as a result of size effects. The electronic states are however affected by substitution of the halide component, such that a VB transition from $3p \rightarrow 4p \rightarrow 5p$ occurs for substitution of $Cl \rightarrow Br \rightarrow I$. This accordingly lowers the ionization potential (binding energy) [26]. Furthermore, the electronic band structure of hybrid perovskites has an associated pressure-dependence, for which a redshift in the energy gap occurs as a result of an increase in pressure. This is due to the antibonding and non-bonding natures of the VBM and CBM, respectively, which are pressure-sensitive. This is quite peculiar as it is in contradiction with most semiconductor materials [26].

More recently, Umari and company demonstrated an accurate Spin—Orbit Coupling-GW (SOC-GW) model to compensate for underestimates seen in previously inconsistent

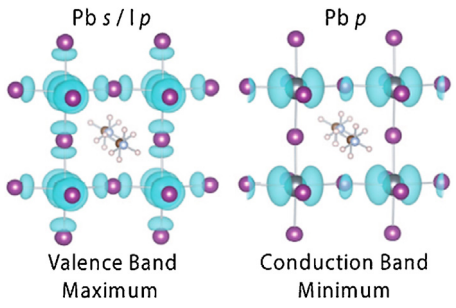

Figure 2.7 Representation of the orbital arrangements for $MAPbI_3$ (a) VBM, showing Pb-s and I-p orbital overlap, and (b) CBM, showing Pb-p orbitals [27].

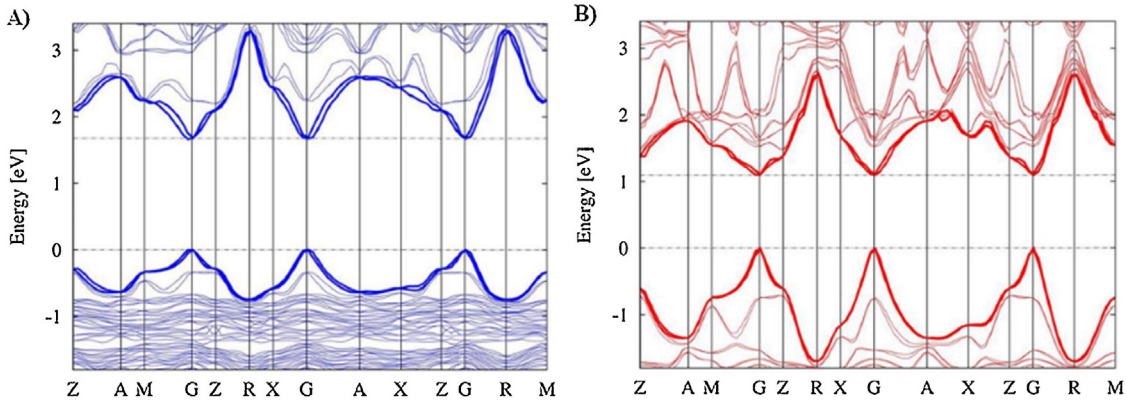

Figure 2.8 Calculated band structures for (A) $MAPbI_3$ and (B) $MASnI_3$ using the SOC-GW method. $MAPbI_3$ shows an unfavorable increase in band gap due to relativistic effects [28].

Density Functional Theory (DFT) electronic structure methods [28]. $MAPbI_3$ and $MASnI_3$ were investigated, revealing that relativistic effects are responsible for the variations seen in electronic properties. These relativistic effects, while improving stability of $MAPbI_3$ toward oxidation, also come with an unfavorable increase in band gap. Their results produced band gaps in agreement with experimental values, yielding a ± 0.1 eV uncertainty (Fig. 2.8). The calculated maximum short circuit current (J_{sc}) was 25 mA/cm^2 compared with the experimentally determined value of 28 mA/cm^2 and the highest achieved J_{sc} values for $MAPbI_3$ reached 21 mA/cm^2 due to reduced absorption efficiency in the 600—800 nm range. It was thought that approximately 0.2 eV difference between $MASnI_3$ and $MAPbI_3$ is attributed to structural differences, i.e. degree of BX_6 octahedra tilting.

Density of states

An analysis of the density of states (DOS) was conducted by Umari et al. to provide a better understanding of the reduction in band gap variations. It depicts an additional peak for states within $MASnI_3$ extending from the main VB peak not seen for $MAPbI_3$. This feature is largely attributed to the I-p states, however antibonding interactions of Sn-5s and I-5p orbitals also have significant contributions. Likewise, the Pb-6s orbitals are seen at a much lower energy level and thus are less inclined to interact with I-5p orbitals and constitute the rapid increase of the VB of $MAPbI_3$ compared to $MASnI_3$. Pb and I are heavy atoms, such that the 5s/6p shells in Sn/Pb stabilize the Pb-6s orbital rendering it less likely to react or share its electrons (6s inert pair effect). As such, relativistic effects, that is, spin—orbit coupling, must be included in quantitative analysis of electronic band structure [26,28]. This results in an increased the band gap compared to that of $MASnI_3$ as the VB shift is approximately 0.5 eV greater than the CB shift.

Effective mass

Park and Chang first investigated electronic properties of $MAPbX_3$ (X = I, Cl, Br), and calculated effective masses in $MAPbBr_3$ for electrons and holes at the CBM and VBM to be $m_e^* = 0.25m_0$ and $m_h^* = 0.12m_0$ (where m_0 is the mass of an electron), respectively [25]. These values are comparable to those seen in other semiconductors, e.g. GaAs, for which $m_e^* = 0.066m_0$ at CBM and $m_h^* = 0.05m_0$, $0.08m_0$ for heavy and light holes at VBM, respectively. It was found that the effective mass of a hole at the VBM was lower than that of an electron at the CBM. In using an organic cation, effective masses were slightly larger than those when using an inorganic one (Cs) due to larger lattice constants. Thus, m^* for holes at the VBM for $MAPbBr_3$ and $MASnBr_3$ were $0.15m_0$ and $0.12m_0$, respectively. It was also found that for 2D perovskite structures the band gap decreased due to a carrier confinement effect as a result of increased number of stacked perovskite layers.

Further theoretical studies have shown maximum effective masses for pseudocubic $MAPbI_3$ with values of $m_e^* = 0.23m_0$ and $m_h^* = 0.29m_0$ incorporating SOC effects [77]. The simulation results, for the first time, explain the ambipolar carrier transport characteristics in perovskite solar cells. However, these effective masses are for an ideal case not including scattering effects due to phonons, defects, or impurities. Effective masses of hybrid perovskites are thus comparable to those seen in silicon ($m_e^* = 0.19m_0$, $m_h^* = 0.53m_0$, $0.16m_0$ for heavy and light holes, respectively).

More recent theoretical studies by Umari and company have demonstrated an improved accuracy in theoretical modeling closer to obtained experimental values using a SOC-GW method [28]. Relativistic effects significantly affect band dispersion, most prominently observed in the case of the VB of $MAPbI_3$ in comparison to $MASnI_3$. This feature is reflected by the calculated effective masses seen for various symmetries across the band structure. Thus, it is clear that $MASnI_3$ ought to provide improved hole transport and accordingly reduced electron transport compared to $MAPbI_3$.

Other properties

Ferroelectric

Ferroelectric materials present beneficial effects for PV applications as their strong symmetry breaking, due to spontaneous polarization, can result in enhanced charge carrier separation upon photoexcitation and allow for increased carrier lifetime and attainable voltages exceeding the band gap [26,85,86]. Hybrid perovskites have shown to exhibit spontaneous electric polarization through ferroelectric

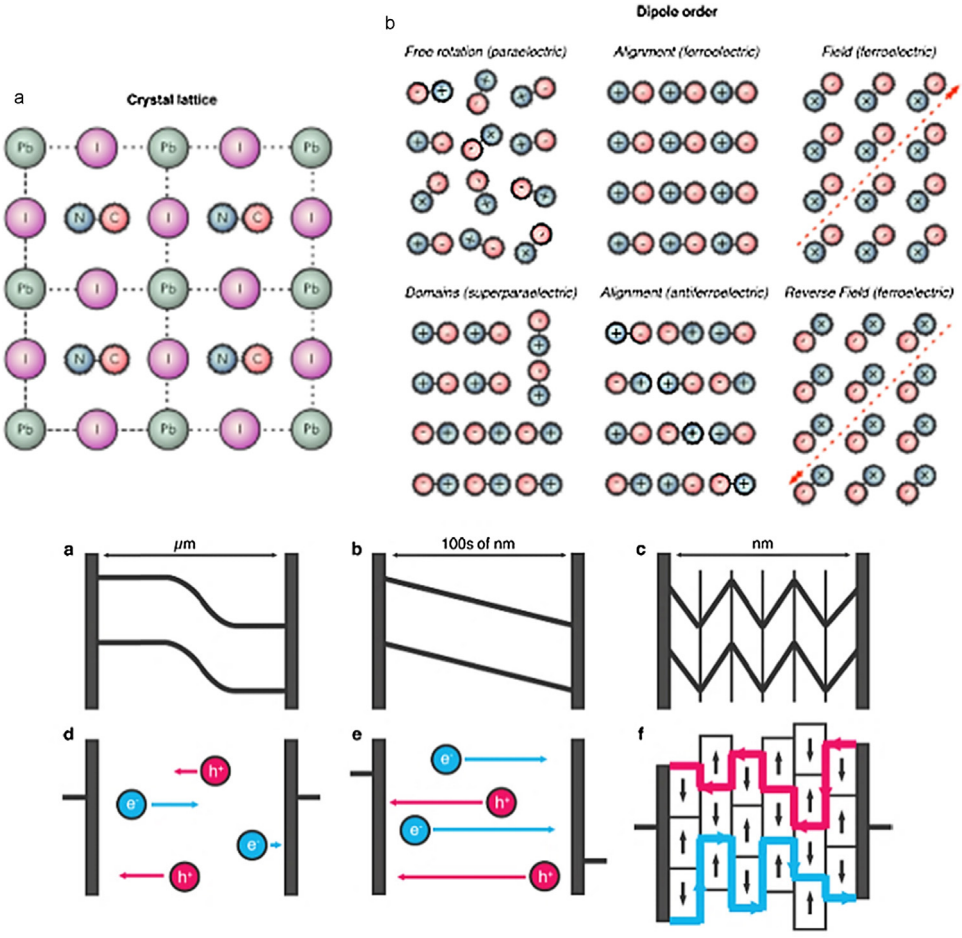

Figure 2.9 Top: Representation of the ionic components of the $MAPbI_3$ crystal lattice and (b) possible dipole order within $MAPbI_3$ crystals. Bottom: free carrier motion in (a) traditional p—n junction (b) hybrid perovskite film, and (c) ''ferroelectric highways'' produced by ferroelectric polarization [26].

domains inducing internal electric fields that may assist in separation of photoexcited charge carriers, effectively reducing recombination and facilitating charge extraction. The spontaneous electric polarization arises from migration of the B cation from its central location within the BX_6 octahedra that causes a disruption of symmetry [26]. This effect is attributed to asymmetry of the organic cation, which prevents the presence of any inversion center in the structure. The flexibility of the crystal structure allows for rotation of the polar organic cations that results in a transition from paraelectric to ferroelectric ordering. Such effects would enhance electron hole separation and consequentially improve carrier mobility, charge extraction efficiency, and performance. A schematic representation of various possible dipole ordering of organic cations is provided in Fig. 2.9a.

Ferroelectric domains may provide support for the free carrier charge generation in hybrid perovskites previously claimed [87]. Frost and co-workers have proposed the idea of ''ferroelectric highways,'' in which charge carriers of a given type may travel unimpeded by carriers of the opposite charge (Fig. 2.9) [26]. This in turn would reduce recombination and may explain the long carrier diffusion lengths observed. Switchable photocurrents have also been observed in hybrid perovskites as a result of p—i—n junctions formed via ion drift. As such, these devices produce a scanning-history-dependent photocurrent that may be a contributing factor to the observed hysteresis (discussed in the following sections) [88].

Thermal conductivity

Relatively little work has been done in regards to thermal considerations for hybrid perovskites. Recently, a temperature dependence of thermal conductivity in crystalline perovskite has been investigated. Pisoni et al. reported ultra-low thermal conductivities ($0.5\,Wm^{-1}\,K^{-1}$) for single and polycrystalline hybrid perovskites, demonstrating that heat transport is primarily attributed to phonon interaction and rotational degrees of freedom of the methylammonium cations [89]. Such a low κ will prevent the rapid spread of the light-converted-heat, which can cause mechanical stresses and limit the lifetime of the photovoltaic device.

PV applications

The interest in organic—inorganic hybrid halide perovskites has been largely renewed due to the staggering increases in performances of perovskite-based solar cells. Featuring

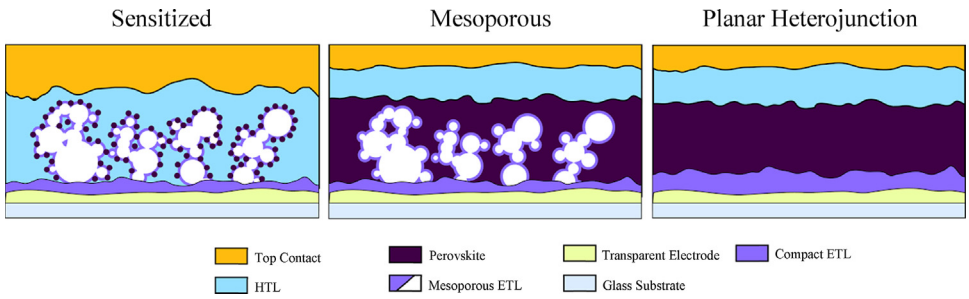

Figure 3.1 Three major groups of perovskite solar cells categorized based on the deposition sequence.

exceptional properties, these materials may revolutionize the field of renewable energy with affordable, yet efficient solar cells able to compete with silicon PV technologies. In this section, we carefully review the recent progress in hybrid perovskite solar cell development. Here we summarize the various device architectures ('Device architecture' section) and current understanding of device working principles ('Working mechanism' section). The major achievements contributing toward the rapid enhancement in device performances pertain to perovskite thin film growth ('Film formation' section) and relevant interface engineering ('Interface engineering' section). Perovskite tandem devices are expected to be the most promising technology for the commercialization of perovskite materials, whose efforts will be discussed ('Tandem devices' section). In addition, we speculate on some open issues and pitfalls of perovskites that are currently under debate in the photovoltaic community, mainly, stability and hysteresis ('Stability' and 'Hysteresis' sections). Due to the recent rapid increase in number of presentations and published articles on perovskite solar cells, in this review we focus on a thorough, but not exclusive, illustration of research landscape.

Device architecture

The perovskite absorber $MAPbI_3$ was initially used in dye sensitized solar cells (DSSC) to replace conventional dyes [15]. After its successful embodiment in solid state DSSC, perovskite materials have attracted great interest in the PV research community [17]. These device configurations feature semiconducting mesoporous TiO_2 scaffolds, which have been intensively studied for DSSCs. At nearly the same time, devices with insulating scaffolds of Al_2O_3 were reported to achieve decent PCEs. Further investigations have found perovskites absorbers to exhibit superior ambipolar transport of both electrons and holes, which indicates that mesoporous scaffolds in perovskite solar cells are not necessary. Planar heterojunction perovskite solar cells fabricated via thermal vapor deposition have demonstrated respectful efficiencies over 15% [7]. The implementation of planar configurations in perovskite solar cells assures further adoption of thin film PV techniques that have been developed over past decades [4]. In addition to their unique optoelectronic properties and organic—inorganic hybrid nature, the versatility of perovskites in device architecture and processing techniques has been a main contributor to its extremely rapid development. The major device designs employed for perovskite solar cells can be roughly categorized in into three groups based on the processing sequence, as illustrated in Fig. 3.1.

In a typical design, a several hundred nanometer thick perovskite absorber layer with or without a scaffold is sandwiched between an electron and hole transporting layer (ETL, HTL). Upon absorption of incident photons, carriers are created within the absorber and subsequently travel through a transport pathway designated by the ETL/HTL, electrodes, and interfaces [8]. Carrier transport layers serve as electrode buffers for selective carrier extraction. However, in some scenarios devices have been reported to achieve reasonable efficiencies without either an ETL or HTL [18,90]. Electrode materials are limited in choice due to diffusivity and chemical reactivity with the perovskite absorber. The following section will cover the versatile architectures seen for perovskite solar cells, with a detailed discussion regarding the major components that determine device configuration.

Initially, perovskites were incorporated as quantum dots to anchor onto 2 μm thick TiO_2 scaffolds, mimicking the architecture from which they were first employed, the DSSC (Fig. 3.1) [16]. Perovskite sensitizers were initially used to replace the standard N917 dye sensitizers for aqueous, and later solid-state, DSSCs that achieved promising performances [15]. The devices achieved higher efficiencies when reducing the thickness of the scaffold and increasing the loading of the absorber materials. These results developed the foundation for what was to come in the explosive progress of perovskite photovoltaics in terms of versatility in device architecture and efficiency. As intrinsic properties of perovskites were revealed through its development it was realized that their contributions may extend beyond that of a sensitizer. Consequentially, other various device architectures were explored to improve device performances.

The mesoporous scaffold

One of the most popular device architectures of perovskite solar cells, the mesoporous structure (Fig. 3.1), follows that of a solid-state DSSC. A typical device contains a fluorine doped tin oxide (FTO) glass substrate covered by a compact TiO_2 ETL (~80 nm). A mesoporous TiO_2 scaffold (~350 nm) is constructed on top of the compact TiO_2 layer, followed by the infiltration of a perovskite absorber. Subsequently a HTL is deposited, most commonly the hole conducting polymer spiro-OMeTAD (~200 nm). Finally, a thin layer of gold (~100 nm) is generally deposited as the top electrode [6]. Further optimization has been reported in devices with an

overlayer of perovskite on top of the TiO_2 scaffold [91]. It is now widely acknowledged that a perovskite film of ~350 nm can absorb a majority of the incident photons, regardless of the scaffolding [92]. However, it has also been noted that the *J*—*V* hysteresis behavior observed in devices is affected by the thickness of the TiO_2 scaffolds [93].

As perovskite solar cell architectures originated from DSSCs, it is not surprising that they most commonly employ a TiO_2 based scaffold. Thus, several scaffolding approaches have been demonstrated for various TiO_2 building blocks that include nanowires [80,94], nanorods [95,96], nanocones [97], nanofibers [98], nanotubes [99], and nanohelices [100]. The morphology of the scaffold affects light scattering and perovskite loading that ultimately determines the short circuit current (J_{sc}). In addition, charge injection and diffusion are not the same across different types of TiO_2 scaffolds, which correlate to device performance through variation of open circuit voltage (V_{oc}) and fill factor (FF). Block co-polymers have also been introduced to create mesoporous TiO_2 scaffolds with different morphology [101]. In addition, TiO_2 based composites have been implemented into perovskite solar cells. Graphene—TiO_2 nanocomposites have been proposed to benefit performance resulting from higher conductivity and better electrical contact of carbon materials for electron transport. Reduced graphene oxide [102] has been blended with TiO_2 nanocrystals to create efficient ETL scaffolds that have lead to a remarkable efficiencies over 15%. TiO_2—WO_3 nanosheet arrays have also been reported recently, where the introduction of TiO_2 layers dramatically increases the PCE of devices based on WO_3 scaffolds [103]. Moreover, nanocrystalline TiO_2 integrated with other metallic elements [94,96,104] have also been demonstrated. The improvement in device performance is attributed to the improved absorber morphology and enhanced electron transfer across the mesoporous scaffold. It has also been reported that metal substitution may affect the surface states of TiO_2 [104]. Since TiO_2 has been reported to possess surface states located in the mid-gap [105], much work has been dedicated to surface passivation along the TiO_2—perovskite interface. A detailed discussion is presented in 'Interface engineering' section.

Zinc oxide (ZnO) has proven to be a feasible alternative to TiO_2 for perovskite solar cells due to its comparable energy levels and sufficient electron transport properties. ZnO based mesoporous scaffolds, mainly comprised of nanorods, have been constructed through various approaches [106—111]. Current results suggest that ZnO nanorods provide an effective charge collection system in $MAPbI_3$ devices [109]. However, it is also worth noting that carrier recombination issues reside at the interface between perovskite and ZnO that are suspected to affect device efficiency. A PCE over 12%[112] has been achieved in devices based on ZnO mesoporous scaffolds fabricated via electrostatic spraying, where Al doped ZnO was observed to increase carrier transport within the ETL and correspondingly improved the V_{oc} and FF.

Apart from the conventional ETL materials (e.g. TiO_2 and ZnO), perovskite oxide $SrTiO_3$ (STO) has been employed to construct a mesoporous scaffold [113]. Steady-state photoluminescence (PL) quenching and transient absorption experiments revealed efficient photoelectron transfer from $MAPbI_{3-x}Cl_x$ to STO, corresponding to an improved V_{oc} of the working device. This suggests STO as a competitive ETM candidate for perovskite solar cells.

In addition to semiconducting n-type materials, p-type semiconductors, mainly NiO, can also be used to fabricate mesporous scaffolds [114,115]. In this configuration, a compact layer and mesoporous scaffold based on NiO are subsequently deposited onto a FTO substrate, establishing a hole transport pathway. PCBM/Al or a carbon electrode is generally employed for electron collection. In a recent report, a layered mesoporous scaffold successively assembling both n-type TiO_2 and p-type NiO has been shown [116]. The device exhibited extended electron lifetime and improved hole extraction of the counter electrode, leading to a PCE of 11.4%.

Another interesting development in the architecture of perovskite solar cells is the replacement of the n-type TiO_2 mesoporous scaffolds with an Al_2O_3 insulating material, so-named a ''mesosuperstructured architecture'' (Fig. 3.1) [19]. The employment of an Al_2O_3 scaffold revealed superior optoelectronic properties of perovskite, which encouraged the use of planar configurations in perovskite solar cells. Smaller V_{oc} loss and longer electron lifetime are reported in Al_2O_3 based devices, which is attributed to reduced surface states at interfaces. Introducing Al_2O_3 to replace TiO_2 shows promise to circumvent the instability of TiO_2 in perovskite solar cells under UV illumination [117]. It is also observed that the Fermi energy of perovskites show significant discrepancy when deposited on Al_2O_3 comparing to those without scaffolds [118]. The authors correlate the enhanced device performance to the fast filling of the subtrap states aided by the Al_2O_3 scaffold. In addition, superior device performance has attracted quite a lot of efforts to investigate the processing of Al_2O_3 scaffolds, including low temperature processing [119,120], copolymer-directed processing [121], and blending with metal nanoparticles to introduce plasmonic effects [122]. ZrO_2 [54,123] and SiO_2 [124,125] have also been employed as mesoporous scaffolds.

The planar heterojunction

The perovskite materials proven to assume all of the principal roles of PV operation, thus planar configurations (Fig. 3.1) have been developed as another category of important architectural design. It can be roughly subcategorized into two groups, n—i—p and p—i—n, based on the processing sequence (see Fig. 3.1). A typical n-i-p configuration is glass/TCO/ETL/perovskite/HTL/metal, while the p—i—n pertains to an inverted structure that follows glass/TCO/HTL/perovskite/ETL/metal. Due to the simplicity of planar configurations, efforts have been focused on (a) material selection for the appropriate HTL/ETL and interface engineering ('Interface engineering' section), and (b) deposition techniques to produce high quality films ('Film formation' section). Devices based on planar configurations have attracted an large portion of research efforts as they provide enhanced versatility for device optimization and ease of multijunction construction, potential low costs for mass production, and ease of investigation of underlying device physics.

Generally, the ETL/HTL helps to provide interfaces for selective carrier extraction. Curiously, working devices have been obtained with comparable performances even

when one carrier transport layer was omitted. Devices without a HTL have been reported by several groups [18,54,116,126—133], for which it is claimed that the most commonly employed HTL, spiro-OMeTAD, is unnecessary and may be omitted from the device configuration as it is one of the more expensive components. Gold and silver electrodes are often applied for selective hole collection in most devices, however silver is becoming used less as it has proven to be chemically reactive with perovskite. Nickel has also been reported as a metal contact [134]. More recently, carbon-based electrodes have been investigated for low-cost electrodes and have shown improved chemical stability [54,116,133,135—138]. Removal of the ETL has also been demonstrated where to substantially simplify the device fabrication process [90], where decent PCEs have been achieved due to highly efficient hole extraction at the HTL interface. This results in a depletion of holes within the perovskite film, limiting the opportunity for bimolecular recombination. This concept provides a reliable platform to study device operation mechanisms and interfacial contributions.

Other configurations

Interestingly, organic bulk heterojunctions have been incorporated into the perovskite solar cells to replace the HTL/ETL [139,140], as shown in Fig. 3.2. The integration successfully expands the light harvesting spectrum to the lower edge, clearly evidenced to contribute to the photocurrents as indicated by EQE measurements. Carrier recombination within the integrated perovskite/BHJ device has been investigated, indicating no substantial space charge build-up and that charge carrier losses in the absorber bulk are dominated by monomolecular recombination via defects, where bimolecular recombination is a rather minor loss. In addition, the integrated devices have shown longer photocurrent response times than regular devices, which is attributed to the slow charge collection. Moreover, the demonstrated device successfully harvests sunlight in IR region, which provides a feasible approach to further improve efficiency in perovskite based solar cells. Indeed, this type of configuration is still in its infancy with several unanswered questions regarding its operational principles.

Interestingly, fiber-shaped perovskite cells have also been reported [141]. A stainless steel fiber employed as an electrode was coated successively by compact TiO_2, mesoporous TiO_2, perovskite and spiro-OMeTAD. Carbon nanotube sheets were woven to serve as the top electrode. The device exhibited a PCE of 3.3% and could be further woven for electronic textiles [141].

Flexible and light weight thin film solar cells have attracted considerable attention due to their convenience of integration and versatile functionality. Efforts have been extracted to fabricate perovskite solar cells on flexible substrates coated with a transparent conductive oxide (TCO). These flexible transparent electrodes include poly(ethylene terephthalate) (PET)/ITO, polyethylene naphthalate (PEN)/ITO, PET/IZO, PET/AZO/Ag/AZO, etc. [71,106,142—149]. Titanium foil has also been employed as both a substrate and electrode, coupled with a transparent conductive carbon nanotube network as the top transparent electrode [138]. Some flexible perovskite solar cells revealed fairly promising mechanical bending stability [142], maintaining 100% PCE throughout 1000 bending cycles via R400. Devices using R10 also exhibited no significant decrease in PCE, retaining over 95% of the initial value.

Similar to other PV technologies, the architecture of perovskite solar cell is always an important issue, which might affect the device in terms of performance, stability, and cost, and eventually determines the commercialization of this technology. Different from other PV technologies however, the uniqueness of this materials have assured the versatility in adopting various device configurations, which are oriented from not only materials properties but also application requirements. Importantly, the perovskite PV is still in its early stage, so there is not a prevailing technology that dominates the market. It is thus open that any new possibility of device architecture, which fits either main or niche market. In considering the research growing community with continuous investment of efforts and resources, it is expected an optimal device configuration will achieve over the recent years that fulfill the demands of performance, stability and cost for perovskite solar cells.

Working mechanism

With the rapid progress in device efficiency, substantial efforts have been made to understand the underlying mechanisms that govern the operation of perovskite solar cells. This section summarizes some of the key achievements.

Photo-excited species

One of the central questions of perovskite based semiconductors is whether the photoexcitation species are free carriers or excitonic. Excitonic materials, consisting of tightly bound excitons, give rise to fast recombination rates and high emission quantum yields. Hence, they are potentially more suitable for light emitting diodes or lasers. Free carrier based materials are more promising for photovoltaic cells, since electrons and holes must be separately collected. Generally, the binding energy between electrons and holes increases as the dimensionality is reduced due to the quantum confinement effect. When the radius of a cation is larger than its limit for cubic packing a perovskite transitions from 3D to 2D occurs giving rise to excitonic binding.

The exciton binding energy for the 3D perovskite adopting the relatively small $CH_3NH_3^+$ cation is reported in the range of 19—50 mV [150], much smaller than those for common organic semiconductors by several hundred meV. As perovskites have achieved comparable efficiencies for various architectures, they are suggested to function as excitonic absorbers but with the high performances seen in inorganic thin film semiconductors. However, significant interplay between exciton and free carriers ought to exist given the 26 meV of the characteristic thermal energy at room temperature. Experimental evidence is given by both steady state and transient absorption and photoluminescence spectra showing a temperature and excitation intensity dependence [150]. An accurate estimation of the exciton binding energy is challenging. This value was calculated based on temperature dependent PL measurements, assuming that the integrated PL intensity decreased as temperature increased

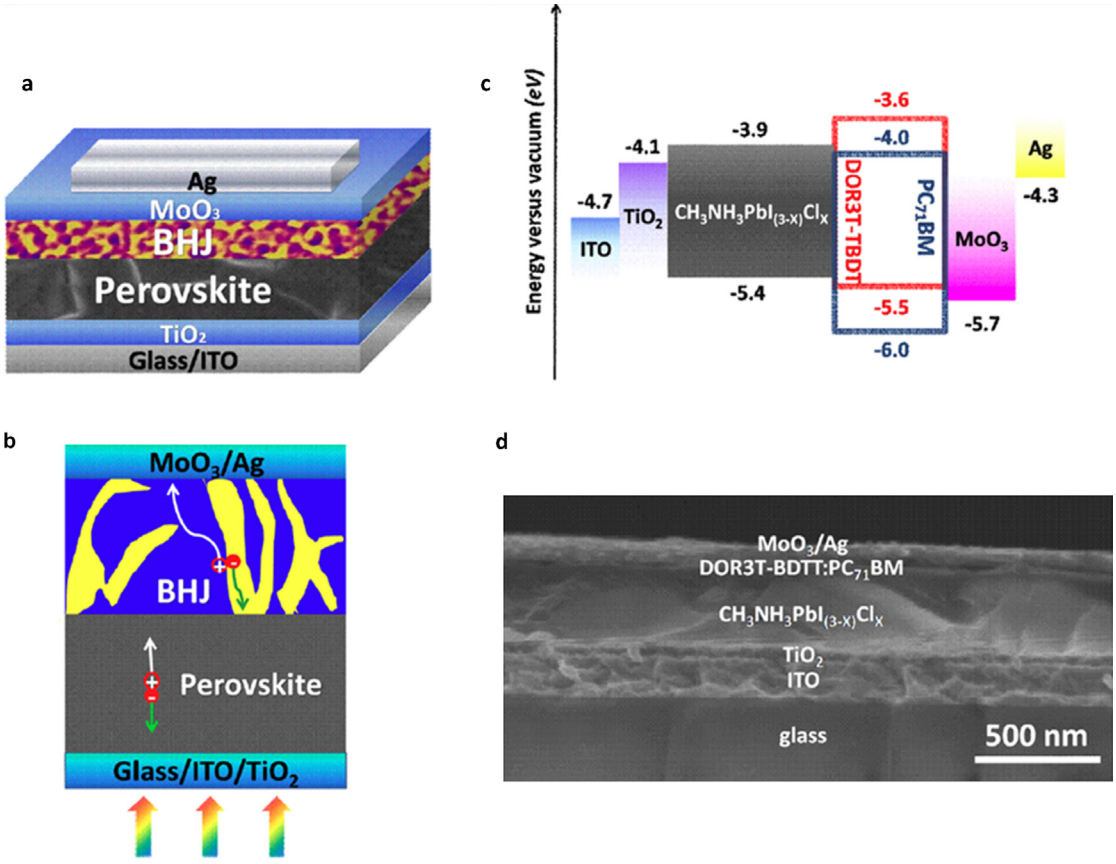

Figure 3.2 Integrated perovskite/BHJ device depicting: (a) schematic of the cross sectional structure (b) charge generation and transport mechanism, (c) energy diagram, and (d) SEM image of the cross-section.
Source: Adapted with permission from Ref. [139].

due to thermal dissociation of the exciton. Such assumptions may be invalid without investigating PL dynamics, since nonradiative recombination channels are more active at higher temperatures which and would ultimately reduce PL intensity.

The most reasonable estimation is presented by temperature dependent absorption measurements as shown in Fig. 3.3, for which ~50 meV exciton binding energy is estimated [87]. However, it should be noted that photoexcitation species and exciton binding energies may vary based on morphology or crystal size. The absorption spectra for mesoporous and planar perovskite structures present difficulties. Excitonic absorption peaks are observed for large perovskite crystal samples and become very clear at low temperatures. On the other hand, mesoporous perovskite with smaller crystals exhibit distinct free carrier absorption characteristics at low temperatures.

The photophysics of perovskite are not yet fully understood. Continuous research efforts on this topic will generate profound impacts in guiding future perovskite-based optoelectronic technologies. Manser and Kamat observed band filling in $MAPbI_3$ and proposed that free charges accumulate at band-edges to further reduce exciton binding energies via columbic screening of photo-generated electron–hole pairs [151]. One of the most intriguing aspects of hybrid perovskites are the dipole moments induced by the cation, which distinguishes them among all traditional semiconductors. Most inorganic perovskites display spontaneous electric polarization, particularly pronounced in hybrid halide perovskites [26]. A spontaneous polarization induced built-in electric field is presumed to facilitate exciton separation upon photoabsorption. This may explain the physical origin of the low exciton binding energy in halide perovskite materials. The strong lattice polarization has potential advantages for enhanced charge separation, reduced recombination loss and improved carrier lifetimes.

Defects and band structure

One merit of the hybrid halide perovskite semiconductor is their unexpected long carrier lifetimes and long carrier diffusion lengths. Moreover, perovskite semiconductors also show very efficient photoluminescence quantum yield and even optically pumped lasing effects [152,153]. The high emissive quantum yields and long carrier lifetimes indicate that nonradiative recombination channels are strongly inhibited, strongly suggesting its application in PV. Yin et al. studied the defects of perovskites through DFT calculations on the perovskite structure [154,155]. Hybrid perovskites are typically composed of the following three ions: positively charged methylammonium (MA^+), lead (Pb^{2+}), and negatively charged iodide (I^-). Interestingly, the defects with the lowest formation energies are Pb^{2+} vacancies and interstitial MA^+. However, both create shallow charge-carrier

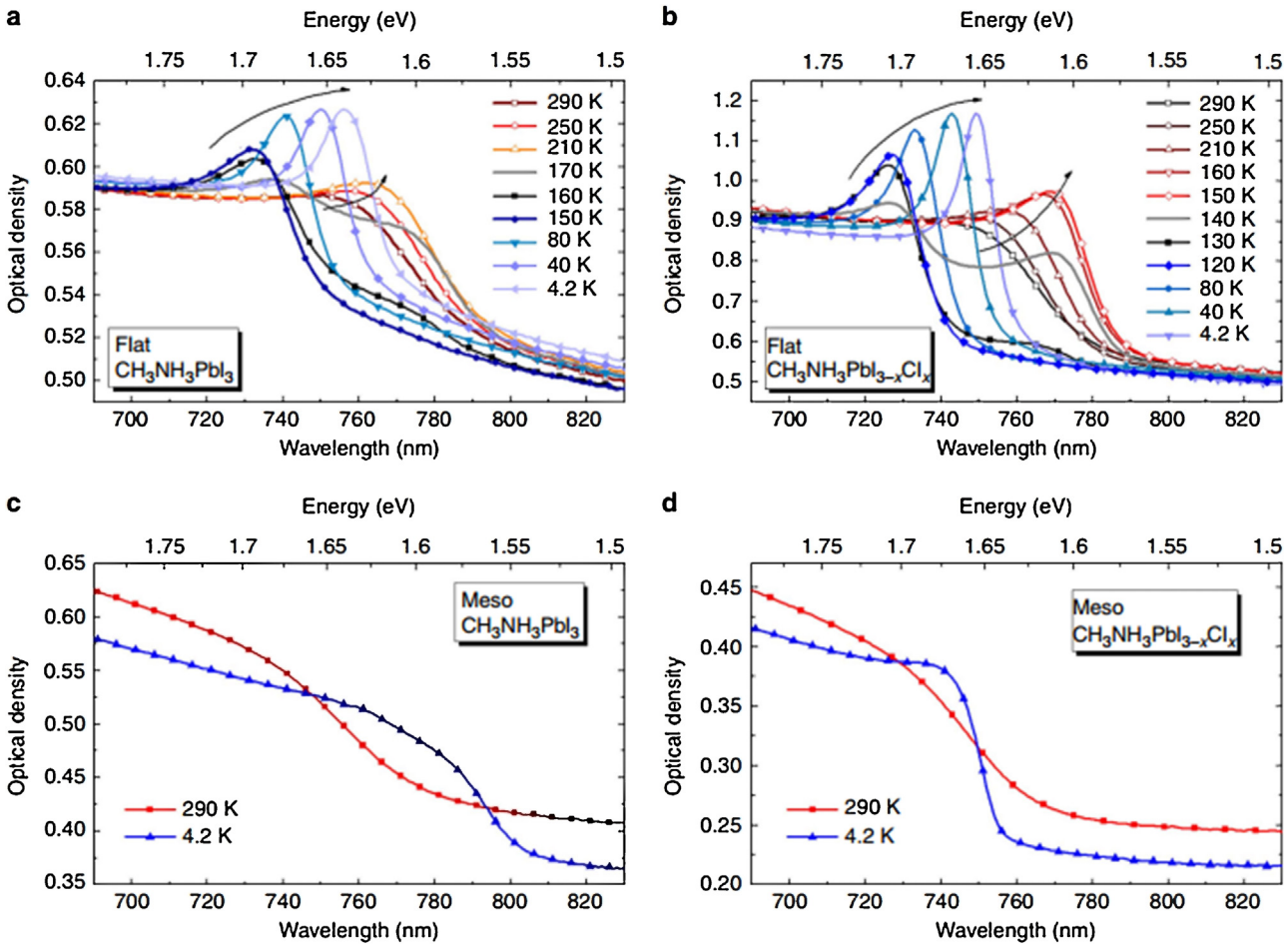

Figure 3.3 Temperature dependent absorption spectra of mixed halide perovskites. Absorption spectra of $CH_3NH_3PbI_3$ and $CH_3NH_3PbI_{3-x}Cl_x$ as a function of temperature (290—4.2 K). (a, b) Thin films on a glass substrate and (c, d) on a mesoporous Al_2O_3 substrate.
Source: Adapted with permission from Ref. [87].

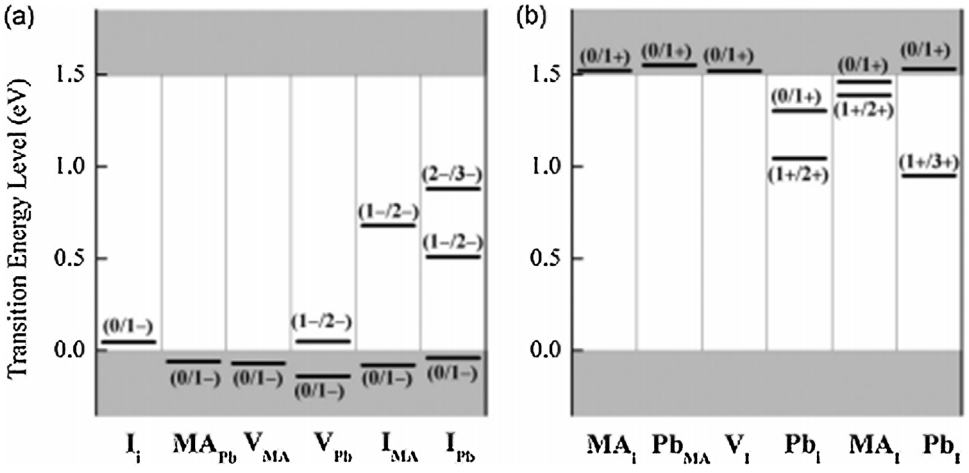

Figure 3.4 Energy levels of $MAPbI_3$ perovskite depicting defect states calculated by DFT: (a) acceptor and (b) donor states resulting from intrinsic defects.
Source: Adapted with permission from Ref. [155].

trap states near the perovskite band edges as shown in Fig. 3.4. Such shallow defects do not serve as nonradiative recombination sites as do deep defects with energy levels near mid-bandgap, as have been experimental observed [156,157]. However, simulation results also predict that films grown under iodine-rich conditions are prone to a high density of deep electronic traps (recombination centers) [158]. This finding explains the larger charge diffusion lengths observed in perovskites prepared using iodide-free precursors.

To some extent, the lack of deep trap states within the band gap of the perovskite band structure explains the long carrier lifetimes. Pb vacancies are electron acceptors while the interstitial MA^+ ions are electron donors. Both types of defects are highly sensitive to preparation methods. Furthermore, preparation methods determine whether perovskites are p-type or n-type. However, it should be noted that the above theoretical studies indicate that grain boundaries do not introduce deep defect states, but that the interface states between the perovskite and HTL/ETL, e.g. TiO_2, spiro-OMeTAD, PCBM, etc., could potentially be detrimental serving as interfacial recombination sites [159]. There have been a few reports regarding passivation of such surface states [160—162].

Understanding the band structure of perovskite semiconductors is no trivial task. The Fermi level is affected by interaction with the mesoporous scaffold, which may correlate to sub-gap electronic trap sites [118]. Both the mesoporous TiO_2 and Al_2O_3 scaffolds appear to raise the Fermi level of the perovskite to just below (~50 meV) the conduction band, while the neat solid perovskite film on fluorine-doped tin oxide (FTO) glass appears to have the Fermi level near the middle of the band gap. In the other reports, it was found that $MAPbI_3$ could be either n- or p-doped by changing the ratio of MAI to PbI_2 [163]. An increase in the intrinsic bandgap that follows the Burstein—Moss band filling model has been observed, which is attributed to charge accumulation within the perovskite films [151].

Carrier dynamics

The hybrid perovskite semiconductor is attractive due to its long and balanced charge carrier diffusion length, which is in sub-micrometer range [64,82]. A charge carrier mobility of ~10 cm^2/Vs is estimated as the lower bound of the methylammonium lead trihalide based on the THz photoinduced absorption transient spectroscopy [164], in agreement with time resolved microwave conductivity measurements [78,165] and excitation density perturbation analysis [118]. The bi-molecular recombination rate to charge mobility ratio is over four orders of magnitude lower than that predicted from Langevin theory. This unique property is likely to arise from spatial separation of electrons and holes within the metal-halide structure or across a crystalline domain. It must be noted that mobilities extracted thus far are based solely on the perovskite film, however, the effective mobility within the actual device may be lower than these reported values when considering the interfacial effects. It is desirable to directly measure effective charge carrier mobility within full devices in the future.

Apart from an understanding of carrier transport within the perovskite film, efforts have been devoted to illustrate the photovoltaic process across the entire perovskite solar cell. Carrier generation and charge dissociation has been clearly detailed, where the electron—hole pairs are generated almost instantaneously after photoexcitation and dissociate in 2 ps forming highly mobile charges [78]. The photocarrier dynamics are well described by a simple rate equation including single-carrier trapping and electron—hole radiative recombination, where a free-carrier model is proves superior than an exciton model for interpreting optical properties [166]. In addition, the observation of both hole injection into the HTL and electron injection into the ETL have been reported by using ultrafast spectroscopy in the near-infrared region [167]. Charge accumulation has been discovered and confirmed by impedance spectroscopy and transient photoluminescence spectroscopy independently [151,168], which affects the band edge shift in the perovskite crystal and the capacitor behavior of the PV device.

Film formation

High performance often closely correlates to film quality of the absorber layer in semiconductor PV devices. In order to obtain high PCEs in perovskite solar cells, it is essential to fabricate high quality films with controlled morphology, crystallinity and corresponding optoelectronic properties. The crystallization behavior entails morphological evolution, which affects charge dissociation efficiency, recombination dynamics, and diffusion lengths in resultant perovskite films. It is highly dependent on several key factors such as deposition method, surrounding environment, precursor composition and solvents/additives used. PCEs exceeding 19% have been realized in devices based on engineering modifications and well-controlled material processing [8,100].

Mesoporous scaffolds provide physical constraints on perovskite crystal dimensions, resulting in the possibility of achieving decent film quality for relatively thick films. One simple approach to deposit perovskite materials is through solution. An important point to note for mesoscopic devices is that an overlayer of perovskite can provide enhanced light absorption and better hole/electron blocking between the ETL and HTL, respectively. The crystals of the perovskite overlayer can provide larger grain sizes, which are necessary for better charge transport [84].

Crystallization dynamics for planar structures are most likely different from those of mesoporous scaffolds as there is a reduced perovskite precursor surface energy and therefore less nucleation sites for film growth [169]. A uniform crystallization process involves two main steps — nucleation and growth. Non-ideal surface energies would result in Volmer—Weber growth, due to the fast growth rate of the perovskite film, resulting in a discontinuous film of large sized grains with holes. Therefore, it is vital to develop effective ways to manipulate nucleation and growth of perovskite crystals in order to achieve optimum film morphology and crystallinity for future applications and scientific studies. In this section, we summarize film fabrication methods to elucidate the specific processes and corresponding device architectures. Herein, we summarize a few strategically important parameters reported to

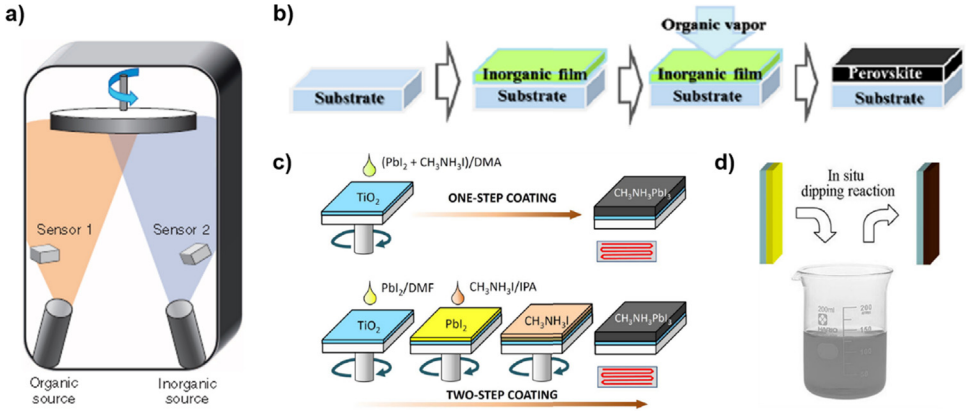

Figure 3.5 The preparation of $MAPbX_3$ films using different deposition methods: (a) dual source co-evaporation using $PbCl_2$ and MAI sources; (b) vapor-assisted solution process using MAI organic vapors to react with pre-deposited PbI_2 films (c) single-step solution processes based on a mixture of PbI_2 and MAI, and sequential coating of PbI_2 and MAI; (d) sequential deposition by dipping the PbI_2 film into MAI solution. Copyright 2013 Nature Publishing Group, 2014 American Institution of Physics, 2014 American Chemical Society.
Source: Adapted with permission from Refs. [6,21,38,176].

control the morphology and achieve high quality films that include precursor stoichiometry, thermal treatment, additives, atmosphere and solvent engineering.

Film formation techniques

Hybrid perovskites can be prepared using different deposition routes and are comprised of two main precursor components: an organic methylammonium halide cation (CH_3NH_3X, X = Cl, Br, I) and an inorganic lead halide species, PbX_2 (X = Cl, Br, I). The preparation methods for perovskite films (Fig. 3.5) using these precursors can be categorized into three processes: (1) vacuum, (2) solution, and (3) hybrid.

Vacuum deposition. In early works, high performance devices (>15% PCE) were achieved by vacuum processes, where the organic and inorganic species were co-evaporated to form uniform planar perovskite films (Fig. 3.5a) [7]. Later, a sequential vapor deposition of $PbCl_2$ followed by MAI was demonstrated with substrate temperatures between 65 and 85 °C to enhance MAI diffusion into $PbCl_2$ [170].

Solution processing. Due to the ease of fabrication and low cost, solution processing routes have been most attractive for preparation of perovskite films. Metal halide and organo-halide species can be mixed for both single-step or sequential deposition at various ratios. Sequential deposition of PbI_2 and MAI solutions onto mesoporous TiO_2 have been successfully demonstrated by Burschka et al. with PCEs greater than 15% (Fig. 3.5d) [6]. Fabrication of PbI_2 framework by atomic layer deposition (ALD) has also been reported [171]. Solution-based processing is favored for devices employing mesoporous scaffolds as the precursors can easily fill the spaces within the pores [172]. While either single-step or sequential deposition can be used for mesoporous structures, single-step precursors cannot form a continuous film for planar configurations due to surface energy and nucleation, as described previously.

To overcome these film coverage issues for single-step deposition in planar configurations, it was shown that molar ratios of 1:3 PbI_2:MAI result in continuous films and consequent device efficiencies over 10% [19]. This method has been widely adopted and was further improved by Zhou et al. to achieve devices with PCEs over 19% [8]. Apart from single-step deposition methods, sequential routes have also been reported by Xiao et al. using PbI_2 and MAI precursors separately, followed by proper thermal annealing for sufficient interdiffusion [173]. Sequential solution deposition techniques provide an alternative route for film formation by further allowing for use of planar architectures (Fig. 3.5c). High performance planar devices with inverted structures such as PEDOT:PSS/$CH_3NH_3PbI_3$/PCBM/C60/BCP/Al were reported to obtain over 15% PCE [174]. Various approaches have been developed to fabricate the hybrids halide perovskite thin films, which is of high value for fundamental study on the re-discovered materials system.

Hybrid vapor-solution process. Building upon these techniques, hybrid methods combining both solution and vapor processes were first proposed and developed by Chen et al. (Fig. 3.5b) [21]. A PbI_2 layer was first deposited in solution by spin coating, followed by a reaction of the pre-deposited PbI_2 film with MAI vapor. The compact layer featured a polycrystalline texture of large grains over 1 μm with small surface roughness. Adopting a similar idea, a chemical vapor deposition growth method, where MAI was reacted with a pre-deposited $PbCl_2$ film, was reported that resulted in a highly stable and scalable process [175].

Precursor stoichiometry

Precursor stoichiometry, particularly the ratio of the organic and inorganic components, largely affects resulting film quality in terms of film conformity and carrier behavior. As mentioned in the previous section, molar ratios of 1:1 and 1:3 have been the most commonly used perovskite precursors. It was reported that for a ratio of 1:3 via solution deposition the mixed halide $MAPbI_{3-x}Cl_x$ exhibits improved film characteristics, e.g. increased grain size, when compared to its pure iodide counterpart [19]. Additionally,

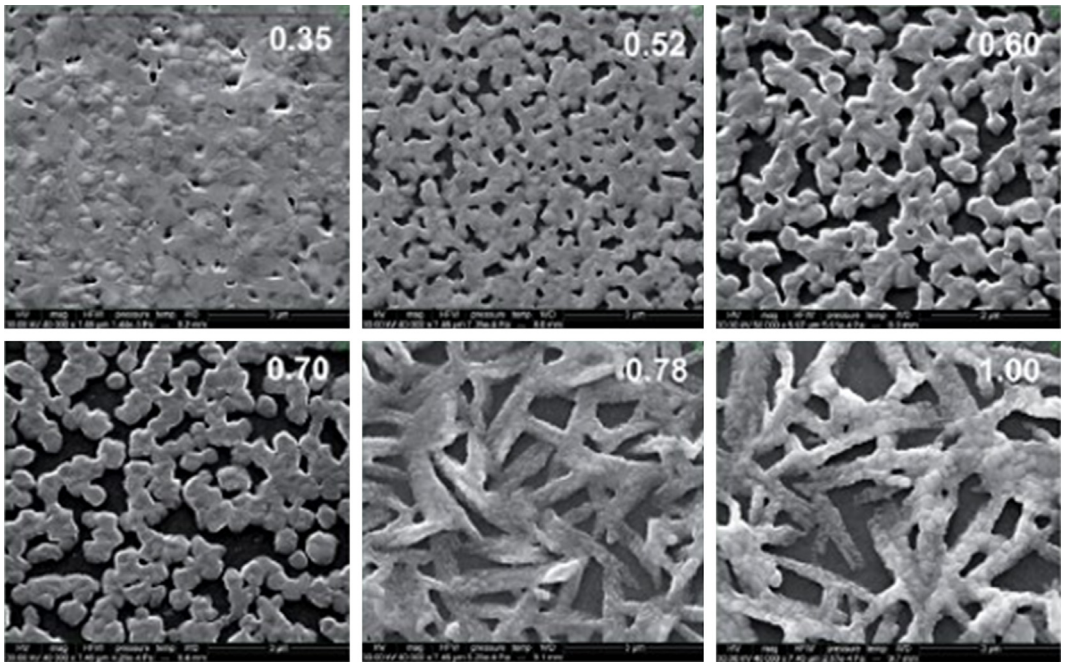

Figure 3.6 The SEM images of the perovskite films prepared from non-stoichiometry of PbI_2 to MAI in DMF solution. Copyright 2014 The Royal Society of Chemistry.
Source: Adapted with permission from Ref. [116].

$MAPbI_{3-x}Cl_x$ films show improved carrier lifetimes of over 100 ns in contrast to only 10 ns seen for $MAPbI_3$ [64]. Thus, dramatically different film qualities originate from precursor stoichiometry that ultimately leads to a difference in device performance.

Studies of stoichiometry effects on film formation have been conducted, in terms of phase formation, underlying reactions, and byproducts. $MAPbI_{3-x}Cl_x$ obtained from $PbCl_2$:MAI (1:3) and $MAPbI_3$ from PbI_2:MAI (1:1) show nearly identical XRD patterns that correspond to a $MAPbI_3$ phase. This suggests that ion exchange occurs between I and Cl during perovskite film formation [19,177]. This observation is also consistent with previous studies on $MASnX_3$ perovskite crystals, where it was shown that iodide and chloride elements cannot form a continuous mixed $MASnI_{3-x}Cl_x$ phase as a result of the extremely low solubility of chloride in the $MASnI_3$ phase [178]. To achieve complete $MAPbI_3$ perovskite formation, three times the amount of MAI to $PbCl_2$ is required. Any stoichiometry deviation from 1:3 ($PbCl_2$:MAI) may cause either excessive MAI or unreacted $PbCl_2$ to remain within the film, which can be expected to degrade optoelectronic performance due to unfavorable film morphology. Zhao et al. have incorporated excess MACl into a PbI_2:MAI (1:1) precursor solution in an effort to modulate perovskite film formation [179]. The authors observed a $MAPbCl_3$ phase as an intermediate state during $MAPbI_{3-x}Cl_x$ formation, suggesting that MACl may serve as a temporary intermediate agent and leave the film during thermal annealing. Device performances have clearly confirmed the positive effects attributed to MACl addition. However, residual impurities within the film have been observed by XRD, such as PbI_2 precursor complexes and $MAPbCl_3$ phases [180]. Detailed studies regarding non-stoichiometric ratios of precursors as well as the role of impurities and Cl inclusion still remain under investigation.

A non-stoichiometric solution of PbI_2 and MAI is essential to modify film formation of planar $MAPbI_3$ structures. The best device performance achieved of approximately 12.2% was demonstrated by using a precursor solution molar ratio of ~0.6—0.7:1 PbI_2 to MAI in DMF [116]. The authors believed that residual amounts of PbI_2 and MAI are left within the final film because of their different affinities toward the substrate and that non-stoichiometric precursor solutions are vital for achieving pure $MAPbI_3$ film formation. A higher PbI_2 to MAI ratio (>0.8:1) in the precursor leads to the formation of microfibers within the film, which significantly increases film roughness (Fig. 3.6). In addition, excess $MAPbI_3$ resulting from lower PbI_2 to MAI ratios (<0.6:1) does not exhibit the typical photoluminescence peaks and absorption edges observed. It is also believed that introducing Cl could form an intermediate complex to reduce the interface energy and enhance the film formation in one step solution process [69,70,72]. Recently, it is reported that coordination degree and mode in initial colloidal solution was able to be tuned by additional methylammonium halide over the stoichiometric ratio. It is found that excess organic component can reduce the colloidal size of and tune the morphology of coordination framework in relation to final perovskite grains, and partial-chlorine-substitution can accelerate the crystalline nucleation process of perovskite. Devices have been reported to achieve 17% PCE without distinct *J*—*V* hysteresis. This work represents the importance of colloidal engineering correlating to the important fundamental chemistry of perovskite precursors. Further study on this topic will

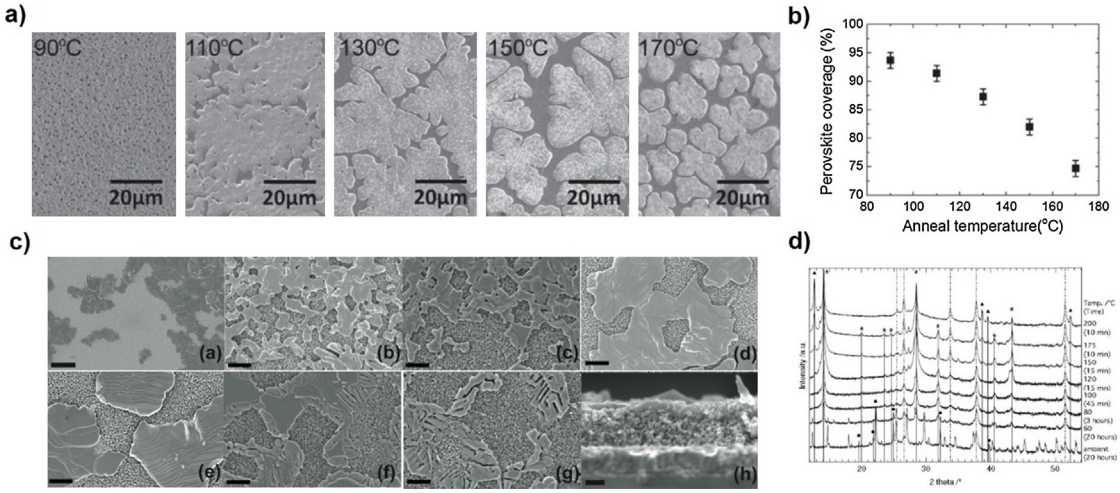

Figure 3.7 One-step solution processed $MAPbI_{3-x}Cl_x$ perovskite films annealed at different temperatures: (a) SEM images and (b) the percentage of surface coverage; (c) SEM and (d) XRD spectra of $MAPbI_{3-x}Cl_x$ perovskite films on mesoporous TiO_2 obtained for different annealing temperatures and times. Copyright 2013 Wiley.
Source: Adapted with permission from Refs. [66,181].

provide genuine guideline to produce high quality perovskite films [296].

Thermal treatment

Thermal annealing is an essential step to initiate or accelerate the reaction between the organic and inorganic species. Eperon et al. investigated the properties of planar mixed halide perovskite $MAPbI_{3-x}Cl_x$ films based on one-step solution techniques for different annealing temperatures (Fig. 3.7a) [181]. The perovskite films with different film thicknesses deposited onto compact TiO_2 ETL layers were annealed at different temperatures ranging from 90 °C to 170 °C. The authors observed that higher annealing temperatures resulted in lower surface coverage of the film. In addition, both the increased initial film thicknesses of the perovskite and compact TiO_2 layers could improve the surface coverage of the final perovskite film. Resulting device performances demonstrated that a higher J_{sc} can be achieved from films with higher coverage due to its increased light absorption capability. Dualeh et al. reported that densely interconnected perovskite films can be obtained by annealing at 80 °C for 3 h, or 100 °C for 45 min, respectively, based on a mesoporous $MAPbI_{3-x}Cl_x$ structure [66]. At lower temperatures (<80 °C), perovskite phase formation appeared to be hindered. Further prolonging the annealing time at low temperatures does not provide any advantage for film quality. Perovskite films annealed at higher temperatures (>100 °C) will produce secondary phases of PbI_2, likely originating from the decomposition of $MAPbI_3$. Fast annealing treatment has been reported by Saliba et al. for higher temperatures and shorter times to enhance device performances for planar structure devices. It was speculated through PL measurements that this effect can reduce recombination losses at grain boundaries [182].

Similarly, thermal annealing processes affect resulting film morphology not only for one-step methods, but also for hybrid and sequential deposition methods. For example, in using the VASP technique, MAI vapor is generated under 150 °C, with an excessive amount of MAI powder necessary to maintain sufficient MAI vapor pressure within the reaction chamber. Using excessively high or low processing temperatures will cause an undesired film quality as result of slow reaction rates or additional side/decomposition reactions [21]. In this scenario, the annealing temperature has only a minor effect regarding surface coverage of the resultant films because the presence of the pre-formed conformal PbI_2 framework serves as a reactant reservoir.

Recently, perovskite films with millimeter scale grains have been achieved [297]. A hot diluted solution of PbI_2 and MACl (70 °C) with molar ratio of 1:1 was applied to the hot FTO substrate (180 °C), and was immediately subjected to spin-coating. Due to non-stoichiometry of the precursors, the final films exhibit an apparent $MAPbCl_3$ phase. Interestingly, 18% PCE has been observed in the devices based on these films. And in these devices, V_{oc} versus log-scaled light intensity [ln(I)] obeys a slope of ~1.0 kBT/q (where kB is the Boltzmann constant, T is absolute temperature, and q is elementary charge), which suggests that a bimolecular recombination process dominates during device operation, similar to that observed in high quality semiconductors such as silicon and GaAs. These findings have brought a lot of valuable information to the research community, including (1) the film passivation and defects states, (2) grain growth vs. nucleation at different temperature, (3) carrier behavior in the polycrystalline films, and (4) possibility in film fabrication techniques.

Additives

The inclusion of small amounts of chemical additives in perovskite precursor solutions have been reported to provide advantages in terms of crystallinity, film coverage, and resulting device performance. Adopted from organic photovoltaic research efforts, Liang et al. added 1% of 1,8-diiodooctane (DIO) into a perovskite precursor solution to demonstrate an increase in device performance [135]. The films exhibited improved surface coverage and crystallinity

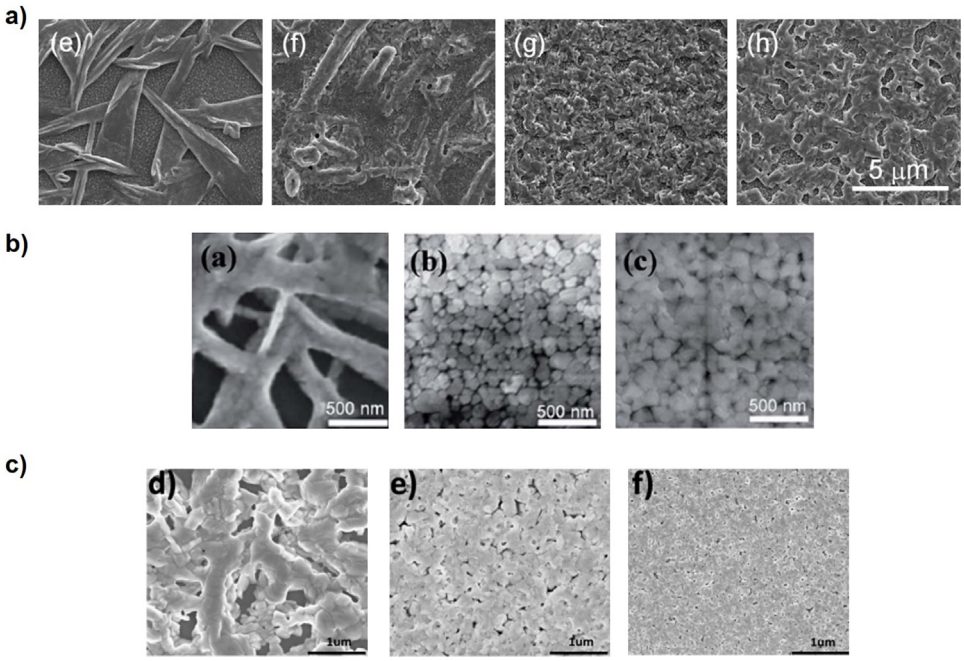

Figure 3.8 (a) SEM images of perovskite films for various amount of MACl treatment. The amount of MACl inclusion increases from left to right; (b) Perovskite films for different amounts of NH_4Cl treatment. The amount of NH_4Cl increases from left to right; (c) SEM images of perovskite films without treatment. Solvents washed with toluene and small molecular additive assisted nucleation, from left to right. Copyright 2014 Wiley, 2014 American Chemical Society, 2014 The Royal Society of Chemistry.
Source: Adapted with permission from Refs. [135,183,184].

as observed through SEM (Fig. 3.8a) and XRD. They speculated that the temporary coplanar chelation of Pb^{2+} with DIO, as I^- ligands reside in axial octahedral positions on Pb^{2+}, enhances the solubility of $PbCl_2$ in DMF. The chelation efficiency could be further modulated to control the film growth. Interestingly, Zuo et al. reported a high fill factor perovskite solar cell based on NH_4Cl as an additive in the PbI_2-MAI precursor. Better crystallinity, well-defined morphology, and improved device performances were evident, similar to films that use DIO or MACl as additives (Fig. 3.8b). The mechanism by which the NH_4Cl additive brings about improvements is still unclear at present. However, it is believed that the NH_4Cl acts in a similar role as MACl in perovskite film growth [183].

Chen et al. recently reported that adding 3% small molecule BmPyPhB into the PbI_2:MAI (1:1) solution assists the nucleation of perovskite formation. The authors provided a novel control process of the film nucleation as well as the compensation capability of various types of organic species in perovskite materials [184]. The role of small molecules on the electrical and optical properties are still under investigation. These results suggest that the introduction of additives into the precursor film could be an effective way to control film growth and subsequently enhance the device performance.

Atmospheric effects

Generally, perovskite films are deposited and annealed in nitrogen or dry air glove boxes with H_2O contents less than 5 ppm. Perovskite films annealed in the presence of moisture were deduced to deteriorate the perovskite film. However, in recent studies, Zhou et al. found that perovskite films annealed in a mild moisture environment (~30% humidity) could in fact significantly improve film properties [8]. The growth mechanism was characterized by XRD and SEM (Fig. 3.9a), showing stronger $MAPbCl_3$ peaks from XRD for films fabricated in the presence of a humid environment (Fig. 3.9a). Time-resolved photoluminescence measurements demonstrated an improvement in carrier lifetime of the perovskite films by a factor of almost 2, as well as a dramatic improvement in the V_{oc} (from 1.02 V to 1.11 V). You et al. also studied moisture-assisted perovskite film growth on PSS:PEDOT surfaces [185]. Compared to other atmospheres, perovskite films annealed in ambient air show improved crystallinity and larger grain sizes. Thus, moisture could possibly promote the motion of organic species and accelerate grain growth by partially dissolving the reaction species and accelerating mass transport within the film, resulting in a reduced quantity of pin holes within the film. However, films annealed under high humidity conditions show obvious PbI_2 peaks as a result of decomposition of the organic species [71]. These results indicate that a controlled humidity atmosphere during film formation is necessary to achieve high performance perovskite devices. Further examination of different atmospheric effect are currently under investigation.

Furthermore, Xiao et al. have demonstrated a solvent annealing technique adopted from similar methods in optimizing the morphology of organic solar cells [186]. In this technique, a semiconductor film is placed in an environment saturated with solvent vapor during the annealing process to promote film growth. The perovskite films were annealed in the presence of DMF vapor at 100 °C for 1 h. An extensive growth was observed for the presence of solvent vapor, as

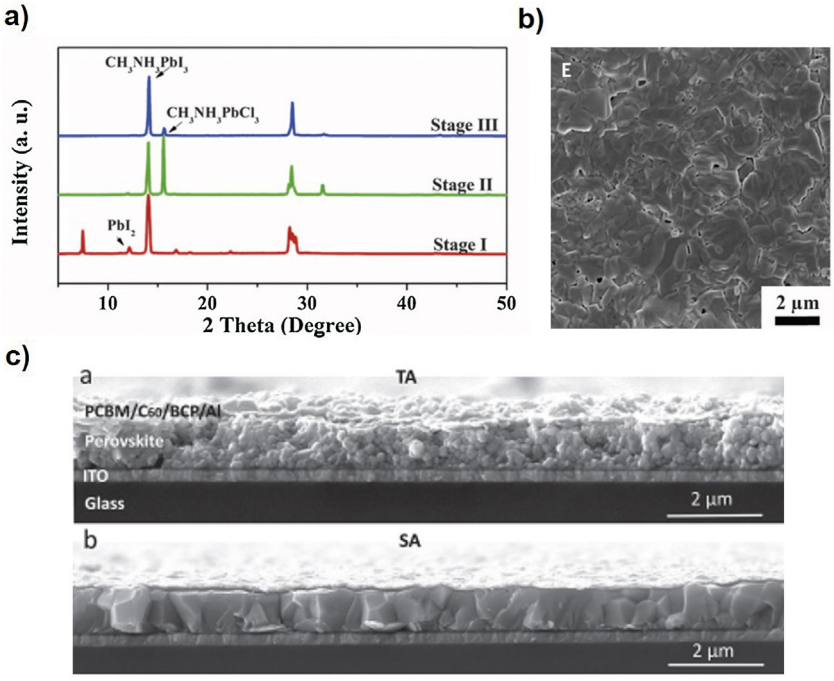

Figure 3.9 (a) XRD spectra of perovskite films annealed at 90—105 °C in a moisture-controlled environment (Stage I: 20 min, Stage II: 60 min, Stage III: 85 min); (b) SEM image of the perovskite film annealed for 85 min under mild humidity; (c) cross section SEM of thermally annealed (TA) and solvent annealed (SA) perovskite films. Copyright 2014 American Association for the Advancement of Science, 2014 Wiley.
Source: Adapted with permission from Refs. [8,186].

it helped to facilitate the interaction of PbI_2 and MAI by enhancing interdiffusion and reorganization of the precursor ions. Interestingly, it was found that the crystal size was proportional to the film thickness, i.e. thicker films could produce larger grains. However, inverted planar devices prepared via solvent-annealed $MAPbI_3$ were not affected by increasing film thickness. Thick perovskite films of approximately ~1 μm were able to yield PCEs approaching 15%, which are comparable to those of thinner films.

Solvent engineering

Solvent choice greatly affects film formation and quality of perovskites, particularly for solution-based processing. Due to the distinct nature of the organic and inorganic precursors of $MAPbI_3$, the selection of solvents with sufficient solubility for both components is limited. Currently, N,N-dimethylformamide (DMF), dimethyl sulfoxide (DMSO) and gamma-butyrolactone (GBL) are the most commonly used solvents. There are several parameters that closely related to the film growth of the perovskite, including solubility, boiling point, viscosity, vapor pressure and interaction between solutes and solvents. All these parameters should be taken into considerations in order to control the film quality by manipulating the crystal growth kinetics. In the early reports, perovskite precursors were deposited using GBL as the solvent on a mesoporous TiO_2 scaffold, resulting in the effective pore-filling of perovskite into the mesoporous TiO_2 [91]. Through tuning the precursor concentration in GBL, it was shown that an overlayer can be formed on top of the mesoporous structure to reduce the direct contact of the ETL and HTL and enhance light absorption [84]. Snaith and co-workers first used DMF-based perovskite precursors to deposit onto mesoporous Al_2O_3 scaffolds. Later, this was adopted to fabricate planar perovskite solar cells [19]. DMF exhibits a relatively low boiling point (154 °C) compared to that of GBL (204 °C), which aids in facilitating film formation. However, owed to extremely high growth rate of $MAPbI_3$, thin films with pinholes and moderate surface coverage are usually observed for one-step PbI_2—MAI—DMF solution processes [147]. Alternative strategies utilizing organic solvents and various processing techniques have allowed for optically dense perovskite films that have resulted in increased device performances.

Solvent-wash induced crystal growth has been realized to fabricate perovskite layers in planar geometry [93,187]. After spin-coating a solution of $MAPbI_3$ in DMF, the wet film was immediately exposed to an organic solvent, such as toluene or chlorobenzene, to induce a fast crystallization process. $MAPbI_3$ precursors have lower solubility in these organic solvents and can be used to enhance precursor concentration during exposure, thus promoting fast nucleation and crystal growth. This resulted in a flat and compact polygon grain features up to microns in size after annealing. It has also been found that the morphology of the resulting film is closely related to the delay time when of the solvent treatment during spin-coating. In this study, 12 solvents were investigated, where the addition of chlorobenzene, benzene, xylene, and toluene lead to uniform films over the entire substrate. The kinetic control of nucleation by the fast solvent wash has generated a similar approach through vapor-assisted film formation [188], which enables a quick fabrication of planar devices at low temperature.

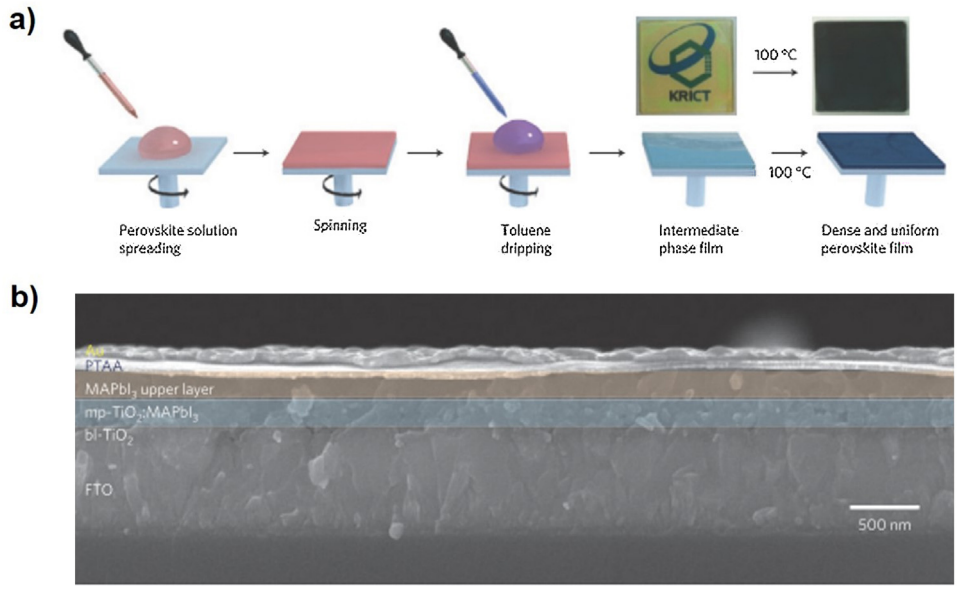

Figure 3.10 (a) Schematic illustration of perovskite films prepared from a solvent mixture of GBL/DMSO (7:3) and dripped with toluene. (b) cross section SEM of the resulting perovskite film. Copyright 2014 Nature Publishing Group.
Source: Adapted with permission from Ref. [93].

Mixed solvents have also been reported to improve the morphology of perovskite films. Kim et al. observed that use of a DMF and GBL solvent mixture (97:3% volume ratio) produces smooth perovskite films and uniform crystal domains with small grain sizes on planar inverted substrates [189]. A small amount of GBL solvent reduces the growth rate and inhibits microfiber structure formation. The combination of GBL with DMSO (7:3 volume ratio) provides another combination for fabricating high quality perovskite films. A 0.8 M $MAPbI_{3-x}Br_x$ mixed solvent solution, where $x = 0.1—0.15$, was spun onto a mesoporous TiO_2 layer followed by a toluene drip during spinning (Fig. 3.10a). Characterization results show that an intermediate MAI—PbI_2—DMSO complex may form during this process prior to annealing [93]. Toluene addition leads to the immediate freezing of precursor constituents during spinning via the quick removal of excess DMSO solvent and the rapid formation of the MAI—PbI_2—DMSO phase, leaving a uniform and transparent layer. Annealing completes the formation process, for which the film shows a compact polycrystalline texture with grain sizes up to several hundreds of nanometers. Thus we can see that solvents either from the precursor solution or introduced during processing substantially influence molecular species interactions within the system and promote various growth paths that greatly affect film quality.

To wrap up, the optimization of film formation and crystallization is of essence for further advances in perovskite solar cells, as most improvement have been witnessed due to the enhancement of the quality of the films, mainly in term of morphology and defects states. Currently, the optimization of film morphology has achieved fast progress, where the continued increase in the domain size of crystals and the uniformity of thin-film deposition is expected to realize soon. On the other hand, the passivation of the trap states will be key and the main challenge to future advances in device performances.

Interface engineering

Hole transport materials (HTM)

Inherited from the similar device architectures and operational principles of organic photovoltaics (OPV) and DSSC technologies, perovskite solar cells have benefited from a wide selection of HTMs that have been continually investigated over the 15 years of previous technological development. The broad spectrum of HTMs covers organic small molecules and oligomers, polymers, and inorganic crystals, as will be discussed sequentially. The chemical structures of some compounds are illustrated in Figs. 3.11 and 3.12.

2,2′,7,7′-Tetrakis[N,N-di(4-methoxyphenyl)amino]-9,9′-spirobifluorene (spiro-OMeTAD, Fig. 3.11) was first introduced in perovskite solar cells as hole transport material in 2012 [17], reaching a peak efficiency of 9.7%. To this day, spiro-OMeTAD remains the standard HTM in perovskite solar cells attracting enormous attention. Pristine spiro-OMeTAD is low in electric conductivity, and chemical doping is one common method to improve the carrier concentration and conductivity. The mechanism of chemical doping has been investigated intensively for DSSCs, and spiro-to-spiro$^+$ transition is mainly responsible for charge carrier transport [190,191]. Upon suitable doping, several key parameters that closely correlate to device performance have been studied carefully, such as redox potentials relating to doping levels [192,193], stability [194], and spiro-to-spiro$^+$ conversion ratios [195]. Recently, Abate et al. pointed out certain protic ionic liquid dopings involved in spiro-OMeTAD molecular interactions [195]. Dopants that have already achieved great success in DSSCs, such as lithium [196] and cobalt salts [197], have been successfully used in perovskite solar cells.

As one of the best small molecule hole transport materials, spiro-OMeTAD has shown superior properties among

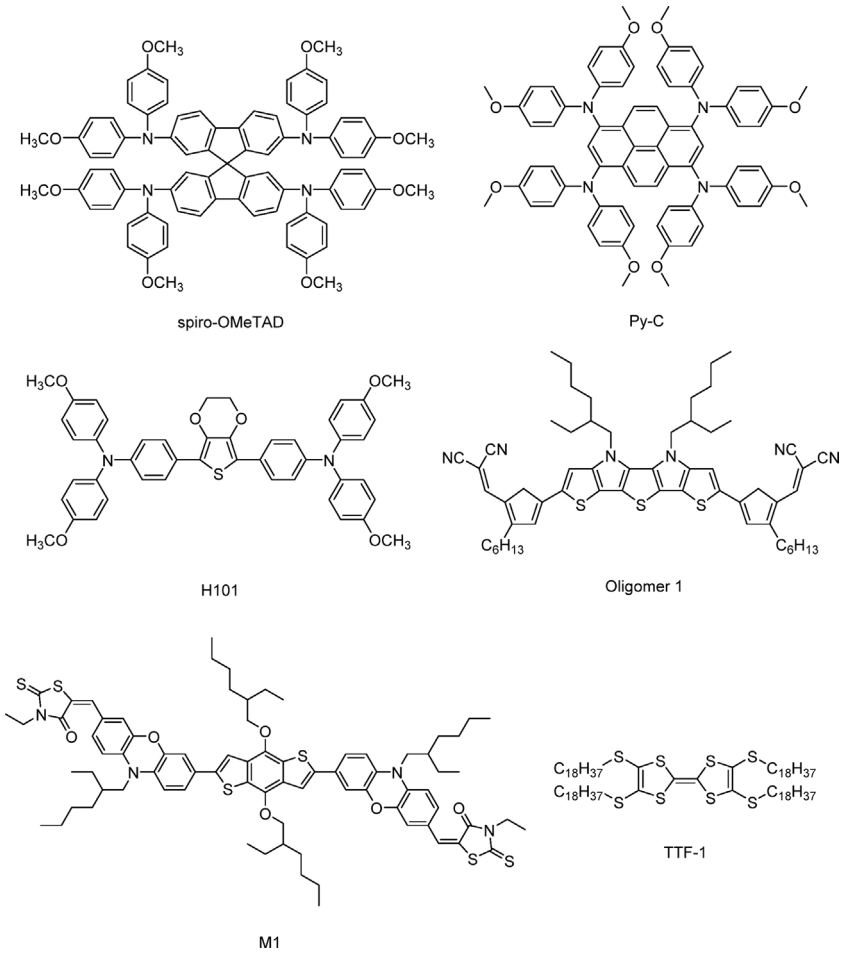

Figure 3.11 Chemical structures of reported small molecule hole transport materials.

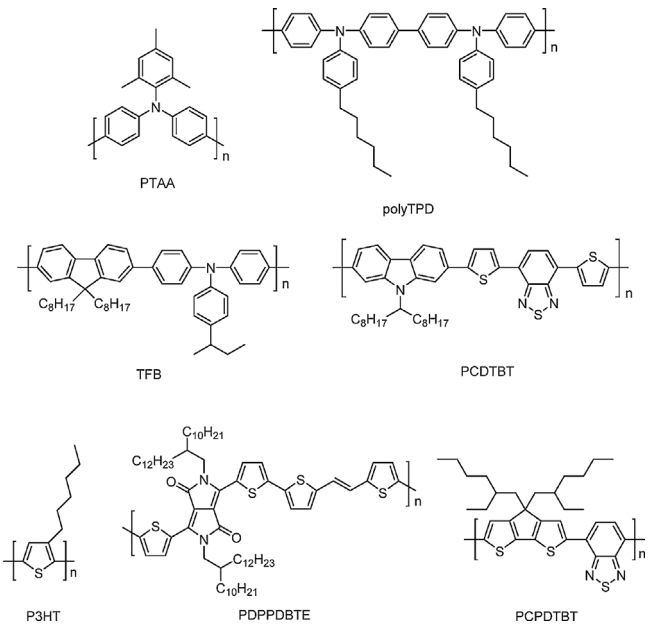

Figure 3.12 Chemical structures of reported conjugated polymer hole transport materials.

all candidates. However, its high cost and processing complexity [191,198,199] have led to the pursuit of other substitutes in the small molecule regime. Arylamine derivatives have received a great interest, showing comparative or even better performances than spiro-OMeTAD [104,162,163,174,200,201,202,203,204,205,206]. Besides, other molecular design is appearing recently [149,207–211]. Inspired by the success of OPV materials, some acceptor–donor–acceptor (A–D–A) type small molecules have been synthesized and employed as HTLs, showing high conductivities and tunable energy alignments [208,210,211]. Particularly, Cheng et al. designed a small molecule HTM M1 (Fig. 3.11) based on a benzo[1,2b:4,5b′]-dithiophene (BDT) donor and a phenoxazine (POZ) acceptor [211]. Through suitable matching of HOMO and LUMO levels with the adjacent layers, the devices showed a V_{oc} as high as 1.02 V. It was claimed the small molecule also portrayed strong absorption in the visible region and relatively high hole mobility, contributing to high J_{sc} and an overall efficiency of 13.2%. However, the strong optical absorption contributions of the HTM to the final photocurrent are still under debate [185,208]. Interestingly, Ishii et al. recently used crystalline perylene as a HTL, yielding a V_{oc} reaching 1.15 V under a 1 sun condition [212]. The high V_{oc} achieved

is attributed to (1) an appropriate HOMO level of perylene (−5.40 eV) that broadens the limit to minimize V_{oc} loss, and (2) minimized Gibbs free energy losses due to the oriented structure of perovskite and high crystallinity of the HTL. However, the cell showed a relatively low J_{sc} and FF due to the moderate conductivity of the crystalline perylene layer and resulted an efficiency of 4.15%.

Conjugated polymers have been intensively exploited as HTMs for perovskite solar cells, as shown in Fig. 3.12. Typically, PSS:PEDOT is used for inverted configurations and polythiophenes and their derivative poly(3-hexylthiophene-2,5-diyl) (P3HT) [84,136,213—228] are employed for normal structures. PSS:PEDOT is a widely used electron blocking layer due to its excellent transparency, work function, conductivity and chemical stability. Comparing to spiro-OMeTAD based perovskite solar cells, PSS:PEDOT devices often show relatively lower V_{oc}, which is potentially a result of the relatively larger difference in work function between PSS:PEDOT and perovskite [71,147]. As such, a composite of PFI/PEDOT:PSS has been investigated to obtain energy level matching between the HTL and perovskite layer [218]. By simply changing the weight ratio of the two species, a work function of 5.4 eV in the composite is achieved to minimize the V_{oc} loss. The best performing devices showed PCEs around 11.7%. In addition, polythiophenes can also substitute directly for PSS:PEDOT for the same device configuration [222]. A thin film of polythiophene prepared via electrochemical polymerization showed a very compact surface and small surface roughness, facilitating sufficient wetting of the PbI_2 solution. Furthermore, it provided a well matched energy level to perovskite and a decent conductivity leading to a PCE of 11.8%.

P3HT has received significant attention due to its excellent electrical properties, robust structure and ease of processing. Habisreutinger et al. improved the stability of the HTL by mixing P3HT with single-walled carbon nanotubes (CNT) [136]. The composite HTL showed excellent hole extraction and conductivity, which provided high J_{sc} and FF in the device with a PCE of 15.3%. It is worth noting that the blend was further embedded within a PMMA matrix to create a robust encapsulation of the solar cell. As a result, the active layer of perovskite showed pristine crystallinity after 96 h of exposure to air. In a similar work, CNTs were blended with P3HT in order to enhance conductivity [214]. The P3HT—CNT composites were dissolved in dichlorobenzene and then spin-coated onto perovskite/TiO_2 film serving as the HTL. Interestingly, it was found that the crystallinity of P3HT was increased upon the addition of CNTs, and consequently the conductivity. The cell reached a highest efficiency of 8.3%. A graphdiyne modified P3HT has been employed to fabricate devices with an observed stronger absorption and higher PCEs reaching 14.58% [226]. Raman and UPS results clearly indicate an interaction between P3HT and graphdiyne, claimed to favor hole conduction. In addition, stronger absorption due to the introduction of graphdiyne was observed.

Apart from P3HT, Heo et al. used poly-triarylamine (PTAA, Fig. 3.12) as a HTM to construct a high efficiency pillared structure with 12.0% PCE [84]. Compared with spiro-OMeTAD, PTAA showed significantly higher V_{oc} and FF, mainly due to the well matched energy levels and excellent conductivity. Polyfluorene derivatives with a TAA backbone of the main chain have been synthesized (TFB, Fig. 3.12), realizing an efficiency of 13.58% in devices based on two-step perovskite deposition [224]. A DPP based polymer, namely, poly[2,5-bis(2-decyldodecyl)pyrrolo[3,4-c]pyrrole-1,4(2H,5H)-dione-(E)-1,2-di(2,20-bithiophen-5-yl)ethene] (PDPPDBTE, Fig. 3.12) was demonstrated to achieve a 9.2% PCE, improved over spiro-OMeTAD and P3HT under the same conditions [216]. Stability tests revealed device to withstand 1000 h storage without degradation. In a parallel study, Lin and co-workers [219] tested a series of different polymer HTLs, including P3HT, PCPDTBT, DPP—DTT and PCDTBT (Fig. 3.12). It was found that deposition of perovskite onto PCDTBT presented the highest degree of crystallinity, which shed a light onto substrate control of crystallinity. With further optimization of perovskite film quality, the best performance cell showed an efficiency of 16.5%. Wu and company used graphene oxide as a HTL for an inverted structure [229]. The observed high PL quenching proved efficient hole extraction from these devices. Moreover, perovskite films deposited on graphene oxide exhibit a preferential (1 1 0) plane orientation.

Inorganic materials have also attracted research interests as HTMs in perovskite solar cells due to their high stability and low cost. Christians et al. reported an inorganic hole conductor based on CuI that showed a high J_{sc} and FF [230], as well as stable photocurrents up to 2 h under continuous illumination. However, the V_{oc} was quite low (0.55 V) due to severe recombination at the interfaces. NiO was employed as the first reported metal-oxide HTL in perovskite solar cells, demonstrating less of a V_{oc} loss than CuI [116,231—233]. Wang and collaborators used mesoscopic NiO as a HTL as it has been successfully used in OPV and DSCC devices [231]. It featured a V_{oc} of 1.04 V, J_{sc} of 13.24 mA/cm^2, FF of 0.69 and an efficiency of 9.51%. Jen et al. reported that insertion of a compact NiO layer between ITO and perovskite can lead to higher device performances over PEDOT:PSS [232]. It is claimed that improved wetting and energy alignment contributes to the better performance. CuSCN was found to have high hole mobility, good chemical stability, and solution-processability [233,234]. With efficient charge extraction and collection properties, CuSCN has been reported as a HTL achieving an overall efficiency of 12.4% [208]. Etgar et al. reported the co-sensitization of perovskite and PbS quantum dots to construct a solar cell with a panchromatic response [235]. Since the bandgap of PbS quantum dots is only ~1.4 eV, it acts as light harvester, in addition to its role of a HTM. The device showed high J_{sc} of 24.63 mA/cm^2, with V_{oc} of 0.66 V, possibly due to the low work function of the quantum dots leading to V_{oc} loss upon carrier extraction. Later different sizes of PbS colloidal quantum dots were synthesized and employed in perovskite solar cells [236]. Through this method, the band gap and electron affinity of PbS can be tuned to effectively block electron injection into the PbS layer. The PbS layer served as not only HTL for hole collection, but also as a light harvester to expand the device absorption to 1000 nm. Such devices reached an efficiency of 7.5%. In addition, HTMs can also be chosen from cost-effective materials, such as Cu-phthalocyanine [237]. With a suitable energy alignment, the cells obtained an efficiency of 5.0% in its early stage.

Electron transport materials

Electron-selective contacts play an important role in perovskite solar cells, which allow electron extraction and retard the recombination of holes at the electrodes. This section will mainly focus on material selection and processing for compact electron transport layers (ETL), as mesoporous scaffolds have been discussed in 'Device architecture' section. Similar to the HTM, ETMs have been intensively explored covering a wide spectrum of organic and inorganic materials.

The most common compact ETL is composed of TiO_2, which is deposited using a titanium precursor solution by spray pyrolysis or spin coating. It is often followed by $TiCl_4$ treatment with high temperature annealing up to 450 °C [6,17,19]. To avoid high temperature processing, sol—gel processes aided by pre-synthesized nanocrystals have been developed [8,147,238,239]. Corresponding devices employing TiO_2 compact films exhibit a lower series resistance and improved FF. In addition, atomic layer deposition (ALD) has been investigated to fabricate such compact layers [240], presenting a lower pinhole density in the resultant films comparing to those obtained from spray pyrolysis and spin coating.

ZnO has also been employed as an electron selective contact in an attempt to replace the UV-sensitive TiO_2. The compact layer has been fabricated through various approaches such as electro-deposition [106], magnetron sputtering [149], and sol—gel approaches [148]. In some cases, device performance is insensitive to the thickness of the ZnO layer, which is ascribed to the high electrical conductivity of the ZnO film [149]. Over 15% PCE was observed for devices based on the ZnO with perovskite films fabricated through two-step methods, effectively omitting a prolonged heating process [148].

[6,6]-Phenyl-C61-butyric acid methyl ester ($PC_{61}BM$) is a widely used ETM, often coupled with PSS:PEDOT to provide further enhanced electron transport, has a favorable energy band alignment with perovskite [20,71,147]. A PL quenching was observed for the addition of a PCBM ETL, realizing an efficiency over 91% that indicates organic acceptors are highly effective when interfaced with perovskite absorbers [147]. This facilitates the adoption of organic components for perovskite technologies, thus allowing the utilization of the extensive existing knowledge of hybrid interface engineering. Use of [6,6]-phenyl-C71-butyric acid methyl ester ($PC_{71}BM$) exhibited improved photovoltaic performance with higher J_{sc} and FF compared to those of $PC_{61}BM$. This was attributed to a better external quantum efficiency in photocurrent than $PC_{61}BM$ as a result of enhanced spectral responses in the visible region [241,242]. Double-layered fullerenes, with a spun cast PCBM layer underneath followed by a thermal evaporated C_{60} layer, were used as electron extraction layers [116,173]. This double fullerene layer structure not only effectively eliminates leakage currents (possibly due to better coverage on the perovskite film), but exhibits better passivation of traps. Interestingly, it was found that double fullerene-based devices provided relief to *J—V* hysteresis effects.

Interface modifications

Interface plays an extremely essential role in PV devices. It is important to control the carrier behavior across relevant interfaces to achieve high performance [8]. It is also favored to retard the interface aging to pursue long term stability of devices. Therefore increasing interest and rapid progress has been received recently, (1) to manipulate the carrier dynamics at the interfaces [103,243—248]; and (2) to improve the device stability by the rationale design.

Abate et al. [243] have reported use of iodopentafluorobenzene (IPFB) at perovskite/HTM interfaces to passivate perovskite crystals for an achieved 20% PCE. IPFB is a Lewis acid that bonds with surface halogen atoms through donor—acceptor complexes, consuming excess negative charges hence allowing further extraction of holes. Similarly, Noel and co-workers inserted the Lewis bases thiophene and pyridine at the interface [244] for an observed reduced nonradiative recombination of holes.

Deep mid-gap states present at TiO_2 surfaces has generally provided non-radiative recombination channels at the perovskite interface that hampers the device performance

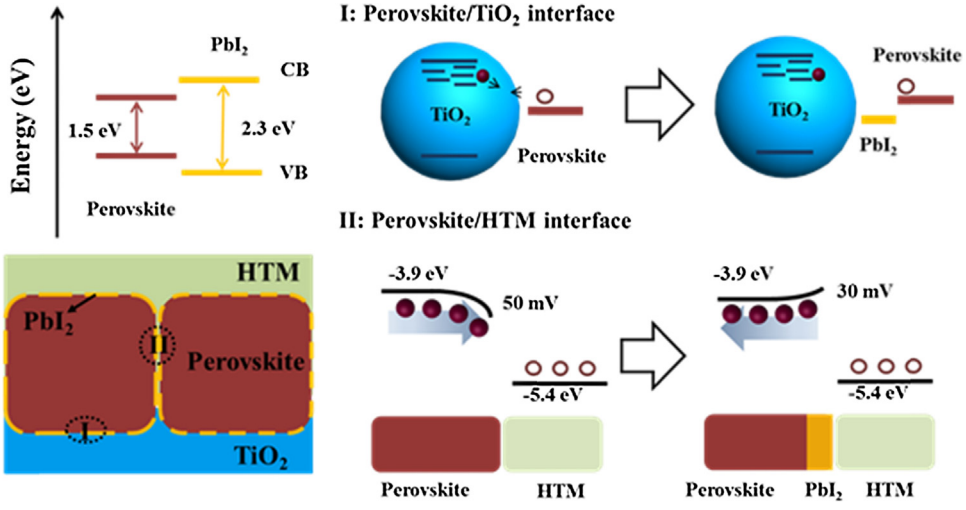

Figure 3.13 Proposed mechanism for PbI_2 passivation in $MAPbI_3$ film.
Source: Adapted with permission from Ref. [160].

[105]. Various attempts have been made to passivate the TiO_2 surface. For instance, a series organic compound HOOC—R—$NH_3^+I^-$ has been reported to passivate surface traps of TiO_2 [247]. Furthermore, the additive was confirmed to aid growth of perovskite on mesoporous scaffolds with higher loading and better crystallinity. Yttrium substitution [8,104,247] has also shown to qwell defects at the surface of TiO_2, enabling electrons in TiO_2 to recombine with holes from the perovskite or HTL film at a slower rate. However, it remains unclear whether yttrium elements are physically incorporated into the TiO_2 nanocrystal. Carbon-based materials have proven good passivation effects on TiO_2. C_{60}-SAM has been reported to modify both mesoporous and compact TiO_2 structures to provide the anchoring group to attach the C_{60} and TiO_2. The fullerene moiety has proven to successfully reduce non-radiative charge recombination [248,249]. In addition, *J—V* hysteresis has been effectively alleviated by introducing C_{60}-SAM. Zhu et al. inserted graphene quantum dots between TiO_2 and perovskite layer, greatly decreasing the electron extraction time from the perovskite layer [224]. With the presence of graphene quantum dots, injection lifetime can be as small as 90 ps with an efficiency increase to 15%. In addition, perovskite solar cells utilizing graphene oxide at the interface between HTL and perovskite have been reported to enhance the interface contact and charge collection efficiency resulting in improved J_{sc} [250].

Interestingly, PbI_2 has been reported to passivate defects at the perovskite interface across the entire device [160]. Simply by releasing the organic species during annealing, a PbI_2 phase was observed to be present at perovskite grain boundaries and interfaces [161]. It has been proposed that the PbI_2 serve to passivate the TiO_2 surface traps and facilitate hole extraction at the perovskite/HTL interfaces, according to series measurements, as shown in Fig. 3.13. Device performances exhibited systematical changes in response to the amount of PbI_2 introduced, and femtosecond time-resolved transient absorption spectroscopy further confirmed the PbI_2 passivation effect by monitoring the electron dynamics across the TiO_2/perovskite interface [162].

As a result of the significant effects seen between interfaces of the perovskite films and transport layers, interface engineering across electrodes has also attracted sufficient interest. PEIE, a polymer that contains simple aliphatic amine groups, has been employed to reduce the work function of ITO. It eliminated the possible Schottky barrier at the TiO_2/electrode interface, and improved the device performance in terms of FF [8]. Sun et al. used a zwitterionic small molecule and LiF to modify the electron transport at the cathode [251]. Addition of rhodamine 101 can significantly decrease surface roughness of a PCBM ETL, leading to better contact with the Ag electrode. Adding LiF beneath Ag electrode can increase V_{oc} by approximately 0.1 V. Using both rhodamine 101 and LiF allowed the cell to reach a peak efficiency of 13.2%. In addition, Cs_2CO_3 has been demonstrated to modify the ITO surface to achieve optimized interfacial energy level alignments, resulting in efficient electron-selective contacts. Results indicated that the surface work function of ITO was 0.4 eV closer to vacuum level after Cs_2CO_3 treatment. The device achieved a remarkable PCE of over 15% [252]. In addition, poly[(9,9-bis(3′-(N,N-dimethylamino)propyl)-2,7-fluorene)-alt-2,7-(9,9-ioctylfluorene)] (PFN) [185] and bathocuproine (BCP) [173] have been employed to modify the cathode for better electron collection, which have been a common treatment used in OPV technology.

Interface engineering addresses device stability issues, which have been widely reported [189,245,253,254]. A Sb_2S_3 layer has been introduced to modify the interface between TiO_2 and perovskite, which largely improves the device stability against light illumination [253]. It was argued that light degradation occurs at the interface between TiO_2 and perovskite. Comparing to the standard conditions, perovskite films in contact with Sb_2S_3 experience less degradation to form PbI_2, as confirmed by XRD. A speculated transformation mechanism illustrated that the lower electron affinity of Sb_2S_3 were able to block electron injection into TiO_2 that leads to oxidation of iodine. In addition, insertion of ultrathin Al_2O_3 layer can protect perovskite decomposition [254]. Computational results showed that due as a result of hydrogen bonding between $CH_3NH_3^+$ and H_2O^+, $CH_3NH_3^+$ loss can occur in a humid environment thus changing the crystal structure of $CH_3NH_3PbI_3$. A layer of ALD-Al_2O_3 coated onto the HTL resulted in a preserved cell efficiency of 12.9% after exposure in open air for 24 days. However, the insulating nature of the Al_2O_3 layer appeared to result in a decrease of J_{sc}. Furthermore, efforts have been conducted to improve interfacial contact between perovskite and HTM. As an example, montmorillonite (MMT) was used to form a buffer layer on top of the hole transport layer, which effectively prevented the corrosion of perovskite from tert-butyl pyridine (a common additive for spiro-OMeTAD). These results were confirmed by XRD and UV—vis spectroscopy measurements.

To wrap up, it still requires efforts to fully understand the interfacial atomic and electronic structures in perovskite solar cells. The strong interfacial electric field of about 10^6 V/m helps to extract photo-induced free carriers, and shallow defects states in the perovskite is essential to slow charge recombination at the interfaces. We have already observed the effectiveness of interface engineering to promote charge transport and to suppress recombination, which contribute to the entire device performance. In addition, device stability is proposed to be affected by the interface degradation. It is the key to obtain appropriate materials with suitable device architecture for further advances in high-performance and stable perovskite solar cells. Within this expect, the fundamental interfacial atomic and electronic structures have to be fully understood, such as interfacial interactions, crystal termination, and the lattice match.

Tandem devices

Based on the design of single-junction solar cell, the maximum achievable efficiency is inherently limited to 31% due to thermalization and transmission losses according to the Shockley—Queisser limit [255]. Solar cell devices employing traditional absorbers such as silicon are approaching their theoretical efficiency limit of approximately 25%. In order to further improve device PCE, a tandem design that consists of multiple absorber cells stacked in a horizontal fashion can be realized to absorb a larger portion of the solar spectrum and consequentially yield higher PCEs.

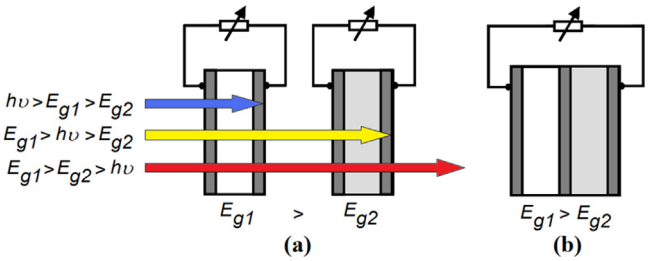

Figure 3.14 Design of a double-junction tandem solar cell with: (a) 4-terminal design in which cells are electrically insulated from one another and connected via external wiring; (b) 2-terminal design in which cells are electrically interconnected by a tunneling junction [256].

For the simplest tandem structure, two cells are stacked on top of one another and connected in series. Depending on the method of electrical interconnection between the two cells, tandem structures can be categorized as 4-terminal (stacked) or 2-terminal (monolithic) (Fig. 3.14).

When the light enters the tandem structure, the top cell with the higher bandgap (E_{g1}) absorbs and converts the high energy photons ($h\nu > E_{g1}$), leaving the lower energy photons ($E_{g1} > h\nu > E_{g2}$) to be harvested by the lower bandgap bottom cell (E_{g2}). The remaining photons are not absorbed by either cells due to insufficient energy ($E_{g1} > E_{g2} > h\nu$) to overcome the bandgap energy barrier. Since multiple absorbers are used, a tandem structure can efficiently convert photons to electrical energy from a wider range of the solar spectrum. According to Fig. 3.15, the expected theoretical efficiency for a double-junction tandem solar cell is approximately 42%.

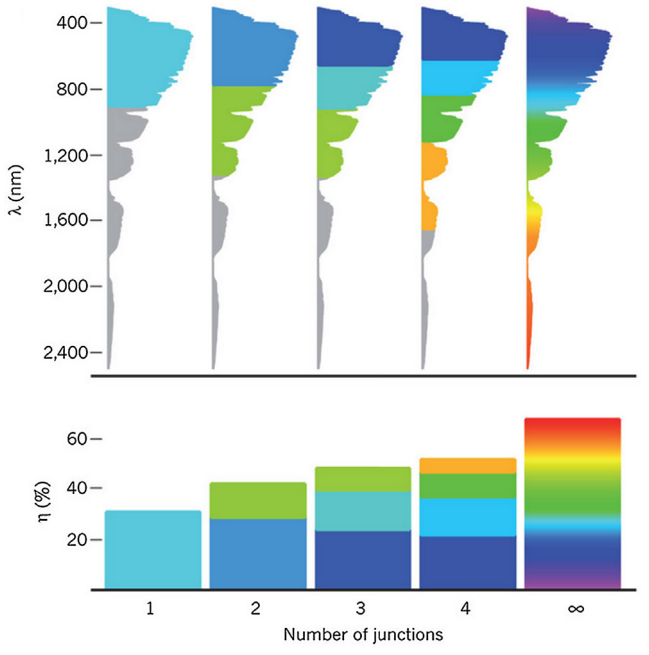

Figure 3.15 Absorption of various wavelengths of light across the solar spectrum (top) and resulting conversion efficiencies (bottom) for an increasing number of junctions (n) in solar cell [257].

Table 3.1 Band gaps of common PV absorber materials.

Material	Symbol	Bandgap (eV)
Crystalline silicon	Si	1.11
Cadmium selenide	CdSe	1.73
Cadmium telluride	CdTe	1.49
CIGS	$CuIn_xGa_{(1-x)}Se_2$	1.0—1.7
CZTS	Cu_2ZnSnS_4	1.4
Gallium indium phosphide	GaInP	1.80
Gallium arsenide	GaAs	1.43
Germanium	Ge	0.67
Perovskite	$MAPbX_3$	1.5—2.0
Perovskite	$FAPbI_3$	1.48

Perovskite materials possess both low materials cost, ease of fabrication, and extraordinary optical/electric properties, offer one of the most promising solution to realize both low-cost and high performance photovoltaics. Perovskite materials (ABX3), possessing a low bandgap-voltage offset ($Woc \equiv (E_g/q) - V_{oc}$) and high carrier mobility, are highly efficient absorbers for solar energy conversion. The state of art of perovskite solar cell has reached high power conversion efficiency in the range of 15—20%, based on only 2—3 years intensive research efforts. With further improvement in composition and interface engineering, the efficiency of perovskite solar cells has the potential to be improved to ~25%. It is even appealing that the most efficient perovskite solar cell can be fabricated under low temperature solution process, and the absorption edge is less than 800 nm in spectrum, which provides both fabrication and optical compatibility with the existing Si, or related thin film solar cell technology, to construct tandem solar cells. In this regard, the construction of perovskite based tandem device is crucial for the advanced photovoltaics development. Below, we provide band gaps of common solar absorber materials as candidates for tandem structures (Table 3.1).

$MAPbX_3$ (X = I, Cl, Br) based perovskite materials (E_g = 1.5—2.0 eV) can be generally regarded as wide-bandgap absorbers, indicating they are strong potential candidates for top-cell absorbers in tandem structures. To obtain optimal performances in double-junction tandem devices, the bottom-cell absorber chosen together with the perovskite top cell must possess a low bandgap near 1.1 eV. From Table 3.1, we can see that suitable candidates with bandgaps near 1.1 eV are crystalline silicon and CIGS.

The design of perovskite based tandem devices have been proposed in numerous reports recently, however, limited successes have been achieved so far. There are two examples of construction of perovskite based monolithic tandem solar cells, but the tunneling junction suffers considerable electric loss, with the resulting efficiency less than 15%. This efficiency is still far below the state of art efficiency for single junction perovskite solar cell. To realize a highly efficient tandem solar cell, the minimized both optical and electrical loss are the concomitant two parameters. To minimize the electrical loss, the tunneling junction between top cell and bottom cell is built up to effectively recombine the respective electrons and holes, and electrically

conductive as well. The design of tunneling junction has been proposed in this section. On the other hand, the most prominent challenge for perovskite based tandem devices is the exploration of the transparent electrodes for an efficient carrier collection. Sputtered metal oxides, e.g. ITO or AZO are successful transparent top electrodes for various solar cell technology, such as CIGS, CdTe, and Si cells. However, it is hard to extend to perovskite solar cell, as the high power energy during the sputtering process will deteriorate the organic transport materials, and even the hybrid absorber layer. An alternative transparent top electrode is solution processed carbon based materials, or metal nanomeshes, whereas the chemical incompatibility between the polar solvents or Ag species with perovskite materials hamper the further demonstration. Successful demonstrations on top transparent electrodes will be discussed in the later part.

During the past year, there have been several demonstrations of perovskite-based tandem solar cells. Löper et al. first demonstrated 4-terminal tandem devices utilizing a perovskite absorber top cell and c-silicon bottom cell. Compared with single junction perovskite solar cells (11.6%), the tandem structure enhanced the PCE to 13.4% [258]. Similar results were provided by McGehee and co-workers for a 4-terminal silicon/perovskite tandem structure achieving 17%. The most optimal combination (CIGS/perovskite) may further push tandem efficiencies to 18.6%, which is much higher than the reference perovskite single-junction cell at 12.7% [259]. In anohter study, an optical splitter has been incorporated with multi-junction solar cells to construct the four-terminal device system. The optical splitter is a multi-layered beam splitter with very high reflection in the shorter-wave-length range and very high transmission in the longer-wave-length range. By splitting the incident solar spectrum and distributing it to each solar cell, a conversion efficiency of 28% using perovskite and HJ solar cells [298]. However, the entire tandem device system depends on the high cost optical splitter, which increases the system complexity, and retards its further practical application.

Two-terminal tandem structures have also been demonstrated, showing superior vertical integration of the cells compared to 4-terminal devices, which bypasses the need for external wiring as shown in Fig. 3.16. However, two-terminal tandem structures require an extra tunneling junction/recombination layer (interconnecting layer) between cells, as depicted in Fig. 3.16, which presents additional complexity in design. Such interconnections typically require multi-layer designs of highly n- and p-doped layers to facilitate carrier tunneling and recombination. Poorly interconnected layers will result in unavoidable transmission and electrical loss. Thus, two-terminal tandem devices are often expected to produce inferior performances compared to those of four-terminal architectures.

Guha et al. demonstrated a two-terminal tandem using perovskite and CZTS as top and bottom cells, respectively [260], resulting in a PCE (4.6%) that was lower than the reference single-junction perovskite cell (12.3%). This poor efficiency was a result of the semi-transparency of the top electrode, blocking out the majority of light. On the other hand, Yang and company have successfully demonstrated two-terminal tandem design [184] using a bottom

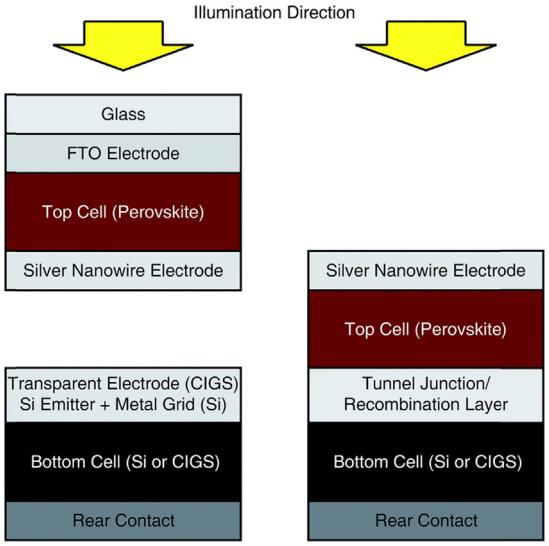

Figure 3.16 Comparison of four- (left) and two-terminal (right) tandem devices. Two-terminal tandem devices employ a tunnel junction/recombination layer (interconnecting layer) to join together the separate cells into one [259].

ITO glass electrode to allow for higher transmittance (transparency > 95%). Their results showed promising improvement in efficiency leading to 10.23%, greater than those of single-junction perovskite and polymer based devices. This is by far the best demonstration of two-terminal tandem structure employing a perovskite top cell. Recently, it has been demonstrated a 1-cm^2 2-terminal monolithic perovskite/silicon multijunction solar cell with a V_{oc} as high as 1.65 V [299]. The best power conversion efficiency is stable at 13.7%, which is low compared to the record efficiency for perovskite or Si cells. Further improvements can be achieved by replacing the spiro-OMeTAD layer with wider band gap hole transport material, improving the quality of the perovskite absorber, use of dedicated furnaces for the Si sub-cell fabrication, and by implementing better surface passivation schemes on the front and back side of the Si sub-cell.

Future designs of perovskite-based tandem structures will likely utilize the two-terminal designs as they ultimately allow for a more compact and robust structure. The success of two-terminal tandem structures can allow major current solar technologies (e.g. silicon, CIGS, II—V) to achieve higher performances by simply stacking a perovskite absorber on top of the existing device. Aside from requiring adequate transmittance and electrical conductivity, the interconnecting layer must also be compatible with existing manufacturing processes. Thus, material selection for tunnel junctions are limited. Here, we provide some potential tunnel junction designs that have proven feasible in organic and quantum-dot two-terminal tandem solar cells (Table 3.2).

Furthermore, to construct a perovskite tandem solar cell it is critical to develop a durable electrode with superior transparency. The transparent electrode has been intensively studied for various electronic devices. However, it is difficult to process on top of perovskite materials due to its fragile hygroscopic nature. Thus far, transparent top electrodes have been successfully applied in perovskite solar

Table 3.2 Potential tunnel junction/interconnecting layers for tandem perovskite structures.

Tunnel junction	Refs.
ITO/MoO_3	[261]
ITO/PEDOT:PSS	[260]
ZnO/Au/PEDOT:PSS	[262]
TiO_2/PEDOT:PSS	[263]
PEDOT:PSS/ZnO	[264]
Au	[265]
$MoO_3/ITO/AZO/TiO_2$	[266]
MoO_3/Al/ZnO	[267]

cells via limited approaches. A thermally evaporated thin gold layer (~10 nm) has been reported, achieving a device with a PCE of 7.5% [268]. In another report, a transparent conducting adhesive was utilized to laminate a Ni-mesh embedded PET film onto the perovskite solar cell, realizing a PCE over 15% [269]. Silver nanowires (AgNWs) have also been utilized as transparent electrodes for tandem perovskite devices [259]. In a recent report, AgNWs were blended with ZnO nanocrystals and applied via spray-coating. Devices based on the all-solution process achieved a PCE of 8.49%, and AgNWs were reported not to damage the underlying perovskite [270]. Recently, a transparent MoO_3/ITO electrode has been documented to obtain an efficiency of 6.2% for single-junction perovskite devices. This cell has been further incorporated into a tandem device consisting of a c-Si cell in a 4-terminal configuration, achieving a final PCE of 13.4% [258]. Thus we can see that perovskite-incorporated tandem structures provide a promising route in obtaining higher efficiency solar devices for practical use.

It is predicted that the realization of transparent electrode, high quality perovskite film, good tunneling junction and superior silicon bottom cell can ultimately yield a 29.0% efficient tandem, with the ultimate efficiency potential of these monolithic tandems surpassing 35%.

Stability

In light of the exceptional properties and consequent high PCEs observed in hybrid perovskite devices, prospects of long-term use are hindered by its unstable nature and rapid degradation in ambient environments that drastically reduce performances in relatively short periods of exposure time. Reliability issues are thus a major concern for industrial scale implementation.

The stability of these materials strongly hinges on the quality of its constituents. Pb-based perovskite materials are highly sensitive to a humid atmosphere due to their ionic nature. Sn-based hybrid perovskites are highly sensitive to both air and moisture, partially decomposing after only 2 h and reaching complete decomposition after just 1 day [55,61]. Considering the organic cation, the general trend is that MA is much more stable than FA due to the individual stability of the organic cation alone. However, $FAPbX_3$ devices have shown superior thermal stability in air and comparable sensitivity to moisture than those MA-based [39]. Controversially, Sn-based devices incorporating FA have shown poor stability in comparison to those MA-based, potentially a reflection of the relative stability of each A cation as FA has an inclination to form ammonia (NH_3), sym-triazine ($C_3H_3N_3$) and SnI_6 [36,46]. Thus, there seems to be some discrepancy in regards to the correlation between FA and stability. While Sn possesses more optimal electronic properties (i.e. band gap) than its Pb-counterpart, its performances have been hampered by its extreme sensitivity to an oxidative environment as it rapidly converts from Sn^{2+} to Sn^{4+} upon exposure. It has been shown that the addition of lead content in mixed $MASn_xPb_{1-x}I_3$ can help to prevent such oxidation of Sn^{2+} to Sn^{4+}, improving its stability in air [59]. In addition, the stability of the perovskite structure decreases upon proceeding up the halide group (group VIIA) on the periodic table from I^- to F^- [33,75]. So we can see that there are several factors to consider pertaining to each perovskite component in addressing not only PCE but stability as well.

In exploring the numerous potential degradation pathways, it is important to keep in mind the basic fundamental chemical reaction for hybrid perovskites, as follows:

$$PbI_2\,(s) + CH_3NH_3I\,(aq) \leftrightarrow CH_3NH_3PbI_3\,(s) \quad (1)$$

As this reaction is reversible, in one direction there is perovskite formation, while the other entails decomposition. In general, there are five major contributors to perovskite degradation, that include humidity, oxygen, UV light, solution (solvent, solute), and temperature, and have been thoroughly reviewed in Ref. [32]. Here we summarize some of the key points in understanding this topic.

Humidity

$MAPbI_3$ tends to hydrolyze in the presence of water, due to the inherent hygroscopic nature of the MA cation. The degradation occurs according to the following reaction mechanism:

$$CH_3NH_3PbI_3\,(s) \leftrightarrow PbI_2\,(s) + CH_3NH_3I\,(aq) \quad (2a)$$

$$CH_3NH_3I\,(aq) \leftrightarrow CH_3NH_2\,(aq) + HI\,(aq) \quad (2b)$$

$$4HI\,(aq) + O_2\,(g) \leftrightarrow 2I_2\,(s) + 2H_2O\,(l) \quad (2c)$$

$$2HI\,(aq) \leftrightarrow H_2\,(g) + I_2\,(s) \quad (2d)$$

The first step shows that upon contact with moisture the highly hygroscopic MA ion is removed from the perovskite crystal and combines with iodine to reform aqueous MAI and solid PbI_2 salt. Next, the MAI may decompose into aqueous methylamine and hydriodic acid within the film (2b), followed by degradation of HI by either a redox reaction producing H_2O and I_2 via contact with oxygen (2c), or a photochemical reaction induced by UV radiation in which HI forms iodine and gaseous hydrogen (2d). Hybrid perovskite decomposition has been reported at humidity levels as low as 55%, realized by the significant change in film color from dark black to yellow [22]. Interestingly, improvement of film quality by utilizing the sensitive nature of perovskites to moisture has been demonstrated, where the hygroscopic organic species is dissolved by the moisture thus accelerating mass transport during film growth [71,185]. The possible transformation pathways have been further investigated [180], as depicted in Fig. 3.17: $PbCl_2$ and MAI may react to form PbI_2 and MACl, co-existing with MAI (1). During

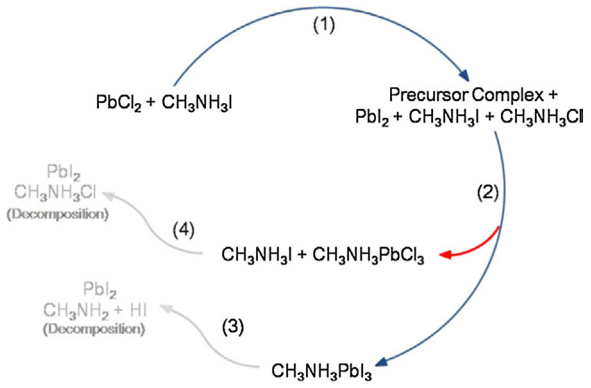

Figure 3.17 Potential reaction pathways for perovskite film formation in the presence of moisture.

annealing, PbI_2 may react with MAI, and $PbCl_2$ with MACl to form $MAPbI_3$ and $MAPbCl_3$, respectively. The $MAPbI_3$ formed at (2) may undergo thermal decomposition to produce PbI_2 and HI (3), and/or the excess MAI may continue to react with $PbCl_2$ to produce PbI_2 and facilitate the decomposition of $MAPbCl_3$ (4).

UV irradiation

TiO_2 is known as an effective photocatalyst to create hydroxyl radicals via oxidation of water and for oxidizing organic materials [32]. Consequentially, degradation of perovskite films under exposure to light for prolonged periods of time results in a similar manner to that seen in dye-sensitized solar cells, for which TiO_2 induces degradation of the iodide electrolyte by removal of its electrons. In an effort to explain these effects, Ito et al. proposed the following degradation mechanism [253]:

$$2I^- \leftrightarrow I_2 + 2e^- \tag{3a}$$

$$3CH_3NH_3^+ \leftrightarrow 3CH_3NH_2 \uparrow + 3H^+ \tag{3b}$$

$$I^- + I_2 + 3H^+ + 2e^- \leftrightarrow 3HI \uparrow \tag{3c}$$

First, the TiO_2 extracts electrons at the TiO_2—perovskite interface (3a). Subsequently both continuous consumption of H^+ to form HI and evaporation of CH_3NH_2 drives reaction (3b) forward despite the high pK_a value (10.80) of water uptake by CH_3NH_2 representing an equilibrium shift to the left in the reaction $CH_3NH_3^+ + H_2O \leftrightarrow CH_3NH_2 \uparrow + H_3O^+$. The extracted electrons at the TiO_2-perovskite interface may then reduce I_2 forming the volatile HI (3c) [32,253].

Niu and company outlined four possible routes for degradation via UV exposure, as presented below [271]. (4a) and (4b) are repeated steps (2a) and (2b) for visual convenience, showing the reformation of initial precursor components and dissociation of methylammonium into methylamine and hydriodic acid. HI can then either oxidize to form solidified I_2 (4c), or upon irradiation incur a photochemical reaction to form H_2 and I_2 (4d). The largely negative Gibbs free energy (ΔG) associated with step (4c) indicates via Le Chatlier's principle that a reaction from reactants to products is highly favorable, highlighting the significance of step (4c) in the degradation process.

$$CH_3NH_3PbI_3\,(s) \leftrightarrow PbI_2\,(s) + CH_3NH_3I\,(aq) \tag{4a}$$

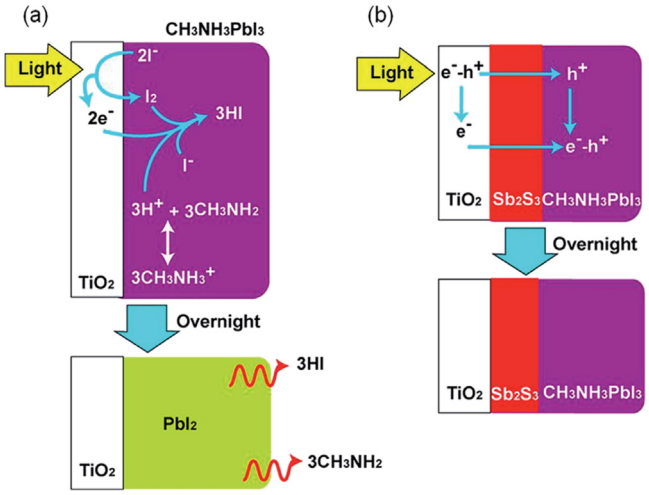

Figure 3.18 Scheme of UV-light degradation of hybrid perovskites (a) without an SbS blocking layer, and (b) with SbS blocking layer [253].

$$CH_3NH_3I\,(aq) \leftrightarrow CH_3NH_2\,(aq) + HI\,(aq) \tag{4b}$$

$$4HI\,(aq) + O_2\,(g) \leftrightarrow 2I_2\,(s) + 2H_2O\,(l) \tag{4c}$$

$$2HI\,(aq) + h\nu \leftrightarrow H_2 \uparrow\,(g) + I_2\,(s) \tag{4d}$$

In an effort to overcome this light instability, Ito and coworkers employed a Sb_2S_3 surface blocking layer showing significantly enhanced stability (Fig. 3.18), serving to suppress electron extraction at the TiO_2—perovskite interface [253].

Leijtens and company have shown that an oxygen environment is necessary for TiO_2-based devices as encapsulation within a nitrogen environment showed significant degradation of the TiO_2 photoanode and rapid decay of cell efficiencies over time [117,272]. Replacement of TiO_2 with an alumina scaffold has shown improvements in stability [271]. When exposed to moisture, a normal device employing TiO_2 degrades to a performance of 20% of the initial PCE, whereas with an Al_2O_3 layer the performance after exposure is approximately 43% of the initial PCE. Furthermore, Chandler and co-workers have demonstrated enhanced stability by utilizing a UV-filter that absorbs UV light and emits visible light, effectively preventing UV light from reaching the TiO_2 film at all. Employing this concept has produced devices retaining more than 50% of their initial efficiency [273].

Chemical stability

Components from adjacent materials, solvents, solutes, and impurities introduced through the various processing methods used for perovskites may also induce degradation. For instance, Niu et al. have shown that the common HTM additive, 4-tert-butylpyridine (TBP), can facilitate degradation of the perovskite film by the dissolution of PbI_2 into TBP via the formation of $PbI_2 \times$ TBP complexes [32,271]. Montmorillonite (MMT) has been introduced as a buffer layer in an attempt to prevent corrosion of the perovskite film by TBP. Furthermore, commonly employed additive solvents such as acetonitrile, with the commonly used Li-TFSI (Li-bis(trifluoromethanesulfonyl)imide) HTM additive, and ammonia gas (NH_3) can corrode perovskite films [274].

Hysteresis

A rather intriguing, yet vastly prominent effect of anomalous hysteresis in current–voltage (J–V) measurements has been observed for hybrid perovskites [250,275,276]. This effect, sensitive to parameters of scan direction, delay time, light intensity, and applied bias, can lead to misinterpretation of device efficiencies [250]. Preconditioning effects, that is, conditions immediately prior to measurement induce a ''scan history'' that largely influences hysteresis effects [250]. It was found that when held at open circuit conditions just before measurement, the hysteresis effect may appear to vanish at high scan rates [250]. However, this is not sufficient evidence to claim the absence of hysteresis effects. Numerous efforts have been made to examine the origin of the observed hysteresis effects, which are highly suspected to arise from the perovskite material, the contacts, ETL and HTL buffer layers, and the overall device architecture. Thus far, three major contributors to hysteresis have been suggested: (1) carrier traps resulting from a large defect density within or near the surface of the material; (2) dipole ordering resulting from ferroelectric properties and polarization of the material; and (3) ion migration due to excess ions that serve as interstitial defects. These hypotheses were experimentally observed to correlate to the resulting anomalous behavior, which will be discussed shortly.

Surface and interfacial defects

Defects located at surfaces or interfaces of the perovskite material provide one possible explanation for the observed hysteresis [159,276]. The existence of carrier traps due to defects at surfaces/interfaces that, at short-circuit conditions, slowly release trapped carriers as they transfer to interfaces, can result in reduced performance. It is well known from theoretical calculations that deep lying defects within the bulk of the perovskite film are not dominant. However, film processing may cause imperfections and produce dangling defect states, mainly located at grain boundaries and interfaces within the material. Shao et al. argued that photocurrent hysteresis is attributed to interface and grain boundary defects in the perovskite material [159]. By depositing PCBM onto the perovskite layer with thermal annealing, the defects at free surfaces and grain boundaries were successfully passivated. Trap state densities were obtained by thermal admittance spectroscopy, which showed that PCBM coating can effectively reduce the amount of defect states at the interface between perovskite and the HTL. In addition, post-annealing of PCBM can initiate its infiltration deeper within the perovskite film to achieve passivation along grain boundaries.

In accordance with these results regarding defect-induced hysteresis, it has been demonstrated by multiple groups that perovskite crystals with larger grain sizes show less prominent hysteresis effects for various device configurations [93,250,252,277]. It has been found that charges are stored within small grained samples and in planar device structures [252]. Therefore, a higher quantity of trap states is present for small grains as they possess more grain boundaries and interfacial area acting as trap sites. This finding directly supports that a reduced amount of grain boundaries in combination with PCBM passivation of surface defects can alleviate the anomalous hysteresis seen for I–V curves. In addition, the TiO_2/perovskite interface has been observed to correlate to hysteresis. By optimizing the thickness of TiO_2 scaffolds, the hysteresis phenomenon can be resolved to a large extent [93]. For the case of no n- or p-type interface, the rate of trap release may increase due to heightened recombination at the unblocked contacts resulting in enhanced hysteresis. This proposed mechanism cannot explain the rise in photoconductivity seen over time [276]. Thus we can see that the type of transport layer used, that is, p- or n-type, affects the magnitude of hysteresis. Furthermore, it has been shown that architecture (mesoporous, planar heterojunction, mesosuperstructure) has an effect on hysteresis [275]. This will undoubtedly result in different surface defect states according to the morphology of the employed architecture.

Ferroelectric dipole ordering

Apart from defects, ferroelectric properties of perovskite structures may contribute to hysteresis [278,279]. The applied electrical field is considered an external force that disturbs the polarity of the MA ions within the film. The response and redistribution of the MA ions is suspected to cause the asymmetric I–V curve observed between forward and reverse scan [26]. These ferroelectric domains would cause an unbalanced charge transport of electron and holes within the electrical field domain. Ferroelectric domains have been further observed through piezoresponse force microscopy, which have shown a reversible switching upon poling with a DC bias [280]. Additionally, Chen et al. have confirmed bias poling effects on perovskite materials, where reverse bias poling resulted in a severe hysteresis effect [279]. It is postulated that forward bias poling can reduce hysteresis effects by breaking the dipoles from a highly ordered state to random state. Although the relaxation process is fast, is has been claimed that the rotation and vibration of the MA ions plays an important role in determining device performance. A recent study by Bertoluzzi et al. measured photovoltage decay in an effort to elucidate the coupled electronic-structural phenomena for which they observed two distinct decay stages [281]. Rapid transients were observed on the millisecond time scale, which are common response times for most solar devices. However over a 10–100-s time scale a power law scale was observed, commonly seen for relaxation of polymers or glassy materials. These findings evidence that slow responses to perturbations occur and, as such, are likely associated with ferroelectric effects. In addition, Gottesman et al. proposed that the slow polarization response is a result of a binding energy reduction due to an $I \rightarrow Pb$ charge transfer that depletes the negative charge carried by I. Since MA and I are primarily hydrogen bonded, excitation would result in less attraction in the hydrogen bond, allowing the polar MA ions to rotate more freely thus inducing dipole ordering and structural change of the inorganic framework [276]. The controlling of the domain formation could be an interesting topic to have hysteresis free devices and the detail studies on the effects of the ferroelectric properties in hybrid materials can benefit to the future material designs.

Ion migration

The third possible mechanism has been examined by Tress et al., whom speculated that an applied voltage may induce ion migration for which excess ions could accumulate at interfaces and effectively screen the applied field, modifying the built-in potential [282]. This process occurs on the timescale of seconds to minutes, providing some justification for their hypothesis. A delayed reduction in the built-in potential could explain why there is a dependence on voltage sweep rate and direction for *J*—*V* measurements. Even though there was no direct evidence of ion migration effects, recent works by Xiao and co-workers have provided supportive evidence to this proposed mechanism [88]. However, this mechanism may also be attributed to the electrical poling process, which would explain why conditions immediately prior to measurement induce a scan-history that largely influences hysteresis effects. It has also been proposed that upon illumination and applied bias, negatively charged I^- anions migrate toward the cathode, and likewise the positive MA cations migrate toward the anode, effectively creating an extraction barrier for both types of carriers at their selective contacts [250]. This effect would explain the s-shaped *I*—*V* curves observed, as well as the sensitivity to previous *I*—*V* bias history. As such, further investigations to distinguish these two mechanisms are necessary to provide a better understanding of ion migration contributions to the observed electrical properties.

Despite the proposed mechanisms that have been reported, a clear picture of the observed hysteresis phenomena is not yet provided. More efforts to distinguish the unique properties of perovskites may accelerate material development and device applications in the near future.

Applications beyond PV

Beyond the photovoltaic practice, hybrid perovskite semiconductors are expected to be incorporated into other functional devices as a result of the superior performances seen in PV applications that include low trap density of states, high carrier mobility and quantum efficiency [155]. Potential applications extend to various types of solution-processed semiconductor devices [283] such as photodetectors [284—286], light emitting diodes (LED) [287,288], lasers [152,153], and thin film transistors (TFTs) [289]. In this section, we review and discuss some of the latest advancements pertaining to these applications and identify the correlation between material properties and device-specific functionalities.

Photodetector

A quality solar cell is able to function as a photovoltaic type photodetector. Furthermore, transistor-type photodetectors have been reported utilizing the photoconductivity of perovskite materials. Dou and Yang have reported high-performance photodetectors from hybrid perovskite based photovoltaic cells [284]. This photovoltaic cell, as shown in Fig. 4.1a, has a power conversion efficiency around 12% under normal 1 sun conditions. They found the dark current of the diode under reverse bias to reach 10^{-9} mA/cm^2, while its photoresponsivity was as high as 0.4 A/W in the visible spectral range. As shown in Fig. 4.1b, very high a detectivity close to 10^{14} Jones was obtained, which is one order of magnitude better than that of the traditional Si photodetector within the same wavelength range. An ideal photodetector should exhibit an extremely fast response to incident radiation. In photovoltaic type photodetectors, film thicknesses are within the range of several hundreds of nanometers, and since the charge diffusion length in perovskite polycrystalline films is on the same order both high quantum yield and fast responses can be obtained. Another significant effect of device architecture on photodetector performance is related to the hysteresis behavior of perovskite based photovoltaic cells. Though it is difficult to elucidate the real mechanisms behind the hysteresis at this stage, any delayed photoresponse upon light excitation ought to be minimized. For a p—i—n device structure using a polyelectrolyte as the p-type layer, perovskite as the intrinsic layer, and a fullerene derivative n-type layer, photoresponse times (rising and decay time of the transient photocurrent) are approximately 300 ns, allowing for operation at frequencies of several MHz. The result also indicates that hysteresis may be strongly related to interfacial contact of perovskite with adjacent charge transport layers.

When a perovskite layer is sandwiched in a n—i—p structure, for which the n-layer is a metal-oxide (TiO_2 or ZnO)

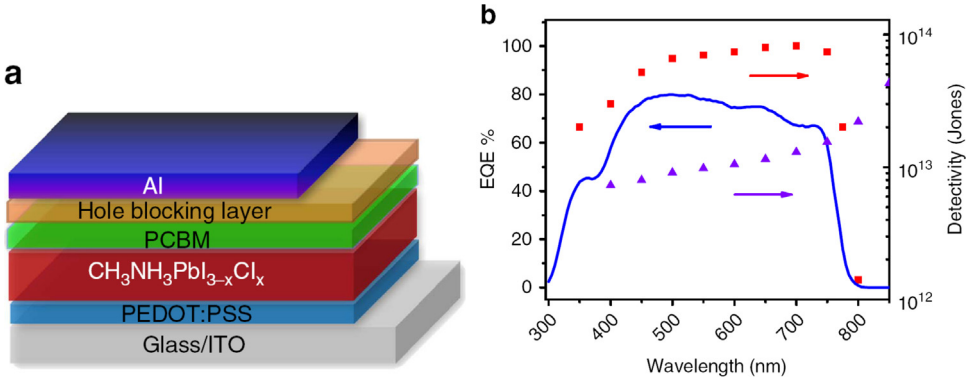

Figure 4.1 (a) Device structure of the hybrid perovskite photodetector; (b) External quantum efficiency and detectivity of the hybrid perovskite photodetector at different wavelengths. The detectivity of a single-crystalline silicon diode (purple triangle) is shown for comparison [284].

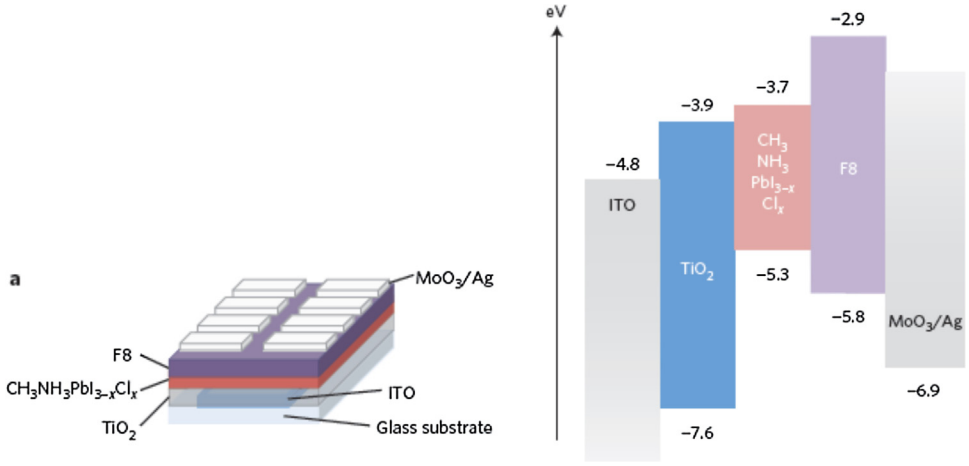

Figure 4.2 Structure and energy-level diagram of the perovskite light-emitting diode (PLED). (a) Device architecture of the $MAPbI_{3-x}Cl_x$ PLED and (b) energy-level diagram of different layers of materials in the infrared PLED, showing conduction and valence band levels with respect to vacuum [287].

and the p-layer is doped Spiro-MeOTAD, response times have been observed to delay from 0.1 s to 30 s. A very high photoresponsivity of 3.49 A/W at a wavelength of 365 was reported. Such a non-linear photoresponse indicates strong light induced charge injection from the cathode side, which might also related to the slow response due to trap filling processes occurring at the interface [290]. It is worth noting that such photodetectors exhibit even higher photoresponsivity as the large channel width is able to accommodate high photocurrents. However, as charge transport distance strongly influences photoresponse speed, the channel length shall ultimately be the limiting factor. While reducing the channel length to a micrometer scale is a possible solution to reduce the response time, it will likely cause complication in processing for transistor fabrication. To further enhance photodetector performance, the combination of perovskites with other electronic materials is a promising route. For instance, a graphene-perovskite hybrid type photodetector was reported, reaching a responsivity and external quantum efficiency of 180 A/W and 5×10^4%, respectively [291]. Dong and Huang et al. employed a high bandgap hole transport layer in combination with perovskite photoactive layers, achieving a high performance photovoltaic type photodetector [286].

LED and laser

As described by the Shockley—Queisser limit, an ideal photovoltaic material exhibits radiative decay as the only channel for charge recombination (detailed balance). As there has been a rapid increase in photovoltaic efficiency in recent years, it has been recognized that hybrid perovskites possess very high PL quantum yields near 70% at room temperature and approaching 100% at 195 K [292]. This not only explains the high photovoltaic performance, but strongly suggests an application for light emitting devices [293].

Tan and Friend et al. demonstrated a bright electroluminescence via perovskites [287]. The emission color can be changed by tuning the composition of the perovskite layer. $MAPbI_3$ emits light around 780 nm. Introduction of Br^- to replace I^- causes emissive band shifting to red and green colors. A sandwich structure was used to confine the charge recombination within the emissive layer, and use of quantum well structures offers an excellent EL external quantum efficiency of ~0.8%. As shown in Fig. 4.2, the perovskite layer is sandwiched between a TiO_2 ETL and a polymer HTL, enabling efficient charge injection. Another example has been demonstrated on flexible substrates by Kim et al., further confirming the effectiveness of charge blocking layers for efficient charge recombination within the perovskite layer [288]. The LED devices are bendable, similar to those demonstrated by You et al. for photovoltaic cells [71]. Alternative charge injection and transport materials have also been employed aiming to rationalize the energy diagrams of the EL devices [294]. The quantum yield in these devices is below 1%, which may stem from severe quenching and/or unbalanced charge injection.

Intrinsically, the hybrid perovskite materials have high PL quantum yield due to their high film quality. In addition, the PL lifetime is on the order of a few hundred nanoseconds, longer than that for normal direct bandgap semiconductors, such as GaAs (only a few nanoseconds). Such a laser device can be fabricated via low-cost solution processes, making them highly attractive as electrically pumped lasers. Amplified simultaneous emission (ASE) and even lasing behaviors have been reported from both cavity and non-cavity modes [152,153,295]. Xing et al. reported a very low threshold ($12\ \mu J/cm^2$) ASE from $MAPbI_3$ films, as clearly shown in Fig. 4.3. Their finding indicates that radiative recombination via ASE successfully overcomes both bulk (traps and Auger) and interface (defects) recombination, becoming the dominant channel. This is a very surprising observation, and it remains unclear why the ASE occurs on such an extremely fast (<10 ps) time scale. In addition, emission colors can be readily tuned via changing the composition in the perovskite layer. Measured quantum yields of simultaneous PL emissions ranging from 20% to 70% have been reported by various

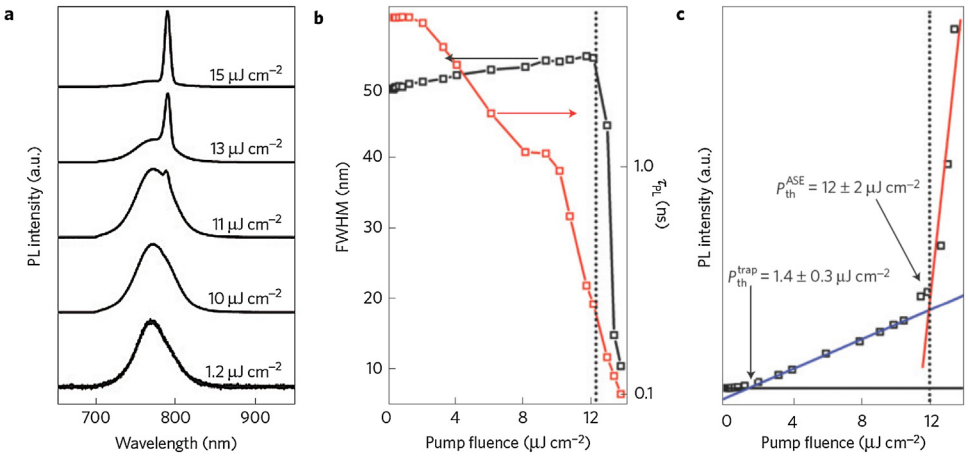

Figure 4.3 Coherent light emission from solution-processed perovskite films. (a) Steady-state PL emission spectra from a 65-nm-thick $MAPbI_3$ film photoexcited using 600 nm, 150 fs and 1 kHz pump pulses with increasing pump fluence (per pulse) — illustrating the transition from SE to ASE. (b) FWHM of the emission peak and average transient PL lifetime (τ_{PL}) as a function of the pump fluence. τ_{PL} is the time taken for the intensity to decrease to $1/e$ of its initial value. (c) PL intensity as a function of pump fluence. The arrows indicate the trap state saturation threshold fluence (P_{th}^{trap}) and the ASE threshold fluence (P_{th}^{ASE}). The blue and red lines represent the linear fits to experimental data in the two linear regimes of SE and ASE, respectively. The dashed vertical black lines in b and c indicate the onset of ASE [153].

groups, indicating that film properties are very sensitive to processing parameters and measurement conditions as we have seen for PV applications [293]. Moreover, lasing from planar and spherical optical cavities also strongly suggests the great potential of hybrid perovskites for application in solid-state electrical-pump lasers [152,295].

Transistors

As one of the early inorganic solution processable materials, hybrid tin perovskites have been intensively studied for thin film transistors (TFT) for potential applications in microelectronics. Hall effect measurement shows very high estimated electron and hole mobility that exceed 2000 cm^2/Vs and 300 cm^2/Vs [36]. However, transistors based on lead based perovskites have hardly been seen. Nevertheless, Soci and company have demonstrated light-emitting characteristics from $MAPbI_3$ in a bottom-contact transistor configuration. It has been confirmed that the compound is ambipolar in nature, and carrier mobilities measured at low temperature are well below 1 cm^2/Vs, much lower than expected values [289]. More importantly electronic properties are discussed, shedding light on further investigation of charge transport mechanisms in perovskite materials.

Future outlook

In summary, we have portrayed a comprehensive understanding of hybrid perovskite materials for applications in photovoltaics and other optoelectronics technologies. As an organic—inorganic hybrid material, $MAPbX_3$ perovskites effectively combine the attributes of the inorganic framework and the intercalated organic species, and as such are highly distinguished among other hybrid materials. Through its development, perovskite materials have come to feature high absorption coefficients, long carrier lifetimes and diffusion lengths, ambipolar carrier transport, and shallow defect levels. As has been carefully reviewed, their application in thin film optoelectronics has been intensively exploited with remarkable progress.

From the perspective of photovoltaics, the adoption of hybrid perovskite materials has achieved significant progress in terms of device architecture, working mechanism, film formation, and interface engineering. It is realized that the most efficient perovskite solar cells follow a p—i—n configuration, with an abundant selection of p- and n-type materials for efficient carrier extraction. Film fabrication of hybrid perovskite materials is of crucial importance as it determines film texture, crystal structure, composition, and defect formation that collectively contribute toward overall device performance. Furthermore, interface engineering has proven to effectively optimize device performance as it affects carrier dynamics across the entire device including charge generation, transportation, and collection. Aside from single-junction perovskite solar cells, the construction of tandem devices to combine the other low band gap materials also provides a feasible approach for this material to competing with crystal silicon based technologies. Tandem perovskite devices have been predicted to enhance power conversion efficiency to levels that may exceed the theoretical limit by efficient light harvesting in an economic manner.

Beyond PV applications, perovskite materials with high crystallinity, emission efficiency, and low concentration of defects enables the fabrication of light-emitting diodes, lasers, photodetectors, and other optoelectronic/microelectronic devices. Furthermore, its high atomic number and high density may find its way into applications for high energy radiation detection. Additionally,

perovskites exhibit interesting ferroelectric properties potentially due to the free rotation of the polar organic species, which further endows their potential use for switchable electronics and memory devices.

Despite the phenomenal properties of hybrid perovskites, several crucial challenges that include toxicity and instability prevent industrial scale use. Limited success has been reported for the replacement of Pb with environmental friendly elements due to lack of choices for substitution. Non-toxic Sn shares comparatively similar properties to Pb in organic—inorganic hybrids perovskites, and theoretically ought to perform more efficiently. However, Sn-based perovskite solar cells experience heightened levels of instability due to the naturally favorable oxidation of Sn(II), inevitably requiring an advanced encapsulation technique to overcome. Apart from the toxicity, Pb-based perovskites experience inherent instability under working conditions that are an even more urgent to address. The degradation mechanisms of perovskites upon exposure to thermal, moisture, UV and mechanical conditions require a plausible strategy in order to improve material stability. Encouraging results have been demonstrated through interface modifications between transport materials and electrodes, realizing device stabilities exceeding 1000 h. However, in considering the durability requirements of terrestrial-use that exceed 20 years in the field for deployed solar cells, there is still much work to be done to improve the intrinsic properties of hybrid perovskites (e.g. ionic nature of organic species) toward more stable device structures.

From an academic research perspective, it is well-observed that the success of this emerging organic—inorganic hybrid perovskite material serves as an excellent example to bridge the organic and organic realms. Further research efforts can be continuously made to (1) investigate the interaction between organic and inorganic species to better utilize the advantages of both components; (2) provide a deep understanding of the structure—property relationships of the entire hybrid material system to guide the rational design and careful manipulation of the optoelectronic properties. In addition, theoretical calculations regarding band structure, defect properties, and carrier behavior of this material have not yet been fully exploited. It is important to couple together theory with experimental exploration of material properties based on single crystals and thin films. The knowledge applied in organic—inorganic hybrid perovskite systems can also be extended to other optoelectronic materials toward higher performances. With the substantial ongoing efforts toward the development of hybrid perovskite materials, environmental friendly and reliable photovoltaic technologies yielding low costs and high performance will assuredly be realized in the future.

Acknowledgments

This work was financially supported by a grant from the National Science Foundation (grant no. ECCS-1202231, Program Director Dr. George N. Maracas), Air Force Office of Scientific Research (grant no. FA9550-12-1-0074, Program Manager Dr Charles Lee), and UCLA Internal Funds. The authors sincerely acknowledge Mr. Yihao Fang for his contributions with figures.

References

[1] H.J. Snaith, J. Phys. Chem. Lett. 21 (2013) 3623—3630.
[2] N.-G. Park, Mater. Today 18 (2015) 65—72.
[3] M. Gratzel, Nat. Mater. 13 (2014) 838—842.
[4] M.A. Green, A. Ho-Baillie, H.J. Snaith, Nat. Photonics 8 (2014) 506—514.
[5] Research Cell Efficiency Records, NREL (2015). http://www.nrel.gov/ncpv/images/efficiency_chart.jpg
[6] J. Burschka, N. Pellet, S.-J. Moon, R. Humphry-Baker, P. Gao, M.K. Nazeeruddin, M. Gratzel, Nature 499 (2013) 316—319.
[7] M. Liu, M.B. Johnston, H.J. Snaith, Nature 501 (2013) 395—398.
[8] H. Zhou, Q. Chen, G. Li, S. Luo, T.-b. Song, H.-S. Duan, Z. Hong, J. You, Y. Liu, Y. Yang, Science 345 (2014) 542—546.
[9] N.J. Jeon, J.H. Noh, W.S. Yang, Y.C. Kim, S. Ryu, J. Seo, S.I. Seok, Nature 517 (2015) 476—480.
[10] M.A. Pena, J.L.G. Fierro, Chem. Rev. 101 (2001) 1981—2017.
[11] C.K. Moller, Nature 182 (1958) 1436.
[12] D. Weber, Inst. Anorg. Chem. Univ. Stutt. 33b (1978) 1443—1445.
[13] D.B. Mitzi, Prog. Inorg. Chem. 48 (2007) 1—121.
[14] A. Kojima, K. Teshima, T. Miyasaka, Y. Shirai, Proc. 210th ECS Meeting, ECS, 2006.
[15] A. Kojima, K. Teshima, Y. Shirai, T. Miyasaka, J. Am. Chem. Soc. 131 (2009) 6050—6051.
[16] J.-H. Im, C.-R. Lee, J.-W. Lee, S.-W. Park, N.-G. Park, Nanoscale 3 (2011) 4088—4093.
[17] H.S. Kim, C.R. Lee, J.H. Im, K.B. Lee, T. Moehl, A. Marchioro, S.J. Moon, R. Humphry-Baker, J.H. Yum, J.E. Moser, M. Gratzel, N.G. Park, Sci. Rep. 2 (2012) 591.
[18] L. Etgar, P. Gao, Z. Xue, Q. Peng, A.K. Chandiran, B. Liu, M.K. Nazeeruddin, M. Grätzel, J. Am. Chem. Soc. 134 (2012) 17396—17399.
[19] M.M. Lee, J. Teuscher, T. Miyasaka, T.N. Murakami, H.J. Snaith, Science 338 (2012) 643—647.
[20] J.-Y. Jeng, Y.-F. Chiang, M.-H. Lee, S.-R. Peng, T.-F. Guo, P. Chen, T.-C. Wen, Adv. Mater. 25 (2013) 3727—3732.
[21] Q. Chen, H. Zhou, Z. Hong, S. Luo, H.-S. Duan, H.-H. Wang, Y. Liu, G. Li, Y. Yang, J. Am. Chem. Soc. 136 (2013) 622—625.
[22] J.H. Noh, S.H. Im, J.H. Heo, T.N. Mandal, S.I. Seok, Nano Lett. 13 (2013) 1764—1769.
[23] Goldschmidt, Ber. Dtsch. Chem. 60 (1927) 1263—1268.
[24] A.S. Bhalla, R.Y. Guo, R. Roy, Mater. Res. Innov. 4 (2000) 3—26.
[25] Y.H. Chang, C.H. Park, J. Korean Phys. Soc. 44 (2004) 889—893.
[26] J.M. Frost, K.T. Butler, F. Brivio, C.H. Hendon, M. van Schilfgaarde, A. Walsh, Nano Lett. 14 (2014) 2584—2590.
[27] F. Brivio, A.B. Walker, A. Walsh, APL Mater. 1 (2013) 042111.
[28] P. Umari, E. Mosconi, F. De Angelis, Sci. Rep. 4 (2014) 4467.
[29] T. Umebayashi, K. Asai, T. Kondo, A. Nakao, Phys. Rev. B 67 (2003) 155405.
[30] M. Johnsson, P. Lemmens, Handbook of Magnetism and Advanced Magnetic Materials, John Wiley & Sons, Ltd., 2007.
[31] C. Li, X. Lu, W. Ding, L. Feng, Y. Gao, Z. Guo, Acta Crystallogr. Sect. B: Struct. Sci. 64 (2008) 702—707.
[32] G. Niu, X. Guo, L. Wang, J. Mater. Chem. A 3 (2015) 8970.
[33] E. Mosconi, A. Amat, M.K. Nazeeruddin, M. Grätzel, F. De Angelis, J. Phys. Chem. C 117 (2013) 13902—13913.
[34] A. Poglitsch, D. Weber, J. Chem. Phys. 87 (1987) 6373—6378.
[35] T. Baikie, Y. Fang, J.M. Kadro, M. Schreyer, F. Wei, S.G. Mhaisalkar, M. Graetzel, T.J. White, J. Mater. Chem. A 1 (2013) 5628—5641.

[36] C.C. Stoumpos, C.D. Malliakas, M.G. Kanatzidis, Inorg. Chem. 52 (2013) 9019—9038.
[37] I. Borriello, G. Cantele, D. Ninno, Phys. Rev. B 77 (2008) 235214.
[38] S. Pang, H. Hu, J. Zhang, S. Lv, Y. Yu, F. Wei, T. Qin, H. Xu, Z. Liu, G. Cui, Chem. Mater. 26 (2014) 1485—1491.
[39] G.E. Eperon, S.D. Stranks, C. Menelaou, M.B. Johnston, L.M. Herz, H.J. Snaith, Energy Environ. Sci. 7 (2014) 982—988.
[40] J.-H. Im, J. Chung, S.-J. Kim, N.-G. Park, Nanoscale Res. Lett. 7 (2012) 353.
[41] S. Aharon, A. Dymshits, A. Rotem, L. Etgar, J. Mater. Chem. A 3 (2015) 9171.
[42] M.I. Dar, N. Arora, P. Gao, S. Ahmad, M. Gratzel, M.K. Nazeeruddin, Nano Lett. 14 (2014) 6991—6996.
[43] N.K. McKinnon, D.C. Reeves, M.H. Akabas, J. Gen. Physiol. 138 (2011) 453—466.
[44] O.D. Miller, E. Yablonovitch, S.R. Kurtz, IEEE J. Photovolt. 2 (2012) 303—311.
[45] B.N. Cohen, C. Labarca, N. Davidson, H.A. Lester, J. Gen. Physiol. 100 (1992) 373—400.
[46] T.M. Koh, K. Fu, Y. Fang, S. Chen, T.C. Sum, N. Mathews, S.G. Mhaisalkar, P.P. Boix, T. Baikie, J. Phys. Chem. C 118 (2013) 16458—16462.
[47] N. Pellet, P. Gao, G. Gregori, T.-Y. Yang, M.K. Nazeeruddin, J. Maier, M. Grätzel, Angew. Chem. Int. Ed. 53 (2014) 3151—3157.
[48] D.E. Scaife, P.F. Weller, W.G. Fisher, J. Solid State Chem. 9 (1974) 308—314.
[49] Z. Chen, C. Yu, K. Shum, J.J. Wang, W. Pfenninger, N. Vockic, J. Midgley, J.T. Kenney, J. Lumin. 132 (2012) 345—349.
[50] I. Chung, J.-H. Song, J. Im, J. Androulakis, C.D. Malliakas, H. Li, A.J. Freeman, J.T. Kenney, M.G. Kanatzidis, J. Am. Chem. Soc. 134 (2012) 8579—8587.
[51] D.B. Mitzi, C.A. Feild, Z. Schlesinger, R.B. Laibowitz, J. Solid State Chem. 114 (1995) 159—163.
[52] J.-W. Lee, D.-J. Seol, A.-N. Cho, N.-G. Park, Adv. Mater. 26 (2014) 4991—4998.
[53] H. Choi, J. Jeong, H.-B. Kim, S. Kim, B. Walker, G.-H. Kim, J.Y. Kim, Nano Energy 7 (2014) 80—85.
[54] A. Mei, X. Li, L. Liu, Z. Ku, T. Liu, Y. Rong, M. Xu, M. Hu, J. Chen, Y. Yang, M. Grätzel, H. Han, Science 345 (2014) 295—298.
[55] F. Hao, C.C. Stoumpos, D.H. Cao, R.P.H. Chang, M.G. Kanatzidis, Nat. Photonics 8 (2014) 489—494.
[56] C. Bernal, K. Yang, J. Phys. Chem. C 118 (2014) 24383—24388.
[57] A.S. Ionkin, W.J. Marshall, B.M. Fish, Organometallics 25 (2006) 4170—4178.
[58] S.P.R.D. Madan, Mod. Inorg. Chem. (1987) 207—212.
[59] Y. Ogomi, A. Morita, S. Tsukamoto, T. Saitho, N. Fujikawa, Q. Shen, T. Toyoda, K. Yoshino, S.S. Pandey, T. Ma, S. Hayase, J. Phys. Chem. Lett. 5 (2014) 1004—1011.
[60] F. Zuo, S.T. Williams, P.-W. Liang, C.-C. Chueh, C.-Y. Liao, A.K.Y. Jen, Adv. Mater. 26 (2014) 6454—6460.
[61] N.K. Noel, S.D. Stranks, A. Abate, C. Wehrenfennig, S. Guarnera, A.-A. Haghighirad, A. Sadhanala, G.E. Eperon, S.K. Pathak, M.B. Johnston, A. Petrozza, L.M. Herz, H.J. Snaith, Energy Environ. Sci. 7 (2014) 3061—3068.
[62] I. Chung, B. Lee, J. He, R.P.H. Chang, M.G. Kanatzidis, Nature 485 (2012) 486—489.
[63] M. Jiang, J. Wu, F. Lan, Q. Tao, D. Gao, G. Li, J. Mater. Chem. A 3 (2015) 963—967.
[64] S.D. Stranks, G.E. Eperon, G. Grancini, C. Menelaou, M.J.P. Alcocer, T. Leijtens, L.M. Herz, A. Petrozza, H.J. Snaith, Science 342 (2013) 341—344.
[65] S. Colella, E. Mosconi, P. Fedeli, A. Listorti, F. Gazza, F. Orlandi, P. Ferro, T. Besagni, A. Rizzo, G. Calestani, G. Gigli, F. De Angelis, R. Mosca, Chem. Mater. 25 (2013) 4613—4618.
[66] A. Dualeh, N. Tétreault, T. Moehl, P. Gao, M.K. Nazeeruddin, M. Grätzel, Adv. Funct. Mater. 24 (2014) 3250—3258.
[67] E. Edri, S. Kirmayer, M. Kulbak, G. Hodes, D. Cahen, J. Phys. Chem. Lett. 5 (2014) 429—433.
[68] E.L. Unger, A.R. Bowring, C.J. Tassone, V.L. Pool, A. Gold-Parker, R. Cheacharoen, K.H. Stone, E.T. Hoke, M.F. Toney, M.D. McGehee, Chem. Mater. 26 (2014) 7158—7165.
[69] Y. Tidhar, E. Edri, H. Weissman, D. Zohar, G. Hodes, D. Cahen, B. Rybtchinski, S. Kirmayer, J. Am. Chem. Soc. 136 (2014) 13249—13256.
[70] H. Yu, F. Wang, F. Xie, W. Li, J. Chen, N. Zhao, Adv. Funct. Mater. 24 (2014) 7102—7108.
[71] J. You, Z. Hong, Y. Yang, Q. Chen, M. Cai, T.-B. Song, C.-C. Chen, S. Lu, Y. Liu, H. Zhou, Y. Yang, ACS Nano 8 (2014) 1674—1680.
[72] S.T. Williams, F. Zuo, C.-C. Chueh, C.-Y. Liao, P.-W. Liang, A.K.Y. Jen, ACS Nano 8 (2014) 10640—10654.
[73] S. Colella, E. Mosconi, G. Pellegrino, A. Alberti, V.L.P. Guerra, S. Masi, A. Listorti, A. Rizzo, G.G. Condorelli, F. De Angelis, G. Gigli, J. Phys. Chem. Lett. 5 (2014) 3532—3538.
[74] T.-W. Ng, C.Y. Chan, M.-F. Lo, Z. Guan, C.-S. Lee, J. Mater. Chem. A 3 (2015) 9081—9085.
[75] S. Nagane, U. Bansode, O. Game, S. Chhatre, S. Ogale, Chem. Commun. 50 (2014) 9741—9744.
[76] A. Dualeh, T. Moehl, N. Tétreault, J. Teuscher, P. Gao, M.K. Nazeeruddin, M. Grätzel, ACS Nano 8 (2013) 362—373.
[77] G. Giorgi, J.-I. Fujisawa, H. Segawa, K. Yamashita, J. Phys. Chem. Lett. 4 (2013) 4213—4216.
[78] C.S. Ponseca, T.J. Savenije, M. Abdellah, K. Zheng, A. Yartsev, T. Pascher, T. Harlang, P. Chabera, T. Pullerits, A. Stepanov, J.-P. Wolf, V. Sundström, J. Am. Chem. Soc. 136 (2014) 5189—5192.
[79] Q. Dong, Y. Fang, Y. Shao, P. Mulligan, J. Qiu, L. Cao, J. Huang, Science (2015).
[80] J. Qiu, Y. Qiu, K. Yan, M. Zhong, C. Mu, H. Yan, S. Yang, Nanoscale 5 (2013) 3245—3248.
[81] S. De Wolf, J. Holovsky, S.-J. Moon, P. Löper, B. Niesen, M. Ledinsky, F.-J. Haug, J.-H. Yum, C. Ballif, J. Phys. Chem. Lett. 5 (2014) 1035—1039.
[82] G. Xing, N. Mathews, S. Sun, S.S. Lim, Y.M. Lam, M. Grätzel, S. Mhaisalkar, T.C. Sum, Science 342 (2013) 344—347.
[83] E. Edri, S. Kirmayer, A. Henning, S. Mukhopadhyay, K. Gartsman, Y. Rosenwaks, G. Hodes, D. Cahen, Nano Lett. 14 (2014) 1000—1004.
[84] J.H. Heo, S.H. Im, J.H. Noh, T.N. Mandal, C.-S. Lim, J.A. Chang, Y.H. Lee, H.-J. Kim, A. Sarkar, M.K. Nazeeruddin, M. Grätzel, S.I. Seok, Nat. Photonics 7 (2013) 486—491.
[85] I. Grinberg, D.V. West, M. Torres, G. Gou, D.M. Stein, L. Wu, G. Chen, E.M. Gallo, A.R. Akbashev, P.K. Davies, J.E. Spanier, A.M. Rappe, Nature 503 (2013) 509—512.
[86] S.Y. Yang, J. Seidel, S.J. Byrnes, P. Shafer, C.H. Yang, M.D. Rossell, P. Yu, Y.H. Chu, J.F. Scott, J.W. Ager, L.W. Martin, R. Ramesh, Nat. Nanotechnol. 5 (2010) 143—147.
[87] V. D'Innocenzo, G. Grancini, M.J.P. Alcocer, A.R.S. Kandada, S.D. Stranks, M.M. Lee, G. Lanzani, H.J. Snaith, A. Petrozza, Nat. Commun. 5 (2014) 3586.
[88] Z. Xiao, Y. Yuan, Y. Shao, Q. Wang, Q. Dong, C. Bi, P. Sharma, A. Gruverman, J. Huang, Nat. Mater. 14 (2015) 193—198.
[89] A. Pisoni, J. Jaćimović, O.S. Barišić, M. Spina, R. Gaál, L. Forró, E. Horváth, J. Phys. Chem. Lett. 5 (2014) 2488—2492.
[90] D. Liu, J. Yang, T.L. Kelly, J. Am. Chem. Soc. 136 (2014) 17116—17122.
[91] H.S. Kim, C.R. Lee, I.H. Jang, W. Kang, N.G. Park, Bull. Korean Chem. Soc. 33 (2012) 670—674.
[92] N.-G. Park, J. Phys. Chem. Lett. 4 (2013) 2423—2429.
[93] N.J. Jeon, J.H. Noh, Y.C. Kim, W.S. Yang, S. Ryu, S.I. Seok, Nat. Mater. 13 (2014) 897—903.

[94] X. Zhang, Z. Bao, X. Tao, H. Sun, W. Chen, X. Zhou, RSC Adv. 4 (2014) 64001—64005.
[95] H.-S. Kim, J.-W. Lee, N. Yantara, P.P. Boix, S.A. Kulkarni, S. Mhaisalkar, M. Grätzel, N.-G. Park, Nano Lett. 13 (2013) 2412—2417.
[96] K. Manseki, T. Ikeya, A. Tamura, T. Ban, T. Sugiura, T. Yoshida, RSC Adv. 4 (2014) 9652—9655.
[97] D. Zhong, B. Cai, X. Wang, Z. Yang, Y. Xing, S. Miao, W.-H. Zhang, C. Li, Nano Energy 11 (2015) 409—418.
[98] Y. Xiao, G. Han, Y. Li, M. Li, J. Wu, J. Mater. Chem. A 2 (2014) 16856—16862.
[99] X. Gao, J. Li, J. Baker, Y. Hou, D. Guan, J. Chen, C. Yuan, Chem. Commun. 50 (2014) 6368—6371.
[100] J.-W. Lee, S.H. Lee, H.-S. Ko, J. Kwon, J.H. Park, S.M. Kang, N. Ahn, M. Choi, J.K. Kim, N.-G. Park, J. Mater. Chem. A 3 (2015) 9179—9186.
[101] A. Sarkar, N.J. Jeon, J.H. Noh, S.I. Seok, J. Phys. Chem. C 118 (2014) 16688—16693.
[102] J.T.-W. Wang, J.M. Ball, E.M. Barea, A. Abate, J.A. Alexander-Webber, J. Huang, M. Saliba, I. Mora-Sero, J. Bisquert, H.J. Snaith, R.J. Nicholas, Nano Lett. 14 (2013) 724—730.
[103] K. Mahmood, B.S. Swain, A.R. Kirmani, A. Amassian, J. Mater. Chem. A 3 (2015) 9051—9057.
[104] P. Qin, A.L. Domanski, A.K. Chandiran, R. Berger, H.-J. Butt, M.I. Dar, T. Moehl, N. Tetreault, P. Gao, S. Ahmad, M.K. Nazeeruddin, M. Gratzel, Nanoscale 6 (2014) 1508—1514.
[105] I. Nakamura, N. Negishi, S. Kutsuna, T. Ihara, S. Sugihara, K. Takeuchi, J. Mol. Catal. A: Chem. 161 (2000) 205—212.
[106] M.H. Kumar, N. Yantara, S. Dharani, M. Graetzel, S. Mhaisalkar, P.P. Boix, N. Mathews, Chem. Commun. 49 (2013) 11089—11091.
[107] D. Bi, G. Boschloo, S. Schwarzmuller, L. Yang, E.M.J. Johansson, A. Hagfeldt, Nanoscale 5 (2013) 11686—11691.
[108] F.J. Ramos, M.C. López-Santos, E. Guillén, M.K. Nazeeruddin, M. Grätzel, A.R. Gonzalez-Elipe, S. Ahmad, ChemPhysChem 15 (2014) 1148—1153.
[109] D.-Y. Son, J.-H. Im, H.-S. Kim, N.-G. Park, J. Phys. Chem. C 118 (2014) 16567—16573.
[110] K. Mahmood, B.S. Swain, A. Amassian, Nanoscale 6 (2014) 14674—14678.
[111] J. Zhang, P. Barboux, T. Pauporté, Adv. Energy Mater. 4 (2014) 1400932.
[112] K. Mahmood, B.S. Swain, H.S. Jung, Nanoscale 6 (2014) 9127—9138.
[113] A. Bera, K. Wu, A. Sheikh, E. Alarousu, O.F. Mohammed, T. Wu, J. Phys. Chem. C 118 (2014) 28494—28501.
[114] H. Tian, B. Xu, H. Chen, E.M.J. Johansson, G. Boschloo, ChemSusChem 7 (2014) 2150—2153.
[115] H. Wang, X. Zeng, Z. Huang, W. Zhang, X. Qiao, B. Hu, X. Zou, M. Wang, Y.-B. Cheng, W. Chen, ACS Appl. Mater. Interfaces 6 (2014) 12609—12617.
[116] Z. Liu, M. Zhang, X. Xu, L. Bu, W. Zhang, W. Li, Z. Zhao, M. Wang, Y.-B. Cheng, H. He, Dalton Trans. 44 (2014) 3967—3973.
[117] T. Leijtens, G.E. Eperon, S. Pathak, A. Abate, M.M. Lee, H.J. Snaith, Nat. Commun. 4 (2013) 2885.
[118] T. Leijtens, S.D. Stranks, G.E. Eperon, R. Lindblad, E.M.J. Johansson, I.J. McPherson, H. Rensmo, J.M. Ball, M.M. Lee, H.J. Snaith, ACS Nano 8 (2014) 7147—7155.
[119] J.M. Ball, M.M. Lee, A. Hey, H.J. Snaith, Energy Environ. Sci. 6 (2013) 1739—1743.
[120] M.J. Carnie, C. Charbonneau, M.L. Davies, J. Troughton, T.M. Watson, K. Wojciechowski, H. Snaith, D.A. Worsley, Chem. Commun. 49 (2013) 7893—7895.
[121] K.W. Tan, D.T. Moore, M. Saliba, H. Sai, L.A. Estroff, T. Hanrath, H.J. Snaith, U. Wiesner, ACS Nano 8 (2014) 4730—4739.
[122] W. Zhang, M. Saliba, S.D. Stranks, Y. Sun, X. Shi, U. Wiesner, H.J. Snaith, Nano Lett. 13 (2013) 4505—4510.
[123] D. Bi, S.-J. Moon, L. Haggman, G. Boschloo, L. Yang, E.M.J. Johansson, M.K. Nazeeruddin, M. Gratzel, A. Hagfeldt, RSC Adv. 3 (2013) 18762—18766.
[124] S.H. Hwang, J. Roh, J. Lee, J. Ryu, J. Yun, J. Jang, J. Mater. Chem. A 2 (2014) 16429—16433.
[125] M.J. Carnie, C. Charbonneau, M.L. Davies, B.O. Regan, D.A. Worsley, T.M. Watson, J. Mater. Chem. A 2 (2014) 17077—17084.
[126] S. Aharon, S. Gamliel, B.E. Cohen, L. Etgar, Phys. Chem. Chem. Phys. 16 (2014) 10512—10518.
[127] S. Aharon, B.E. Cohen, L. Etgar, J. Phys. Chem. C 118 (2014) 17160—17165.
[128] W.A. Laban, L. Etgar, Energy Environ. Sci. 6 (2013) 3249—3253.
[129] B.-E. Cohen, S. Gamliel, L. Etgar, APL Mater. 2 (2014) 081502.
[130] J. Shi, Y. Luo, H. Wei, J. Luo, J. Dong, S. Lv, J. Xiao, Y. Xu, L. Zhu, X. Xu, H. Wu, D. Li, Q. Meng, ACS Appl. Mater. Interfaces 6 (2014) 9711—9718.
[131] Y. Xu, J. Shi, S. Lv, L. Zhu, J. Dong, H. Wu, Y. Xiao, Y. Luo, S. Wang, D. Li, X. Li, Q. Meng, ACS Appl. Mater. Interfaces 6 (2014) 5651—5656.
[132] J. Shi, J. Dong, S. Lv, Y. Xu, L. Zhu, J. Xiao, X. Xu, H. Wu, D. Li, Y. Luo, Q. Meng, Appl. Phys. Lett. 104 (2014) 063901.
[133] F. Zhang, X. Yang, H. Wang, M. Cheng, J. Zhao, L. Sun, ACS Appl. Mater. Interfaces 6 (2014) 16140—16146.
[134] Q. Jiang, X. Sheng, B. Shi, X. Feng, T. Xu, J. Phys. Chem. C 118 (2014) 25878—25883.
[135] P.-W. Liang, C.-Y. Liao, C.-C. Chueh, F. Zuo, S.T. Williams, X.-K. Xin, J. Lin, A.K.Y. Jen, Adv. Mater. 26 (2014) 3748—3754.
[136] S.N. Habisreutinger, T. Leijtens, G.E. Eperon, S.D. Stranks, R.J. Nicholas, H.J. Snaith, Nano Lett. 14 (2014) 5561—5568.
[137] H. Zhou, Y. Shi, Q. Dong, H. Zhang, Y. Xing, K. Wang, Y. Du, T. Ma, J. Phys. Chem. Lett. (2014) 3241—3246.
[138] X. Wang, Z. Li, W. Xu, S.A. Kulkarni, S.K. Batabyal, S. Zhang, A. Cao, L.H. Wong, Nano Energy 11 (2015) 728—735.
[139] Y. Liu, Z. Hong, Q. Chen, W. Chang, H. Zhou, T.-B. Song, E. Young, Y. Yang, J. You, G. Li, Y. Yang, Nano Lett. 15 (2014) 662—668.
[140] C. Zuo, L. Ding, J. Mater. Chem. A 3 (2015) 9063—9066.
[141] L. Qiu, J. Deng, X. Lu, Z. Yang, H. Peng, Angew. Chem. Int. Ed. 53 (2014) 10425—10428.
[142] B.J. Kim, D.H. Kim, Y.-Y. Lee, H.-W. Shin, G.S. Han, J.S. Hong, K. Mahmood, T.K. Ahn, Y.-C. Joo, K.S. Hong, N.-G. Park, S. Lee, H.S. Jung, Energy Environ. Sci. 8 (2015) 916—921.
[143] Y. Dkhissi, F. Huang, S. Rubanov, M. Xiao, U. Bach, L. Spiccia, R.A. Caruso, Y.-B. Cheng, J. Power Sources 278 (2015) 325—331.
[144] C. Roldan-Carmona, O. Malinkiewicz, A. Soriano, G. Minguez Espallargas, A. Garcia, P. Reinecke, T. Kroyer, M.I. Dar, M.K. Nazeeruddin, H.J. Bolink, Energy Environ. Sci. 7 (2014) 994—997.
[145] Y.-F. Chiang, J.-Y. Jeng, M.-H. Lee, S.-R. Peng, P. Chen, T.-F. Guo, T.-C. Wen, Y.-J. Hsu, C.-M. Hsu, Phys. Chem. Chem. Phys. 16 (2014) 6033—6040.
[146] J.W. Jung, S.T. Williams, A.K.Y. Jen, RSC Adv. 4 (2014) 62971—62977.
[147] P. Docampo, J.M. Ball, M. Darwich, G.E. Eperon, H.J. Snaith, Nat. Commun. 4 (2013) 2761.
[148] D. Liu, T.L. Kelly, Nat. Photonics 8 (2014) 133—138.
[149] L. Liang, Z. Huang, L. Cai, W. Chen, B. Wang, K. Chen, H. Bai, Q. Tian, B. Fan, ACS Appl. Mater. Interfaces 6 (2014) 20585—20589.
[150] T.C. Sum, N. Mathews, Energy Environ. Sci. 7 (2014) 2518—2534.
[151] J.S. Manser, P.V. Kamat, Nat. Photonics 8 (2014) 737—743.
[152] F. Deschler, M. Price, S. Pathak, L.E. Klintberg, D.-D. Jarausch, R. Higler, S. Hüttner, T. Leijtens, S.D. Stranks, H.J. Snaith,

M. Atatüre, R.T. Phillips, R.H. Friend, J. Phys. Chem. Lett. 5 (2014) 1421—1426.
[153] G. Xing, N. Mathews, S.S. Lim, N. Yantara, X. Liu, D. Sabba, M. Grätzel, S. Mhaisalkar, T.C. Sum, Nat. Mater. 13 (2014) 476—480.
[154] W.-J. Yin, T. Shi, Y. Yan, Adv. Mater. 26 (2014) 4653—4658.
[155] W.-J. Yin, T. Shi, Y. Yan, Appl. Phys. Lett. 104 (2014) 063903.
[156] H.-S. Duan, H. Zhou, Q. Chen, P. Sun, S. Luo, T.-B. Song, B. Bob, Y. Yang, Phys. Chem. Chem. Phys. 17 (2015) 112—116.
[157] M. Samiee, S. Konduri, B. Ganapathy, R. Kottokkaran, H.A. Abbas, A. Kitahara, P. Joshi, L. Zhang, M. Noack, V. Dalal, Appl. Phys. Lett. 105 (2014) 153502.
[158] A. Buin, P. Pietsch, J. Xu, O. Voznyy, A.H. Ip, R. Comin, E.H. Sargent, Nano Lett. 14 (2014) 6281—6286.
[159] Y. Shao, Z. Xiao, C. Bi, Y. Yuan, J. Huang, Nat. Commun. 5 (2014) 5784.
[160] Q. Chen, H. Zhou, T.-B. Song, S. Luo, Z. Hong, H.-S. Duan, L. Dou, Y. Liu, Y. Yang, Nano Lett. 14 (2014) 4158—4163.
[161] T. Supasai, N. Rujisamphan, K. Ullrich, A. Chemseddine, T. Dittrich, Appl. Phys. Lett. 103 (2013) 183906.
[162] S. Lv, L. Han, J. Xiao, L. Zhu, J. Shi, H. Wei, Y. Xu, J. Dong, X. Xu, D. Li, S. Wang, Y. Luo, Q. Meng, X. Li, Chem. Commun. 50 (2014) 6931—6934.
[163] J. Wang, S. Wang, X. Li, L. Zhu, Q. Meng, Y. Xiao, D. Li, Chem. Commun. 50 (2014) 5829—5832.
[164] C. Wehrenfennig, G.E. Eperon, M.B. Johnston, H.J. Snaith, L.M. Herz, Adv. Mater. 26 (2014) 1584—1589.
[165] H. Oga, A. Saeki, Y. Ogomi, S. Hayase, S. Seki, J. Am. Chem. Soc. 136 (2014) 13818—13825.
[166] Y. Yamada, T. Nakamura, M. Endo, A. Wakamiya, Y. Kanemitsu, J. Am. Chem. Soc. 136 (2014) 11610—11613.
[167] A. Marchioro, J. Teuscher, D. Friedrich, M. Kunst, R. van de Krol, T. Moehl, M. Gratzel, J.-E. Moser, Nat. Photonics 8 (2014) 250—255.
[168] H.-S. Kim, I. Mora-Sero, V. Gonzalez-Pedro, F. Fabregat-Santiago, E.J. Juarez-Perez, N.-G. Park, J. Bisquert, Nat. Commun. 4 (2013) 2242.
[169] V.M. Burlakov, G.E. Eperon, H.J. Snaith, S.J. Chapman, A. Goriely, Appl. Phys. Lett. 104 (2014) 091602.
[170] C.-W. Chen, H.-W. Kang, S.-Y. Hsiao, P.-F. Yang, K.-M. Chiang, H.-W. Lin, Adv. Mater. 26 (2014) 6647—6652.
[171] B.R. Sutherland, S. Hoogland, M.M. Adachi, P. Kanjanaboos, C.T.O. Wong, J.J. McDowell, J. Xu, O. Voznyy, Z. Ning, A.J. Houtepen, E.H. Sargent, Adv. Mater. 27 (2015) 53—58.
[172] T. Leijtens, B. Lauber, G.E. Eperon, S.D. Stranks, H.J. Snaith, J. Phys. Chem. Lett. (2014) 1096—1102.
[173] Z. Xiao, C. Bi, Y. Shao, Q. Dong, Q. Wang, Y. Yuan, C. Wang, Y. Gao, J. Huang, Energy Environ. Sci. 7 (2014) 2619—2623.
[174] Y. Song, S. Lv, X. Liu, X. Li, S. Wang, H. Wei, D. Li, Y. Xiao, Q. Meng, Chem. Commun. 50 (2014) 15239—15242.
[175] M.R. Leyden, L.K. Ono, S.R. Raga, Y. Kato, S. Wang, Y. Qi, J. Mater. Chem. A 2 (2014) 18742—18745.
[176] J.-H. Im, H.-S. Kim, N.-G. Park, APL Mater. 2 (2014) 081510.
[177] D.T. Moore, H. Sai, K. Wee Tan, L.A. Estroff, U. Wiesner, APL Mater. 2 (2014) 081802.
[178] K. Yamada, K. Nakada, Y. Takeuchi, K. Nawa, Y. Yamane, Bull. Chem. Soc. Jpn. 84 (2011) 926—932.
[179] Y. Zhao, K. Zhu, J. Phys. Chem. Lett. 5 (2014) 4175—4186.
[180] T.-B. Song, Q. Chen, H. Zhou, S. Luo, Y. Yang, J. You, Y. Yang, Nano Energy 12 (2015) 494—500.
[181] G.E. Eperon, V.M. Burlakov, P. Docampo, A. Goriely, H.J. Snaith, Adv. Funct. Mater. 24 (2014) 151—157.
[182] M. Saliba, K.W. Tan, H. Sai, D.T. Moore, T. Scott, W. Zhang, L.A. Estroff, U. Wiesner, H.J. Snaith, J. Phys. Chem. C 118 (2014) 17171—17177.
[183] C. Zuo, L. Ding, Nanoscale 6 (2014) 9935—9938.
[184] C.-C. Chen, S.-H. Bae, W.-H. Chang, Z. Hong, G. Li, Q. Chen, H. Zhou, Y. Yang, Mater. Horiz. 2 (2015) 203—211.
[185] J. You, Y. Yang, Z. Hong, T.-B. Song, L. Meng, Y. Liu, C. Jiang, H. Zhou, W.-H. Chang, G. Li, Y. Yang, Appl. Phys. Lett. 105 (2014) 183902.
[186] Z. Xiao, Q. Dong, C. Bi, Y. Shao, Y. Yuan, J. Huang, Adv. Mater. 26 (2014) 6503—6509.
[187] M. Xiao, F. Huang, W. Huang, Y. Dkhissi, Y. Zhu, J. Etheridge, A. Gray-Weale, U. Bach, Y.-B. Cheng, L. Spiccia, Angew. Chem. 126 (2014) 10056—10061.
[188] F. Huang, Y. Dkhissi, W. Huang, M. Xiao, I. Benesperi, S. Rubanov, Y. Zhu, X. Lin, L. Jiang, Y. Zhou, A. Gray-Weale, J. Etheridge, C.R. McNeill, R.A. Caruso, U. Bach, L. Spiccia, Y.-B. Cheng, Nano Energy 10 (2014) 10—18.
[189] H.-B. Kim, H. Choi, J. Jeong, S. Kim, B. Walker, S. Song, J.Y. Kim, Nanoscale 6 (2014) 6679—6683.
[190] H.J. Snaith, M. Gratzel, Adv. Mater. 19 (2007) 3643—3647.
[191] U.B. Cappel, T. Daeneke, U. Bach, Nano Lett. 12 (2012) 4925—4931.
[192] T.M. Koh, S. Dharani, H. Li, R.R. Prabhakar, N. Mathews, A.C. Grimsdale, S.G. Mhaisalkar, ChemSusChem 7 (2014) 1909—1914.
[193] J.H. Noh, N.J. Jeon, Y.C. Choi, M.K. Nazeeruddin, M. Gratzel, S.I. Seok, J. Mater. Chem. A 1 (2013) 11842—11847.
[194] B. Xu, J. Huang, H. Agren, L. Kloo, A. Hagfeldt, L. Sun, ChemSusChem 7 (2014) 3252—3256.
[195] A. Abate, D.J. Hollman, J. Teuscher, S. Pathak, R. Avolio, G. D'Errico, G. Vitiello, S. Fantacci, H.J. Snaith, J. Am. Chem. Soc. 135 (2013) 13538—13548.
[196] A. Abate, T. Leijtens, S. Pathak, J. Teuscher, R. Avolio, M.E. Errico, J. Kirkpatrik, J.M. Ball, P. Docampo, I. McPherson, H.J. Snaith, Phys. Chem. Chem. Phys. 15 (2013) 2572—2579.
[197] J. Burschka, A. Dualeh, F. Kessler, E. Baranoff, N.L. Cevey-Ha, C. Yi, M.K. Nazeeruddin, M. Gratzel, J. Am. Chem. Soc. 133 (2011) 18042—18045.
[198] L. Yang, B. Xu, D. Bi, H. Tian, G. Boschloo, L. Sun, A. Hagfeldt, E.M.J. Johansson, J. Am. Chem. Soc. 135 (2013) 7378—7385.
[199] Z. Hawash, L.K. Ono, S.R. Raga, M.V. Lee, Y. Qi, Chem. Mater. 27 (2014) 562—569.
[200] N.J. Jeon, J. Lee, J.H. Noh, M.K. Nazeeruddin, M. Gratzel, S.I. Seok, J. Am. Chem. Soc. 135 (2013) 19087—19090.
[201] H. Choi, S. Paek, N. Lim, Y.H. Lee, M.K. Nazeeruddin, J. Ko, Chemistry 20 (2014) 10894—10899.
[202] H. Choi, S. Park, S. Paek, P. Ekanayake, M.K. Nazeeruddin, J. Ko, J. Mater. Chem. A 2 (2014) 19136—19140.
[203] N.J. Jeon, H.G. Lee, Y.C. Kim, J. Seo, J.H. Noh, J. Lee, S.I. Seok, J. Am. Chem. Soc. 136 (2014) 7837—7840.
[204] A. Krishna, D. Sabba, H. Li, J. Yin, P.P. Boix, C. Soci, S.G. Mhaisalkar, A.C. Grimsdale, Chem. Sci. 5 (2014) 2702—2709.
[205] T. Krishnamoorthy, F. Kunwu, P.P. Boix, H. Li, T.M. Koh, W.L. Leong, S. Powar, A. Grimsdale, M. Grätzel, N. Mathews, S.G. Mhaisalkar, J. Mater. Chem. A 2 (2014) 6305—6309.
[206] H. Li, K. Fu, A. Hagfeldt, M. Gratzel, S.G. Mhaisalkar, A.C. Grimsdale, Angew. Chem. Int. Ed. Engl. 53 (2014) 4085—4088.
[207] J. Liu, Y. Wu, C. Qin, X. Yang, T. Yasuda, A. Islam, K. Zhang, W. Peng, W. Chen, L. Han, Energy Environ. Sci. 7 (2014) 2963—2967.
[208] P. Qin, S. Tanaka, S. Ito, N. Tetreault, K. Manabe, H. Nishino, M.K. Nazeeruddin, M. Gratzel, Nat. Commun. 5 (2014) 3834.
[209] J. Xiao, L. Han, L. Zhu, S. Lv, J. Shi, H. Wei, Y. Xu, J. Dong, X. Xu, Y. Xiao, D. Li, S. Wang, Y. Luo, X. Li, Q. Meng, RSC Adv. 4 (2014) 32918—32923.
[210] L. Zheng, Y.H. Chung, Y. Ma, L. Zhang, L. Xiao, Z. Chen, S. Wang, B. Qu, Q. Gong, Chem. Commun. 50 (2014) 11196—11199.
[211] M. Cheng, B. Xu, C. Chen, X. Yang, F. Zhang, Q. Tan, Y. Hua, L. Kloo, L. Sun, Adv. Energy Mater. 5 (2015) 1401720.

[212] A. Ishii, A.K. Jena, T. Miyasaka, APL Mater. 2 (2014) 091102.
[213] H. Chen, X. Pan, W. Liu, M. Cai, D. Kou, Z. Huo, X. Fang, S. Dai, Chem. Commun. 49 (2013) 7277—7279.
[214] M. Cai, V.T. Tiong, T. Hreid, J. Bell, H. Wang, J. Mater. Chem. A 3 (2014) 2784—2793.
[215] F. Di Giacomo, S. Razza, F. Matteocci, A. D'Epifanio, S. Licoccia, T.M. Brown, A. Di Carlo, J. Power Sources 251 (2014) 152—156.
[216] Y.S. Kwon, J. Lim, H.-J. Yun, Y.-H. Kim, T. Park, Energy Environ. Sci. 7 (2014) 1454—1460.
[217] J.W. Lee, S. Park, M.J. Ko, H.J. Son, N.G. Park, ChemPhysChem 15 (2014) 2595—2603.
[218] K.G. Lim, H.B. Kim, J. Jeong, H. Kim, J.Y. Kim, T.W. Lee, Adv. Mater. 26 (2014) 6461—6466.
[219] Q. Lin, A. Armin, R.C.R. Nagiri, P.L. Burn, P. Meredith, Nat. Photonics 9 (2015) 106—112.
[220] K. Neumann, M. Thelakkat, RSC Adv. 4 (2014) 43550—43559.
[221] S. Ryu, J.H. Noh, N.J. Jeon, Y. Chan Kim, W.S. Yang, J. Seo, S.I. Seok, Energy Environ. Sci. 7 (2014) 2614—2618.
[222] W. Yan, Y. Li, W. Sun, H. Peng, S. Ye, Z. Liu, Z. Bian, C. Huang, RSC Adv. 4 (2014) 33039—33046.
[223] D. Zhao, M. Sexton, H.-Y. Park, G. Baure, J.C. Nino, F. So, Adv. Energy Mater. (2014) 1401855.
[224] Z. Zhu, J. Ma, Z. Wang, C. Mu, Z. Fan, L. Du, Y. Bai, L. Fan, H. Yan, D.L. Phillips, S. Yang, J. Am. Chem. Soc. 136 (2014) 3760—3763.
[225] P. Nagarjuna, K. Narayanaswamy, T. Swetha, G.H. Rao, S.P. Singh, G.D. Sharma, Electrochim. Acta 151 (2015) 21—26.
[226] J. Xiao, J. Shi, H. Liu, Y. Xu, S. Lv, Y. Luo, D. Li, Q. Meng, Y. Li, Adv. Energy Mater. (2015) 1401943.
[227] M. Zhang, M. Lyu, H. Yu, J.H. Yun, Q. Wang, L. Wang, Chemistry 21 (2015) 434—439.
[228] Y. Zhang, W. Liu, F. Tan, Y. Gu, J. Power Sources 274 (2015) 1224—1230.
[229] Z. Wu, S. Bai, J. Xiang, Z. Yuan, Y. Yang, W. Cui, X. Gao, Z. Liu, Y. Jin, B. Sun, Nanoscale 6 (2014) 10505—10510.
[230] J.A. Christians, R.C. Fung, P.V. Kamat, J. Am. Chem. Soc. 136 (2014) 758—764.
[231] K.C. Wang, J.Y. Jeng, P.S. Shen, Y.C. Chang, E.W. Diau, C.H. Tsai, T.Y. Chao, H.C. Hsu, P.Y. Lin, P. Chen, T.F. Guo, T.C. Wen, Sci. Rep. 4 (2014) 4756.
[232] J.Y. Jeng, K.C. Chen, T.Y. Chiang, P.Y. Lin, T.D. Tsai, Y.C. Chang, T.F. Guo, P. Chen, T.C. Wen, Y.J. Hsu, Adv. Mater. 26 (2014) 4107—4113.
[233] A.S. Subbiah, A. Halder, S. Ghosh, N. Mahuli, G. Hodes, S.K. Sarkar, J. Phys. Chem. Lett. 5 (2014) 1748—1753.
[234] S. Ito, S. Tanaka, H. Vahlman, H. Nishino, K. Manabe, P. Lund, ChemPhysChem 15 (2014) 1194—1200.
[235] L. Etgar, P. Gao, P. Qin, M. Graetzel, M.K. Nazeeruddin, J. Mater. Chem. A 2 (2014) 11586—11590.
[236] Y. Wang, T. Gould, J.F. Dobson, H. Zhang, H. Yang, X. Yao, H. Zhao, Phys. Chem. Chem. Phys. 16 (2014) 1424—1429.
[237] C.V. Kumar, G. Sfyri, D. Raptis, E. Stathatos, P. Lianos, RSC Adv. 5 (2014) 3786—3791.
[238] K. Wojciechowski, M. Saliba, T. Leijtens, A. Abate, H.J. Snaith, Energy Environ. Sci. 7 (2014) 1142—1147.
[239] B. Conings, L. Baeten, T. Jacobs, R. Dera, J. D'Haen, J. Manca, H.-G. Boyen, APL Mater. 2 (2014) 081505.
[240] W. Yongzhen, Y. Xudong, C. Han, Z. Kun, Q. Chuanjiang, L. Jian, P. Wenqin, I. Ashraful, B. Enbing, Y. Fei, Y. Maoshu, Z. Peng, H. Liyuan, Appl. Phys. Express 7 (2014) 052301.
[241] S. Paek, N. Cho, H. Choi, H. Jeong, J.S. Lim, J.-Y. Hwang, J.K. Lee, J. Ko, J. Phys. Chem. C 118 (2014) 25899—25905.
[242] C.-H. Chiang, Z.-L. Tseng, C.-G. Wu, J. Mater. Chem. A 2 (2014) 15897—15903.
[243] A. Abate, M. Saliba, D.J. Hollman, S.D. Stranks, K. Wojciechowski, R. Avolio, G. Grancini, A. Petrozza, H.J. Snaith, Nano Lett. 14 (2014) 3247—3254.
[244] N.K. Noel, A. Abate, S.D. Stranks, E.S. Parrott, V.M. Burlakov, A. Goriely, H.J. Snaith, ACS Nano 8 (2014) 9815—9821.
[245] W. Li, H. Dong, L. Wang, N. Li, X. Guo, J. Li, Y. Qiu, J. Mater. Chem. A 2 (2014) 13587—13592.
[246] Y. Ogomi, K. Kukihara, S. Qing, T. Toyoda, K. Yoshino, S. Pandey, H. Momose, S. Hayase, ChemPhysChem 15 (2014) 1062—1069.
[247] Y. Ogomi, A. Morita, S. Tsukamoto, T. Saitho, Q. Shen, T. Toyoda, K. Yoshino, S.S. Pandey, T. Ma, S. Hayase, J. Phys. Chem. C 118 (2014) 16651—16659.
[248] K. Wojciechowski, S.D. Stranks, A. Abate, G. Sadoughi, A. Sadhanala, N. Kopidakis, G. Rumbles, C.-Z. Li, R.H. Friend, A.K.Y. Jen, H.J. Snaith, ACS Nano 8 (2014) 12701—12709.
[249] A. Abrusci, S.D. Stranks, P. Docampo, H.-L. Yip, A.K.Y. Jen, H.J. Snaith, Nano Lett. 13 (2013) 3124—3128.
[250] E.L. Unger, E.T. Hoke, C.D. Bailie, W.H. Nguyen, A.R. Bowring, T. Heumuller, M.G. Christoforo, M.D. McGehee, Energy Environ. Sci. 7 (2014) 3690—3698.
[251] K. Sun, J. Chang, F.H. Isikgor, P. Li, J. Ouyang, Nanoscale 7 (2014) 896—900.
[252] H.-S. Kim, N.-G. Park, J. Phys. Chem. Lett. (2014) 2927—2934.
[253] S. Ito, S. Tanaka, K. Manabe, H. Nishino, J. Phys. Chem. C 118 (2014) 16995—17000.
[254] X. Dong, X. Fang, M. Lv, B. Lin, S. Zhang, J.N. Ding, N. Yuan, J. Mater. Chem. A 3 (2015) 5360—5367.
[255] W. Shockley, H.J. Queisser, J. Appl. Phys. 32 (1961) 510—519.
[256] B. Minnaert, P. Veelaert, Materials 5 (2012) 1933—1953.
[257] M. Graetzel, R.A. Janssen, D.B. Mitzi, E.H. Sargent, Nature 488 (2012) 304—312.
[258] P. Löper, S.-J. Moon, S.M. de Nicolas, B. Niesen, M. Ledinsky, S. Nicolay, J. Bailat, J.-H. Yum, S. De Wolf, C. Ballif, Phys. Chem. Chem. Phys. 17 (2015) 1619—1629.
[259] C.D. Bailie, M.G. Christoforo, J.P. Mailoa, A.R. Bowring, E.L. Unger, W.H. Nguyen, J. Burschka, N. Pellet, J.Z. Lee, M. Gratzel, R. Noufi, T. Buonassisi, A. Salleo, M.D. McGehee, Energy Environ. Sci. 8 (2015) 956—963.
[260] T. Todorov, T. Gershon, O. Gunawan, C. Sturdevant, S. Guha, Appl. Phys. Lett. 105 (2014) 173902.
[261] J. Sakai, K. Kawano, T. Yamanari, T. Taima, Y. Yoshida, A. Fujii, M. Ozaki, Sol. Energy Mater. Sol. Cells 94 (2010) 376—380.
[262] J.J. Choi, W.N. Wenger, R.S. Hoffman, Y.F. Lim, J. Luria, J. Jasieniak, J.A. Marohn, T. Hanrath, Adv. Mater. 23 (2011) 3144—3148.
[263] C.-C. Chen, L. Dou, J. Gao, W.-H. Chang, G. Li, Y. Yang, Energy Environ. Sci. 6 (2013) 2714—2720.
[264] C.C. Chen, W.H. Chang, K. Yoshimura, K. Ohya, J. You, J. Gao, Z. Hong, Y. Yang, Adv. Mater. 26 (2014) 5670—5677.
[265] O. Malinkiewicz, A. Yella, Y.H. Lee, G.M. Espallargas, M. Graetzel, M.K. Nazeeruddin, H.J. Bolink, Nat. Photonics 8 (2013) 128—132.
[266] X. Wang, G.I. Koleilat, J. Tang, H. Liu, I.J. Kramer, R. Debnath, L. Brzozowski, D.A.R. Barkhouse, L. Levina, S. Hoogland, Nat. Photonics 5 (2011) 480—484.
[267] C.H. Chou, W.L. Kwan, Z. Hong, L.M. Chen, Y. Yang, Adv. Mater. 23 (2011) 1282—1286.
[268] C. Roldan, O. Malinkiewicz, R. Betancur, G. Longo, C. Momblona, F. Jaramillo, L. Camacho, H.J. Bolink, Energy Environ. Sci. 7 (2014) 2968—2973.
[269] D. Bryant, P. Greenwood, J. Troughton, M. Wijdekop, M. Carnie, M. Davies, K. Wojciechowski, H.J. Snaith, T. Watson, D. Worsley, Adv. Mater. 26 (2014) 7499—7504.
[270] F. Guo, H. Azimi, Y. Hou, T. Przybilla, M. Hu, C. Bronnbauer, S. Langner, E. Spiecker, K. Forberich, C.J. Brabec, Nanoscale 7 (2015) 1642—1649.
[271] G. Niu, W. Li, F. Meng, L. Wang, H. Dong, Y. Qiu, J. Mater. Chem. A 2 (2014) 705—710.

[272] S.K. Pathak, A. Abate, T. Leijtens, D.J. Hollman, J. Teuscher, L. Pazos, P. Docampo, U. Steiner, H.J. Snaith, Adv. Energy Mater. 4 (2014) 1301667.
[273] N. Chander, A.F. Khan, P.S. Chandrasekhar, E. Thouti, S.K. Swami, V. Dutta, V.K. Komarala, Appl. Phys. Lett. 105 (2014) 033904.
[274] Y. Zhao, K. Zhu, Chem. Commun. 50 (2014) 1605—1607.
[275] H.J. Snaith, A. Abate, J.M. Ball, G.E. Eperon, T. Leijtens, N.K. Noel, S.D. Stranks, J.T.-W. Wang, K. Wojciechowski, W. Zhang, J. Phys. Chem. Lett. 5 (2014) 1511—1515.
[276] R. Gottesman, E. Haltzi, L. Gouda, S. Tirosh, Y. Bouhadana, A. Zaban, E. Mosconi, F. De Angelis, J. Phys. Chem. Lett. 5 (2014) 2662—2669.
[277] W. Nie, H. Tsai, R. Asadpour, J.-C. Blancon, A.J. Neukirch, G. Gupta, J.J. Crochet, M. Chhowalla, S. Tretiak, M.A. Alam, H.-L. Wang, A.D. Mohite, Science 347 (2015) 522—525.
[278] J. Wei, Y. Zhao, H. Li, G. Li, J. Pan, D. Xu, Q. Zhao, D. Yu, J. Phys. Chem. Lett. 5 (2014) 3937—3945.
[279] H.-W. Chen, N. Sakai, M. Ikegami, T. Miyasaka, J. Phys. Chem. Lett. 6 (2014) 164—169.
[280] Y. Kutes, L. Ye, Y. Zhou, S. Pang, B.D. Huey, N.P. Padture, J. Phys. Chem. Lett. (2014) 3335—3339.
[281] L. Bertoluzzi, R.S. Sanchez, L. Liu, J.-W. Lee, E. Mas-Marza, H. Han, N.-G. Park, I. Mora-Sero, J. Bisquert, Energy Environ. Sci. 8 (2015) 910—915.
[282] W. Tress, N. Marinova, T. Moehl, S.M. Zakeeruddin, M.K. Nazeeruddin, M. Gratzel, Energy Environ. Sci. 8 (2015) 995—1004.
[283] D.B. Mitzi, J. Mater. Chem. 14 (2004) 2355—2365.
[284] L. Dou, Y. Yang, J. You, Z. Hong, W.-H. Chang, G. Li, Y. Yang, Nat. Commun. 5 (2014) 5404.
[285] H.-R. Xia, J. Li, W.-T. Sun, L.-M. Peng, Chem. Commun. 50 (2014) 13695—13697.
[286] R. Dong, Y. Fang, J. Chae, J. Dai, Z. Xiao, Q. Dong, Y. Yuan, A. Centrone, X.C. Zeng, J. Huang, Adv. Mater. 7 (2015) 1912—1918.
[287] Z.-K. Tan, R.S. Moghaddam, M.L. Lai, P. Docampo, R. Higler, F. Deschler, M. Price, A. Sadhanala, L.M. Pazos, D. Credgington, F. Hanusch, T. Bein, H.J. Snaith, R.H. Friend, Nat. Nanotechnol. 9 (2014) 687—692.
[288] Y.-H. Kim, H. Cho, J.H. Heo, T.-S. Kim, N. Myoung, C.-L. Lee, S.H. Im, T.-W. Lee, Adv. Mater. 27 (2014) 1248—1254.
[289] X.Y. Chin, D. Cortecchia, J. Yin, A. Bruno, C. Soci, arXiv:1501.04407v1.
[290] X. Hu, X. Zhang, L. Liang, J. Bao, S. Li, W. Yang, Y. Xie, Adv. Funct. Mater. 24 (2014) 7373—7380.
[291] Y. Lee, J. Kwon, E. Hwang, C.-H. Ra, W.J. Yoo, J.-H. Ahn, J.H. Park, J.H. Cho, Adv. Mater. 27 (2015) 41—46.
[292] K. Tvingstedt, O. Malinkiewicz, A. Baumann, C. Deibel, H.J. Snaith, V. Dyakonov, H.J. Bolink, Sci. Rep. 4 (2014) 6071.
[293] S.D. Stranks, V.M. Burlakov, T. Leijtens, J.M. Ball, A. Goriely, H.J. Snaith, Phys. Rev. Appl. 2 (2014) 034007.
[294] R.L.Z. Hoye, M.R. Chua, K.P. Musselman, G. Li, M.-L. Lai, Z.-K. Tan, N.C. Greenham, J.L. MacManus-Driscoll, R.H. Friend, D. Credgington, Adv. Mater. 27 (2015) 1414—1419.
[295] B.R. Sutherland, S. Hoogland, M.M. Adachi, C.T.O. Wong, E.H. Sargent, ACS Nano 8 (2014) 10947—10952.
[296] K. Yan, M. Long, T. Zhang, Z. Wei, H. Chen, S. Yang, J. Xu, J. Am. Chem. Soc. 137 (2015) 4460—4468.
[297] W. Nie, H. Tsai, R. Asadpour, J.-C. Blancon, A.J. Neukirch, G. Gupta, J.J. Crochet, M. Chhowalla, S. Tretiak, M.A. Alam, H.-L. Wang, A.D. Mohite, Science 347 (2015) 522—525.
[298] H. Uzu, M. Ichikawa, M. Hino, K. Nakano, T. Meguro, J.L. Hernández, H.-S. Kim, N.-G. Park, K. Yamamoto, Appl. Phys. Lett. 106 (2015) 013506.
[299] J.P. Mailoa, C.D. Bailie, E.C. Johlin, E.T. Hoke, A.J. Akey, W.H. Nguyen, M.D. McGehee, T. Buonassisi, Appl. Phys. Lett. 106 (2015) 121105.

Qi Chen got his B.S and Master's degrees from Tsinghua University in China, and received his Ph.D. degree in Materials Science and Engineering from University of California at Los Angeles (UCLA) in the year 2012. Now, he is working as a postdoc fellow in California Nanosystem Institute (CNSI) of UCLA. And his research focuses on hybrids materials, polymer blends for various applications, such as Photovoltaics, sensors, and detectors.

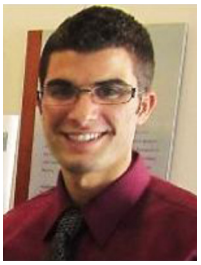

Nicholas De Marco is a Ph.D. candidate in Materials Science & Engineering at the University of California, Los Angeles (UCLA) under Prof. Yang Yang. He received his B.S. in Mechanical Engineering from the University of California, Merced (UCM) in 2013. His research focuses on hybrid nanomaterials and thin films for energy harvesting, storage, and other optoelectronic applications.

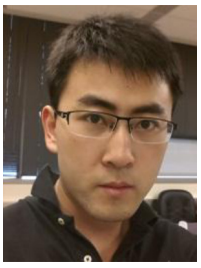

Yang (Michael) Yang received B.E. in Electrical Engineering from Zhejiang University, China in 2009. He was a research intern between 2009 and 2010 at institute of Chemistry, Chinese Academy of Sciences (ICCAS), under the supervision of Prof. Yongfang Li. He is now a Ph.D. Candidate in Prof. Yang Yang's group, in the Department of Materials Science and Engineering at UCLA. His research interests include organic and organic—inorganic hybrid optoelectronic device and their spectroscope study.

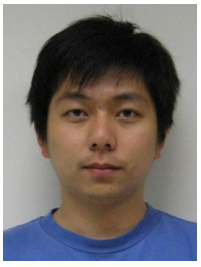

Tze-Bin Song is a Ph.D. candidate at the University of California Los Angeles (UCLA), in Materials Science and Engineering under the supervision of Prof. Yang Yang. He received his B.S. degree from National Tsing-Hua University, Taiwan, in 2007 and M.S. degree from University of Florida in 2010, both in Materials Science and Engineering. His research interests include development of thin film solar cells, transparent electrodes and material/device characterizations. During his Ph.D. studies, he had an internship in International Business Machines, T.J. Watson, NY, where he participated in developing the advanced integration technique.

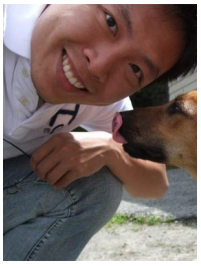

Chun-Chao Chen received his Ph.D. from the department of material science, UCLA. He has vast experiences in flexible electronics development. In his early career, he joined ITRI at Taiwan working on flexible polymeric transistors. Before he joined UCLA for his PhD, he also worked at Solarmer Inc. (El Monte, CA) for roll-to-roll printing of flexible solar cells. His main expertise is ink formulation, solution-based coating methods, and tandem solar cells.

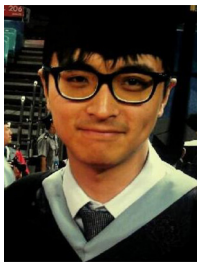

Hongxiang Zhao received his B.S. in chemistry from Peking University, China in 2013. He is currently a Ph.D. candidate in Prof. Yang Yang's lab, at department of Material Science and Engineering in UCLA. His research interests include molecule design and synthesis for organic photovoltaic and perovskite solar cell.

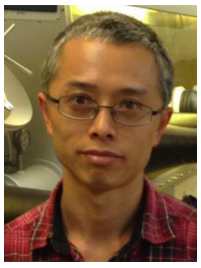

Ziruo Hong obtained BS in Chemistry from Sichuan Univ in 1995. In 1996, he entered Changchun Institute of Optics, Fine Mechanics and Physics of CAS. He studied condensed matter physics, and received training as a device physicist (Ph.D. 2001), mainly working on organic light emitting devices (OLEDs) and photovoltaic cells. He is now doing research on solution processed organic/inorganic hybrid semiconductors and devices in Prof. Yang Yang's group at UCLA. He has published 120 papers.

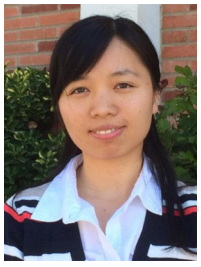

Dr. Huanping Zhou received her Ph.D. degree in Inorganic Chemistry from Peking University in the year 2010. Now, she is working as a postdoc fellow in Prof. Yang Yang's lab in UCLA. Her research focuses on nanomaterials, thin films, optoelectronics, etc.

Yang Yang received his M.S. and Ph.D. in Physics and Applied Physics from the University of Massachusetts, Lowell in 1988 and 1992, respectively. Before he joined UCLA in 1997, he served as the research staff in UNIAX (now DuPont Display) from 1992 to 1996. Yang is now the Carol and Lawrence E. Tannas Jr. Endowed Chair Professor of Materials Science at UCLA. He is also the Fellow of MRS, SPIE, RSC and the Electromagnetic (EM) Academy. He is an expertise in the fields of organic, inorganic and organic/inorganic hybrid electronics and the development and fabrication of related devices, such as photovoltaic cells, LEDs, transistor and memory devices.